Femtosecond Coherent Control of Quantum Systems in Liquid Phase

by

Andrei C. Florean

A dissertation submitted in partial fulfillment
of the requirements for the degree of
Doctor of Philosophy
(Physics)
in The University of Michigan
2008

Doctoral Committee:

Professor Roseanne J. Sension, Chair
Professor Paul R. Berman
Professor Theodore G. Goodson III
Associate Professor David A. Reis
Professor Philip H. Bucksbaum, Stanford University

To my parents and my sister,
who have always been close to me.

Acknowledgements

I would like to thank to all the people I worked with during my almost six years long PhD journey. First, I want to say thanks to Phil Bucksbaum, who, as advisor, offered me guidance and support. I have always been impressed by his ability to motivate people without criticizing them and by the way he directs our work, showing unexpected insights and bringing excitement and a positive attitude through the difficult moments. I have also benefited a lot from the advice and direction received from Roseanne Sension, who, as my University of Michigan advisor in the final years of the PhD, helped me a lot by setting high standards and providing constructive critics of my work, which significantly improved and clarified my research. At the beginning of my PhD I benefited a lot from the tutoring offered by Brett Pearson, who guided my first steps in an ultrafast laser lab. Warm thoughts go towards the other members of the Michigan group: Joel Murray, Haidan Wen, Catherine Herne, Santosh Pisharody and Emily Peterson with whom I shared the same laser system through many long days and nights. As my companions through the PhD years they shared with me the troubles and excitements of the lab work. Elizabeth Carroll is another person with whom I have shared the hardship and excitement of the PhD research. We spent a number of years working shoulder-to shoulder and I learned a lot from her pragmatic and goal-oriented attitude. The other members of Roseanne's group, Mike Orozco, Andy Stickrath and Kuo-Chun Tang have also helped me a lot, in the year before my move to Stanford. Ken Spears made an important contribution during his sabbatical visit to Ann Arbor, and his experimental and theoretical insights helped shape the coherent control experiments we performed there.

I have a very high appreciation for the Stanford group, with which I spent the last year of my PhD. James White brought an invaluable contribution, not only at Stanford but from the earliest stages of my work, at Ann Arbor, through his software skills. The genetic algorithms he helped perfect are a key component of our studies, and his

LabView skills made advanced data collection possible. David Cardoza is the other member of our team, and he never ceased to amaze me with his enthusiasm, energy and broad knowledge. We had many lively discussions which shaped the research direction for the best. I would also like to thank Markus Guehr, who helped a lot with advice and challenging discussions. He is not only one of the most uncompromising and hard-working persons I know, but also a very friendly and helpful guy. Special thanks go to Professor Janos Lanyi from University of California at Irvine, who kindly supplied the bacteriorhodopsin samples. The other people who shared with me the joy of research at Stanford are Joe Farrell, Brian McFarland, Doug Broege, Mike Glownia, Jaehee Kim and Ryan Coffee. I will always remember our lunches, where, by tradition, we would touch the political and scientific issues of the day, spiced with jokes and laughter.

Table of Contents

Dedication ..... **ii**

Acknowledgments ..... **iii**

List of Tables ..... **viii**

List of Figures ..... **ix**

Chapter

I. Introduction 1

II. Experimental Setup 11

2.1 The Ti:sapphire laser system 11

2.2 The NOPA 13

2.2.1 Introduction to Nonlinear Optics 13

2.2.1.1 White-light generation 14

2.2.1.2 Second harmonic generation 19

2.2.1.3 Pulse propagation in air 21

2.2.2 Large Bandwidth NOPA 21

2.3 Pulse Shaping 27

2.3.1 Theoretical Introduction 27

2.3.2 Practical Aspects 28

2.4 Optimization Techniques 31

2.5 Pulse Compression 36

2.6 Pulse Characterization 38

III. Control of vibrational coherences in LD690 41
3.1 Introduction to Coherent Control 41
3.2 Overview of LD690 Chemistry 43
3.3 Experimental Setup 45
3.4 Experimental Results 49
3.4.1 FFT Analysis of the Oscillatory Component 52
3.4.2 Analysis of Vibrational Frequencies and Dephasing 54
3.4.3 The Intensity of the Oscillations vs. the Probe Wavelength 56
3.4.4 The Phase of the Oscillations as a Function of Wavelength 61
3.4.5 Revivals in the Coherent Oscillations 61
3.5 Discussion 62
3.5.1 The Oscillation Frequency 63
3.5.2 Vibrational Dephasing 65
3.5.3 The Intensity of the Vibrational Coherences 66
3.5.4 The Phase of the Oscillations 67
3.5.5 Involvement of Higher Excited States 67
3.6 Conclusions 69

IV. Control of Retinal Isomerization in Bacteriorhodopsin 70
4.1 Introduction 70
4.1.1 Bacteriorhodopsin Chemistry 70
4.1.2 Coherent Control of Complex Molecules 77
4.2 Experimental Setup 78
4.3 Genetic Algorithm Results 83
4.4 Energy and Bandwidth Scans 87
4.5 Transient Scans 93
4.5.1 Transient Scans at 570 nm 93
4.5.2 Transient Scans at 487 nm and 850 nm 95
4.5.3 Transient Scans at 650 nm 99
4.6 Discussion and Conclusions 102

V. Conclusions 104
Bibliography 107

List of Tables

Table

2.1 The flatness parameter versus α. 23

3.1 Spectra and chirp rates used in the LD690 experiment. 52

3.2 Effective Damping Times in Picoseconds, with Error Bars, for Red-tuned and Broadband Excitation. 55

4.1 Decay times of the all-trans bleach for various phase profiles and two pulse energies. T_1 and T_2 are the time constants of the bi-exponential fit for each transient scan. 95

4.2 Column 2: decay times for the stimulated emission of the I_{460} conformation (single exponential fit). Columns 3 and 4: relative change of the signal for the all-trans bleach and I_{460} stimulated emission, in the interval T = 200 fs → T = 2 ps. The 10^{17} photons/cm^2 fluence corresponds to pulse energy of 120 nJ. 98

List of Figures

Figure		Page
1.1	Possible mechanisms for coherent control of molecular dynamics.....	3
1.2	Model of vibrational coherences in LD690 (top).....	6
1.3	Model of the electronic potential energy surface structure for retinal in bacteriorhodopsin.....	8
2.1	The femtosecond Ti: sapphire laser system.	12
2.2	Typical white-light spectrum in a sapphire plate.	16
2.3	Typical white-light spectrum generated in a jet of ethylene glycol.	16
2.4	A typical 2D plot of a transient scan in a non-resonant liquid medium.	17
2.5	Left panel: a section through Figure 2.4, at 570 nm.	18
2.6	A sample spectrum of the blue pump.	20
2.7	The 800 nm spectrum right after the amplifier (left panel) and after propagation through a few meters of air (right panel).	21
2.8	Top: the non-collinear geometry (the continuous, dotted and dashed lines represent the angularly dispersed pump beam for three pump wavelengths, the dashed-dotted line represents the seed beam, the thick continuous line is the crystal axis and the circle depicts the chirp-free fluorescence cone).	23
2.9	The Pellin-Broca prism based NOPA setup.	24
2.10	The NOPA spectrum (top), the pump (bottom right) and the seed spectrum (bottom left).	26
2.11	Schematic presentation of a 4f pulse shaping setup.	28

2.12 Left panel: the voltage values applied to the 128 pixels of the LCM mask. 31

2.13 Schematic presentation of the coherent control apparatus. 34

2.14 The genetic algorithm at work. 34

2.15 Two possible second-harmonic generation setups for pulse compression. 35

2.16 A typical compression GA, using as feedback a SHG FROG setup. 36

2.17 A schematic presentation of a prism-based double-pass compressor. 37

2.18 The group delay (500 nm – 650 nm spectrum) for three compressor configurations. 38

2.19 A typical SHG FROG setup. 39

2.20 The phase-matching bandwidth in BBO crystals of various lengths. 40

2.21 The intensity profile of the optimized pulse (left panel) and the retrieved phase (dashed line) and spectrum (solid line) profiles (right panel). 40

3.1 Schematic presentation of a pump-dump mechanism. 44

3.2 LD690 absorption spectrum (black open circles) and three of the pump spectra: red-tuned (RT, red dashed line), broadband (BB, green thick solid line), and the blue-tuned spectrum cut at 600 nm (BT2, blue thin solid line). 46

3.3 Experimental FROG traces (left-side column) and the retrieved time profiles (right-side column) of the excitation pulses for the broadband TL and NC cases..... 48

3.4 Left panel: typical two-dimensional plot of the transient kinetics. 51

3.5 Pump-probe kinetic traces collected at 610 nm, produced by excitation with the red-tuned (RT) and broadband (BB) TL pulses. 51

3.6 Frequency of the dominant mode vs. the probe wavelength, retrieved with the FFT procedure. 53

3.7 Frequency of the dominant vibrational mode vs. the probe wavelength for the red-tuned (red lines) and broadband (blue lines) cases. 54

3.8 Fourier power spectrum produced under excitation with the red-tuned TL pulse..... 57

3.9 Fourier intensity of the ring-breathing mode vs. the probe wavelength. 57

3.10 Fourier intensity of the ring-breathing mode vs. the probe wavelength, for red-tuned excitation: black line, PC1; red with squares, PC2; blue with triangles, PC3. 58

3.11 Fourier intensity of the ring-breathing mode vs. the probe wavelength, for broadband excitation, with TL (black line), ... 58

3.12 Fourier intensity of the ring-breathing mode plotted as a function of the probe wavelength, for BT1 excitation, with TL (black line), PC0 (red line with squares), PC2 (blue line with triangles), and NC2 (dotted line) phase profiles. .. 59

3.13 Fourier intensity of the ring-breathing mode plotted as a function of the probe wavelength, for BT2 excitation, with TL (black line), PC0 (red line with squares), PC2 (blue line with triangles), and NC2 (dotted line) phase profiles. .. 59

3.14 Bottom panel: wavelength dependence of the relative phase of the oscillations for RT excitation, with the TL (black line with squares), PC1 (red line with triangles), and NC1 (blue line with circles) phase profiles. 60

3.15 Kinetic traces obtained using negatively chirped broadband excitation for the probe wavelengths indicated on the figure. 60

3.16 Estimated absorption profile of the first excited electronic state. 65

4.1 An overview of the seven-helical structure of bacteriorhodopsin. 71

4.2 Retinal isomerization from the all-trans to the 13-cis isomer after photon absorption..... 72

4.3 The three-state model of retinal isomerization in bR. 75

4.4 The main high frequency modes involved in retinal isomerization. 76

4.5 The pump - probe setup for the bR experiment, top view. 80

4.6 Black lines: the probe absorption spectra at 487 nm, 570 nm, 650 nm and 850 nm. 82

4.7 A typical pump-probe transient spectrum where the full probe spectrum is monitored simultaneously. 84

4.8 A GA run performed at 150 nJ pump energy with a “Nπ” basis set. 86

4.9 The isomerization yield versus the probe bandwidth. 88

4.10 The pump spectra used in the bandwidth scan experiment. 88

4.11 Intensity scans monitoring the signal strength of the isomerization intermediates: 89

4.12 Upper panel: chirp scans monitoring the K590 (blue curve) and the J625 (black curve) conformations. 92

4.13 Transient scans for three excitation conditions. 94

4.14 Transient scans taken at 850 nm. 96

4.15 Transient scans measuring the dynamics of the I460 absorption, at 487 nm. 96

4.16 The black curve shows a transient scan taken at 487 nm, with a TL, high energy excitation pulse. 97

4.17 Transient scans at 650 nm, monitoring the J625 and K590 conformations. 99

4.18 Transient scans for the TL, negative chirp and a positive chirp pulse, at intermediate excitation energy. 100

Chapter I

Introduction

This dissertation is centered on the quest to control and understand molecular dynamics on a very short time scale [1], although the meaning of the word "short" changes continuously due to the fast pace of laser development. In the late 90's "ultrashort" referred to 5 – 10 fs laser pulses created with optical parametric amplifiers or directly out of laser oscillators [2-4]. In 2002 Kobayashi and Baltuška demonstrated a non-collinear optical parametric amplifier which generated 3.7 fs pulses in the visible spectral domain [5]. Soon afterwards attosecond (10^{-16} s) laser pulses took that record away [6]. Nevertheless, the new record is based on shifting the laser wavelength to very short (~ tens of nanometers) values. For direct excitation of molecular dynamics femtosecond "visible" (250 nm – 800 nm) pulses are the method of choice.

One could question the need for such broad ultrashort light sources, but they are instrumental in uncovering a broad range of phenomena [3]. Femtosecond spectroscopy has become central for the comprehension of molecular dynamics. Here a comparison with photographic techniques is granted. In 1877 Eadward Muybridge proved that a horse can have all four legs in air during its run. For that he used the fastest shutter and the most advanced photographic cameras of the time. Femtochemistry is not far from that approach, at least in spirit. Very short laser flashes enable the observation of a sequence of "frozen" molecular intermediate states, which can be added together to form a movie. This movie can be used to understand how molecules evolve after photoexcitation. At the time of this thesis the number of experiments using femtosecond "photography" to

uncover molecular dynamics is very large [3, 7-9]. The femto-chemistry field itself has received Nobel Prize recognition [1].

In the history of science understanding and controlling phenomena have always been tightly connected and this is also true for the ultrafast chemistry field [8-17]. At the beginning molecular control was regarded as remarkable in itself but then the standards were raised and understanding of the control mechanisms became required [18]. A large range of chemical processes proved to be controllable: dissociation, isomerization, charge-transfer, molecular vibrations and more [8, 9, 11-16, 18-33]. A number of general models of the control mechanism became standard in the scientific community [13, 16].

One primary model is the so-called Brumer – Shapiro scheme [16] which follows the analogy with a double-slit experiment (see Figure 1.1a). The underlying idea is that two appropriately shaped laser pulses can trigger a chemical reaction which evolves along two competing pathways. The coefficients of the eigenstates of the resulting wave packet will depend on the relative phase of the excitation pulses. The participating eigenstates correspond to different products. So by varying the relative timing of the excitation pulses the relative contribution of the two paths can be changed, altering the size of the target population. Another common scheme (Figure 1.1c) is the Tannor – Rice control technique [13]. In this scheme the excitation pulse puts population up in the excited electronic state, followed by free evolution. At a later time a dump pulse vertically puts the population back in the ground state, in a configuration which is close to the desired final target state. The STIRAP (Stimulated Raman Adiabatic Passage) technique (Figure 1.1b) uses a sequence of two pulses to control the population distribution in a Λ-type system [34]. Remarkable in this case is the counter-intuitive sequence of pulses. The pulse coupling the intermediary and final state comes first, even though no population is yet present there. The excitation pulse comes second, coupling the initially populated ground state with the intermediary state. These three models have been experimentally implemented and numerous variations exist at this point.

Coherent control experiments generally attempt to find specially crafted laser pulses which can maximize a certain reaction target often using Brumer – Shapiro or Tannor – Rice type mechanisms. The question is how such a shape can be found. In an ideal case the Hamiltonian of the system is completely known and the optimal pulse

shape can be fully predicted from calculations. However real systems have a complex structure and interact with the environment, making accurate theoretical predictions impossible. A practical approach to this problem has been proposed by Judson and Rabitz in a seminal paper which outlined the use of learning algorithms for coherent control [10]. The idea is to let the experimental apparatus find the optimal shape. For this the experiment needs to have a series of features. The first basic component is a fitness function, which defines the "value criterion" for each laser shape.

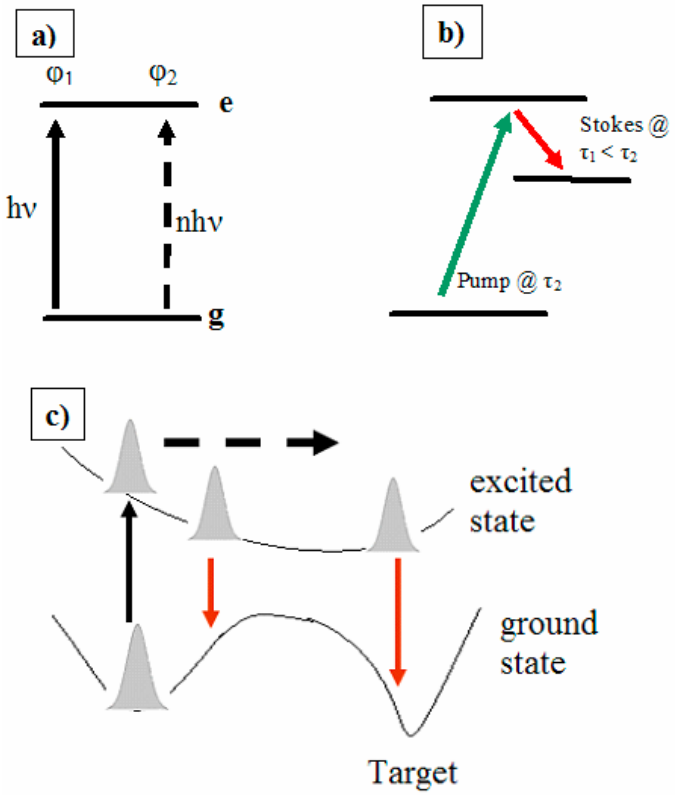

Figure 1.1. Possible mechanisms for coherent control of molecular dynamics. In a): the Brumer – Shapiro scheme of quantum pathway interference. In b): STIRAP. In c): the Tannor – Rice pump – dump technique. The horizontal arrow hints to the wave packet dynamics in the excited electronic state. All other arrows designate laser pulses. See text for details.

For example if the target molecular species has increased absorption at a wavelength λ_0 then the fitness could be the increase in absorption at that wavelength. Higher fitness is equivalent to higher absorption and higher population in the target state. The absorption at λ_0 is called the feedback signal and an excitation laser shape is performing well if the fitness function increases. The second ingredient is a method to find the optimal shape among the billions of possible laser shapes. For this task genetic algorithms proved to be an excellent tool [20, 25, 33, 35, 36]. The operation of genetic algorithms is analogous to evolution in biology. The multitude of possible laser pulses represent the "population" and the best pulses which satisfy the "survivability requirements" (high fitness) represent the "elite" which gets filtered to the top of the "population". Details about this mathematical method can be found in Chapter II. The second control experiment presented below (isomerization of retinal in bacteriorhodopsin) employs this approach for finding the optimal pulse shape. The first experiment (control of vibrational coherences in a laser dye) employs a hybrid method, where previous knowledge about the potential energy surfaces suggests that certain features of the laser pulse ("control knobs") are important. The search procedure is replaced by scanning the control knobs in a certain range to explore their impact on the target state yield.

At the present time the emphasis in coherent control experiments is three-fold. First, as mentioned above, coherent control is used as a tool to understand the underlying reaction mechanisms. By studying the characteristics of the laser shape which is able to maximize the reaction yield one can infer what "knobs" have an impact and how the molecule evolves during the reaction. Second coherent control can place the molecule in hard-to-reach states, which can then be studied with standard femtosecond spectroscopic techniques. For example, assume a certain chemical reaction has a 10:1 branching ratio between two final states. If the two states have overlapping spectral signatures (which is very often the case for broad molecular spectra in liquid phase) it is hard to do spectroscopy of the low-signal state. But if specially crafted pulses change the branching ratio to 1:10, then selective spectroscopy is possible. This example relates to one of the experiments presented below, in which spectrally blue-tuned, positive chirp pulses are able to excite almost exclusively excited state coherences in the LD690 laser dye.

Because of this selective excitation the pure oscillation frequency and dephasing time of the excited state oscillations can be measured.

LD690's attractiveness is due to a rigid structure, which allows a single strong oscillatory component at 586 cm^{-1}. This makes it an ideal candidate for vibrational control experiments. LD690 was investigated intensively by Bardeen and Shank 10 years ago [37]. They showed that linearly chirped pulses were able to control the population and the intensity of the vibrational coherences in the ground and excited electronic states of the molecule. The mechanism responsible for control is sketched in Figure 1.2. At equilibrium the ground state population is situated almost exclusively in the ground vibrational level (n = 0). The excitation pulse depicted by the blue arrow puts population in the excited electronic state, in a linear superposition of vibrational levels. This wave packet slashes back and forth in the excited state with a 56 fs period. During its motion to the right a red-tuned pulse can resonantly couple this wave packet to vibrationally excited ground state levels, enhancing the ground state coherences. This sequence (blue colors first, red colors later) does not require a multi-pulse temporal structure. A negatively chirped pulse satisfies the time-ordering criterion, as depicted in the bottom section of the plot. Alternatively, positively chirped pulses will continue to excite ground state population to the excited state across the full pulse duration, enhancing the excited state coherences.

Bardeen [37] implemented this scheme with 10 fs pump pulses, which are resonant with both the ground state absorption and excited state stimulated emission. However it is expected that the spectrum of the excitation pulses also has relevance for the process described above, and very broad pulses could complicate the analysis. In the experiment presented below we use resonant excitation with spectrally narrower pulses, of about 20 fs transform-limited duration. The narrower spectrum allows detuning of the peak wavelength which, as it is shown in Chapter III, has a strong impact on coherences. Specifically, blue spectral tuning disturbs the ground state wave function less than red-tuned excitation. At the same time blue-tuning the pump spectrum excites higher excited state vibrational levels, enhancing the excited state coherences, at the expense of the ground state counterpart. Spectral tuning in tandem with the other knob (the chirp) enables high-contrast selective excitation of the excited state coherences and their

selective spectroscopy. The oscillation frequency is found to be red-shifted compared to the ground state and the characteristic dephasing time is measured.

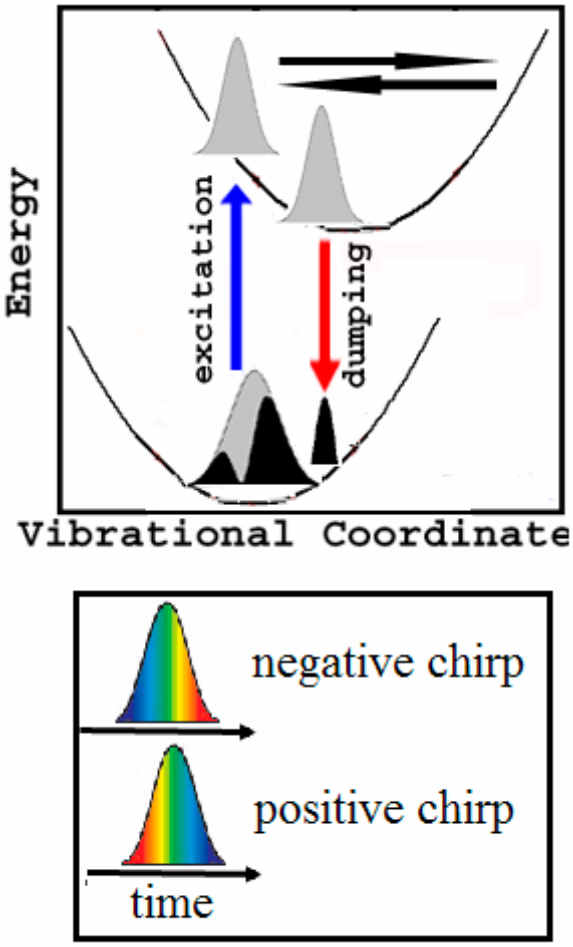

Figure 1.2. Model of vibrational coherences in LD690 (top). Bottom: illustration of color – time ordering for positive and negative chirped pulses. For a detailed description of the mechanism see the text in Introduction and Chapter III.

To our knowledge this is the first experiment in which tuning the excitation wavelength showed a strong impact on the strength of the molecular vibrations, in the ground and excited electronic states [28]. However the experiment involved linear scans of the phase and spectrum of the excitation pulses, and not a full exploration of the search space. The reason for not using fully-fledged genetic algorithm techniques is that the feedback signal requires time-consuming Fast-Fourier-Transform (FFT) analysis.

The third trend in present-day coherent control experiments is to move beyond simple molecules which have just a couple of atoms. Biological molecules in particular are very good candidates because they exhibit complex chemistry and they are large scale systems. A number of molecules in this category have already been successfully controlled [23, 30, 33, 38, 39]. The experiment described in this work aims at controlling the isomerization of retinal in bacteriorhodopsin (bR). In bR the peak of the absorption spectrum of the retinal chromophore is at 570 nm, within the reach of the laser system. An earlier study performed with 5 fs pump and probe pulses [40] showed that vibrational coherences play an important role in the isomerization reaction. The control of oscillations as a "reaction catalyst" fitted well with the expertise gained from the LD690 experiment. The bR molecule is also attractive because of its robustness (which is not the case with many other proteins), because it contains retinal, a key molecule in vision, and because of the large number of possible applications, like bio-memory storage devices or bio-electronics [41].

From the physical chemistry point of view the interest is in the ultrafast isomerization process of the retinal (all-trans → 13-cis) which is strongly assisted by the protein environment. The number of studies dedicated to retinal isomerization in bR is impressive but many questions are still unanswered [42, 43]. The complexity of the potential energy surfaces and of the corresponding broad and overlapping spectral signatures is daunting, and causes a lot of debate in the scientific community [42]. Figure 1.2 illustrates the potential energy diagram of the retinal molecule. This so-called "three-state" model is the one which to date provides the best explanation of the experimental results presented in literature [43]. A simple inspection shows that at least six distinct conformers are involved. The black arrows indicating the possible molecular evolution form an intricate pattern of possible (and intersecting!) pathways.

The goal of the experiment is to control and understand the isomerization reaction. A similar study has been published less than two years ago [33], in the biologically relevant low intensity excitation regime. It found that a train of pulses separated by ~ 145 fs (or 230 cm^{-1}) maximizes the 13-cis yield (see Figure 1.2). The two numbers are close to the period and frequency normally assigned to the torsional mode. The experiment described below uses excitation intensities two orders of magnitude

higher and finds that a transform-limit pulse (i.e. the shortest pulse possible for a given spectral bandwidth) maximizes the isomerization yield.

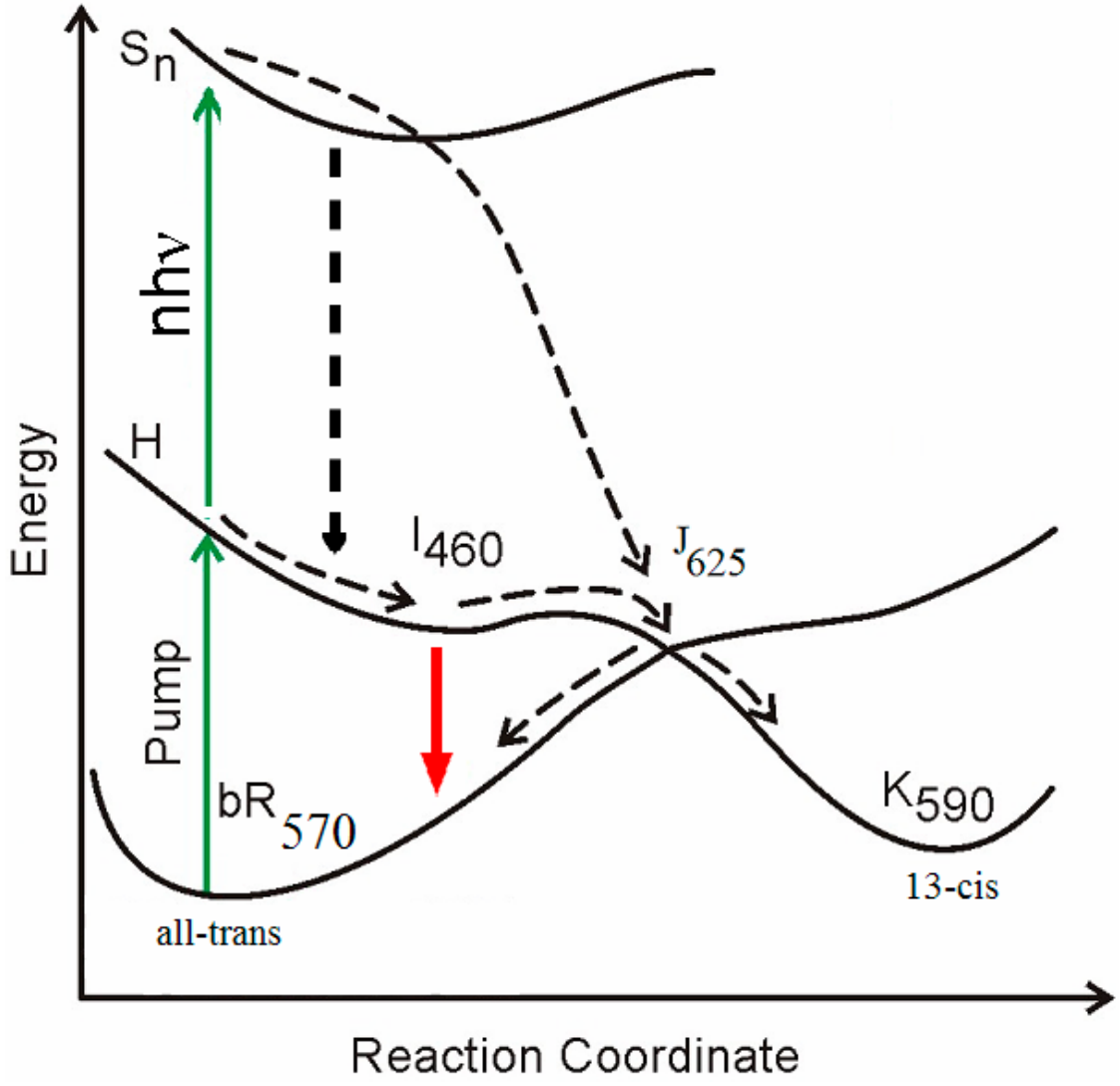

Figure 1.3. Model of the electronic potential energy surface structure for retinal in bacteriorhodopsin. The green arrows illustrate the excitation pulse. The red arrow illustrates the $I_{460} \rightarrow$ all-trans transition. The dashed arrows illustrate non-radiative internal conversion processes between different states. J_{625} is tentatively assigned to the upper region of the conical intersection. See Chapter IV for more details.

At low intensity there is no sensitivity of the yield on pulse shape. This result contrasts with the solution found in the low-intensity study. However the signal-to-noise ratio in the cited work was significantly better and this may have been a critical factor in the experiment. In the low intensity regime the maximum increase of the isomerization yield translates into an absorption change of 2 – 3 mOD [33]. This figure is at the limit of our signal-to-noise ratio.

Another control experiment has been performed by Gerber et al. [39]. Transform-limited pump pulses are used to excite population which subsequently evolves in the first excited electronic state. A shaped dump pulse is used to put the population back in the ground state, before it is able to reach the conical intersection region (see Figure 1.3. The dump pulse is represented by the dashed arrow pointing from I_{460} to all-trans). This control scheme is similar to the Tannor – Rice scheme shown in Figure 1. A transform-limited pulse is found to dump most efficiently the population back to the ground state suggesting that the wave packet has a narrow spread along the reaction coordinate. This control scheme allows only a decrease, not an increase of the isomerization yield.

As mentioned above, the results presented in this work show that a high intensity, very short pulse is maximizing the 13 – cis isomerization yield. A number of complementary measurements are performed in order to understand this result. The model uncovered involves multiple excitation pathways (see Figure 3) which are not accessible under normal ambient light excitation. At high intensity the S_n pathway allows bypassing of the I_{460} region. In addition to this effect, the population which still goes through the I_{460} conformation decays faster. This is expected since at high intensity more energy is put into vibrationally hot levels and a hotter wave packet would cross faster the small barrier at the right of the I_{460} shallow bottom. I_{460} is strongly coupled to the all-trans ground state, as shown through stimulated emission measurements. Avoiding it minimizes the losses on the way towards the conical intersection. The branching ratio at the conical intersection also appears to be influenced by the excitation parameters. This last point needs further experimental confirmation.

It is expected that for low excitation, “sun-like” intensity the molecule is performing its job in a robust and efficient manner, perfected in billions of years of evolution. It is interesting that nature appears to have over-designed the molecule,

allowing for much more efficient (S_n – related) pathways under conditions reachable only in lab conditions. From this perspective the results presented in this work encourages a deeper look at bio-molecules, which could potentially uncover chemistry not normally anticipated from these systems.

The coherent control field evolves continuously, the target being the control and understanding of larger and more complex molecules. The results presented in this dissertation open the door towards a number of directions. The LD690 experiment suggests that by simultaneously using spectral tuning and chirp selective excitation and, potentially, breaking of bonds is possible. This could be a tool for selective dissociation chemistry. The bR isomerization experiment opens the door for studying a variety of biological molecules containing visible-absorbing chromophores. The intensity regime appears to be a very important factor. The ensuing analysis reveals complex molecular dynamics (see Figure 3) which could be a starting point for understanding other bio-molecules. The question if coherence plays a role in these large scale molecules is kept open. The low intensity experiment mentioned above supports this assertion but the high intensity experiment reported here does not point to any coherence effects.

Chapter II

Experimental Setup

The laser setup described below is the one employed for the LD690 experiment, performed at University of Michigan at Ann Arbor. The system used at Stanford, for the bacteriorhodopsin experiment, has a single major difference compared to the other one: the root system generating the 800 nm laser light is a fully commercial, hands-off Ti: sapphire laser.

2.1 The Ti: sapphire laser system

The Ti: sapphire laser system used in the LD690 experiment (see Figure 2.1) is based on a standard industry design [4, 44, 45]. The first element in the laser chain is the oscillator (KML Labs), in which a Ti: sapphire crystal placed in the center of a resonant cavity is pumped by a high power continuous wave green laser (Millennia, Spectra Physics). The oscillator generates a train of broadband laser pulses with 800 nm peak wavelength and about 3 - 4 nJ pulse energy. The repetition frequency is dictated by the length of the laser cavity and is of the order of 100 MHz. The problem with this system is the low energy per output pulse. To increase the pulse energy, an amplifier is used, in which the weak ultrafast pulse (seed) overlaps with a high energy pulsed green pump beam in another Ti: sapphire crystal. Because of potential crystal damage at high intensity the green pump light has a long duration, of about 150 ns. The power of the green laser is about 6.5 W at 1 kHz repetition rate. To insure good amplification of the seed, two preparatory steps are needed. First the repetition rate of the seed train of pulses is reduced to 1 kHz by means of a Pockels cell and a

polarizer. Each millisecond the Pockels cell rotates the polarization of one of the seed pulses, allowing its transmission through the polarizer. Secondly, for a good time overlap the seed pulses are stretched in time to a couple of picoseconds and sent through the crystal 8 times. Each pass "steals" more energy from the green pump. After amplification, the output pulses are recompressed. Both the compressor and the stretcher are standard gratings-based devices. The typical output parameters of this laser system are: 70 fs full-width-half-maximum (FWHM) duration, 600 μJ pulse energy and 1 kHz repetition rate.

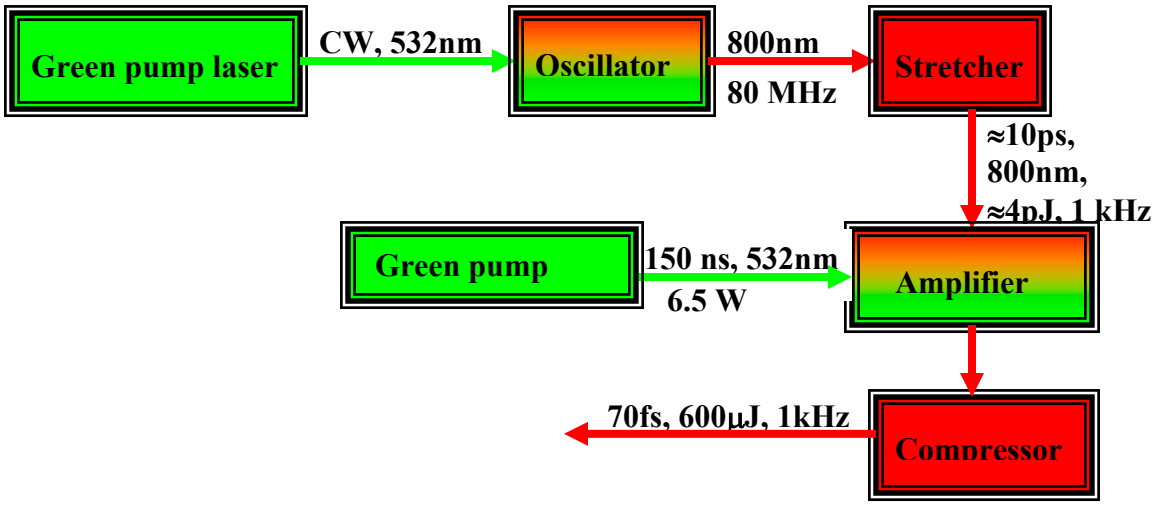

Figure 2.1. The femtosecond Ti: sapphire laser system. A CW green laser pumps the Ti: sapphire oscillator, delivering short, weak pulses at 800 nm. The pulses are temporally stretched by ~ 100, sampled at 1 kHz and sent into a power amplifier pumped by a pulsed green laser. The compressor corrects the stretcher's and amplifier's dispersion, producing 70 fs pulse duration.

The laser used for the bacteriorhodopsin experiment, which took place at Stanford University, is a fully commercial system (Thales Femtocube), able to deliver 40 fs, 2.5 mJ pulses.

As presented above, the laser delivers coherent light with some of the desired properties: high energy and high repetition rate. However, the 800 nm wavelength and the duration do not match the requirements of the coherent control experiments reported below. An important class of interesting molecular systems absorbs in the visible range of the electromagnetic spectrum and the time resolution needed to

observe their motion is about 5 times smaller than our pulse duration. As a consequence, a device was built which, by using the 800 nm pulses as input, can deliver laser radiation fulfilling the two above-mentioned requirements (wavelength and pulse duration).

2.2 The NOPA

Non-collinear optical parametric amplifiers (NOPA) are devices which produce tunable, broadband pulses [2, 46, 47]. The wavelength range spans the visible spectrum from 470 nm to the near infra-red region. The shortest pulses created with this type of device are 3.7 fs long [5, 21]. A range of non-linear phenomena are at the core of this technology: white-light generation, second harmonic generation and parametric amplification.

2.2.1 Introduction to Nonlinear Optics

Before going into the details of the NOPA design the basics of the nonlinear optics theory are briefly summarizes [48]. When light travels through a medium it generates an electronic response and the dielectric polarization in the material can be expressed as a power series of the electrical field of the incident laser pulse:

$$\vec{P} = \varepsilon_0 \chi \vec{E} \tag{2.1}$$

Or

$$\vec{P} = \varepsilon_0 \left[\chi_{ij}^{(1)} E_j + \chi_{ijk}^{(2)} E_j E_k + \chi_{ijkl}^{(3)} E_j E_k E_l + ... \right] \tag{2.2}$$

Here the coefficient $\chi^{(i)}$ is the ith order susceptibility tensor of the medium. The first term describes the linear optics regime while the next terms give rise to nonlinear effects. Among these, second harmonic generation (SHG) and white light generation (WLG) are widely used in femtosecond experiments.

2.2.1.1 White-light generation

White light (WL) generation can be observed when an ultrashort laser pulse is focused in a transparent medium with a strong nonlinear coefficient. Since its first observation in 1970 [49], it has been observed in a large range of solids, liquids and gases [50, 51]. The dominant factor responsible for WLG is the self-phase modulation process but it has been argued that plasma creation, multi-photon processes and nonlinear Raman scattering play an important role as well. The literature in the field is rich and below only the key theoretical points are presented.

In the simple case of linearly polarized light the formula above is reduced to

$$P = \varepsilon_0 \left[\chi^{(1)} + \frac{3}{4} \chi^{(3)} |E|^2 \right] E \tag{2.3}$$

This equation leads to a well known formula for the non-linear index of refraction:

$$n \approx n_0 + n_2 I \tag{2.4}$$

An important consequence of Equation 2.4 is the self-focusing effect. For a Gaussian beam the intensity is higher in the center compared to the wings so the index of refraction will have a gradient and a beam-induced focusing lens will be created, resulting in even higher intensity. The threshold power for this process is

$$P_{crit} = \frac{a\lambda^2}{8 n_0 n_2} \tag{2.5}$$

Here *a* is a characteristic parameter with values between 3.8 and 6.4, λ is the laser wavelength and n_0, n_2 are the refraction indices. The resulting high intensity triggers another process called self-phase modulation, which is responsible for the spectral broadening. The equation describing the propagation of a traveling wave is

$$E(z,t) = E_0(z,t) e^{\varphi(t,z)} = E_0(z,t) e^{-i(kz - \omega_0 t)} \tag{2.6}$$

The wave vector k is given by

$$k = n \frac{\omega_0}{c} = (n_0 + n_2 I(t)) \frac{\omega_0}{c} \tag{2.7}$$

This means that the phase is equal to

$$\varphi(t,z) = \omega_0 t - (n_0 + n_2 I(t))\frac{\omega_0}{c} z \tag{2.8}$$

And the instantaneous frequency is

$$\omega(t) = \frac{\partial \varphi(t)}{\partial t} = \omega_0 - n_2 \frac{\omega_0}{c} \frac{\partial I(t)}{\partial t} z \tag{2.9}$$

For an ultrashort pulse the intensity envelope I (t) changes fast, resulting in a large $\omega(t) - \omega_0$ spectral broadening. Inside the nonlinear medium a series of other effects distort the pulse envelope, making it asymmetrical and cause an asymmetric spectral broadening. Always the short wavelength (blue) wing of the broadened spectrum is much wider than the red wing.

In the experiments reported here the WL generation technique is used twice, first in the NOPA, to create the broadband seed, and second to create the probe which will monitor the molecular dynamics after laser excitation. Given this major role, extreme care has to be taken in order to insure that the WL is stable and of high temporal and spatial quality. These characteristics can be realized simultaneously if a number of conditions concerning the pump beam, the nonlinear medium and the focusing geometry are fulfilled. The 800 nm pump needs to be compressed and of very good spatial quality. Its intensity has to be very close to the critical power for self-focusing, which for our experimental setup is ≈ 1 μJ. The best nonlinear medium is sapphire because of its high nonlinearity and excellent resistance to laser damage. A typical WL spectrum created with a f = 100 mm lens in a 2 mm sapphire plate is presented in Figure 2.2.

The continuum extends from 450 nm to 820 nm, with a smooth anti-Stokes plateau from 750 nm to 600 nm. The green peak around 550 nm can be tuned by varying the focal length of the lens. The spectral region around 800 nm has been attenuated in order to acquire this spectrum. The anti-Stokes wing accounts for only ≈ 10% of the total energy. For comparison purposes in Figure 2.3 we present the WL spectrum generated in ethylene glycol. The anti-Stokes wing has more energy and is much broader. Other options for extending the WL bandwidth are solid state materials with very large band gaps like CaF_2 or LiF. However they have a low damage threshold and in our tests the WL intensity dropped to zero in ≈ 15 minutes. Ethylene glycol is the best choice since it has an extremely broad WL spectrum and it does not have damage issues (when flowing)

but it requires a smooth flow system. It has been used occasionally for WL probe generation.

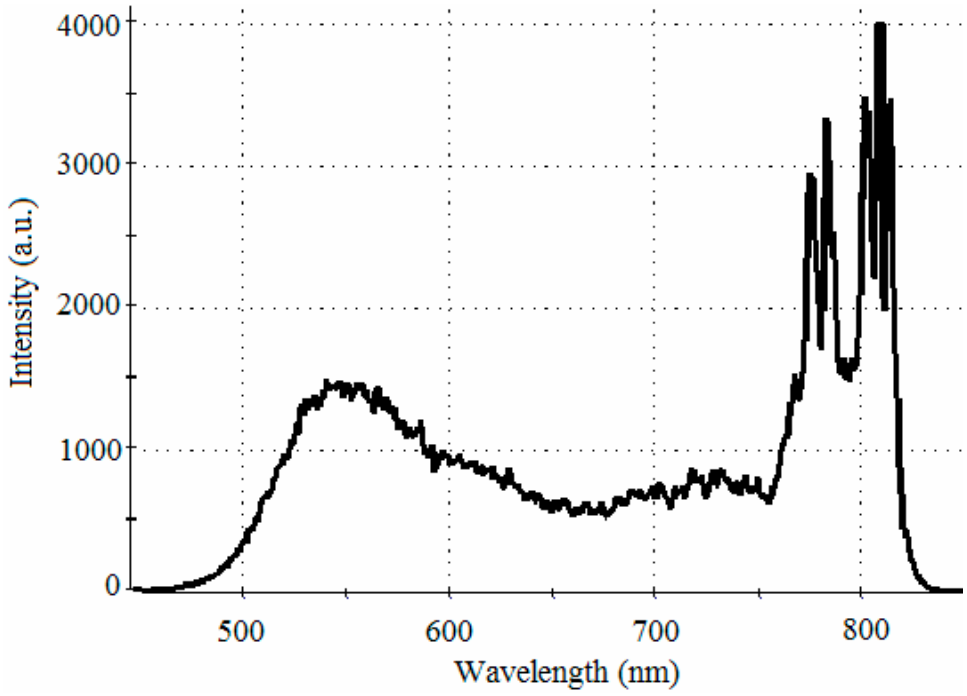

Figure 2.2. Typical white-light spectrum in a sapphire plate. The strong 800 nm component is attenuated by a filter.

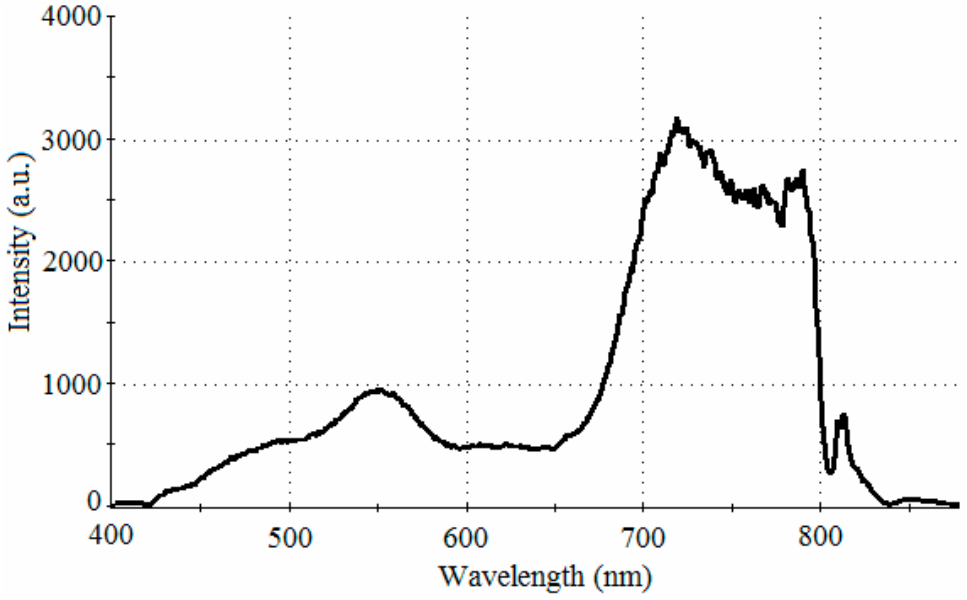

Figure 2.3. Typical white-light spectrum generated in a jet of ethylene glycol.

An important issue is the group velocity dispersion (GDV) of the WL pulses, which needs to be known and extracted from the ultrafast dynamics measurements. For this purpose transient TL pump – WL probe scans are done in a medium which does not absorb at the pump or probe wavelength [52]. The pump changes the polarization of the medium (Kerr effect) resulting in a rotation of the polarization of the probe beam, which is measured with a crossed – polarizers setup. Since the effect is instantaneous it allows the direct measurement of the probe chirp. The measurement shown in Figures 2.4 and 2.5 has been done in ethylene glycol and it shows that the WL chirp is small and almost linear with a GD of ≈ 1.5 fs/ nm (see the right-hand panel of Figure 2.5). A cross section done at 570 nm is presented in Figure 2.5, left panel. The plot reveals the time of maximum temporal overlap between the pump and probe pulses, $T_0 \approx$ - 275 fs, which is used to "set the clock" for the ultrafast dynamics. If the timings of all the peaks for individual WL wavelengths are extracted, they can be plotted as shown in the right panel of Figure 2.4, which graphically illustrates the delay between individual spectral components.

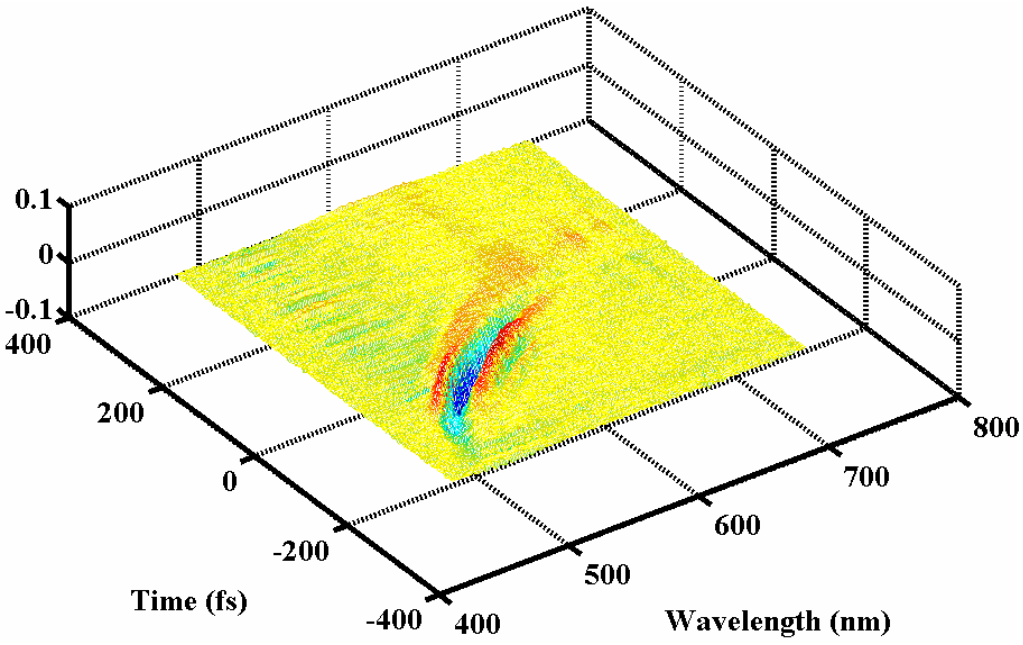

Figure 2.4. A typical 2D plot of a pump – probe transient scan in a non-resonant liquid medium (Kerr effect measurement). The curvature of the groove depicts the order in time of the spectral components of the probe pulse.

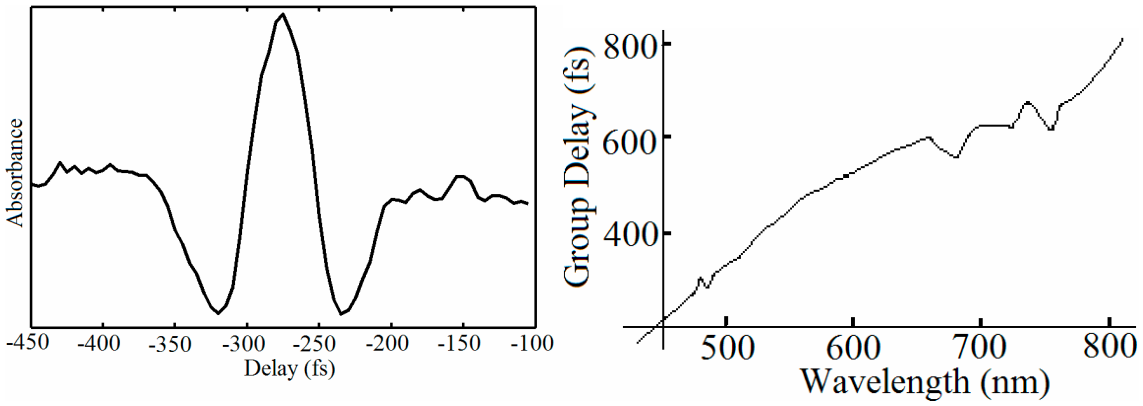

Figure 2.5. Left panel: a section through Figure 2.4, at 570 nm. Right panel: a plot of the timings of the peaks, collected from plots similar to that shown in the left panel.

The propagation of the broadband pulse through the experimental setup creates additional challenges. Lenses, mirrors and air itself contribute to the temporal stretching of the pulse [27, 53, 54]. The dispersion equations for air are presented below [55]. The constants k, k_1, k_2 and k_3 are experimentally derived fit parameters. By using this equation and the group velocity equation the GD is found to be about 60 fs between 450 nm and 800 nm for 1 m of air propagation.

$$n_{air}(\lambda) = 1 + \left(\frac{k}{k - \frac{1}{\lambda^2}} + \frac{k_3}{k_2 - \frac{1}{\lambda^2}}\right) \times 10^{-8} \tag{2.10}$$

$$v_{air}(\lambda) = \frac{c}{n_{air}(\lambda) - \lambda \times \frac{\partial n_{air}}{\partial \lambda}} \tag{2.11}$$

The use of lenses has been carefully minimized but mirrors present similar dispersion issues. The lab setup employs typical dielectric broadband mirrors, whose dispersion has been previously characterized in literature [53]. For metallic mirrors the total GD is a few femtoseconds across the visible spectrum and it can be neglected. However the dielectric mirrors exhibit significant negative dispersion. Sometimes this property is used to partially compress the broadband pulses. One problem is the sharp profile around 600 nm [53]. Ideally a compressing device should offer a smooth GD

correction over the full spectrum. The discussion about the issue of dispersion will be detailed below (vide infra).

2.2.1.2 Second harmonic generation

SHG processes are part of a larger class of nonlinear parametric phenomena, which are instrumental in the production of intense laser light at wavelengths other than those characteristic for Ti: sapphire lasers [56, 57]. NOPAs are pumped with SHG light produced by doubling the 800 nm Ti: sapphire laser light to 400 nm. In this section the key formulae concerning SHG are presented in an abbreviated form. If equation 2.2 is converted to the frequency domain the second order term in the expansion is given by

$$P(2\omega) = 2\varepsilon_0 d_{eff}(2\omega;\omega,\omega)E^2(\omega) \tag{2.12}$$

Here $2d_{eff} = \chi^{(2)}$. In the slowly varying envelope approximation and for negligible loss in the material, the wave equation is given by:

$$\frac{\partial E(2\omega)}{\partial z} = -\frac{i\omega}{n_{2\omega}c} d_{eff} E^2(\omega) e^{i\Delta kz} \tag{2.13}$$

Here $\Delta k = k(2\omega) - 2k(\omega)$. In the limit when the conversion efficiency is low the amplitude of the pump field remains approximately constant and the equation can be solved giving a very important formula:

$$I(2\omega, l) = \frac{2\omega^2 d_{eff}^2 l^2}{n_{2\omega} n_{\omega}^2 c^3 \varepsilon_0} \left(\frac{\sin(\Delta kl/2)}{\Delta kl/2}\right)^2 I^2(\omega) \tag{2.14}$$

A number of conclusions can be reached from the above equation. First of all the intensity of the SHG light is proportional to the square of the intensity of the incoming light. This means that to obtain high conversion efficiency energetic, ultrashort laser pulses focused at a very small spot size should be employed. In practice a series of limitations exist: the SHG crystals have a finite damage threshold level which prevents tight focusing. Secondly the intensity of the SHG light is proportional to the square of l, the crystal length, and it would appear that using very long crystals would result in very high conversion efficiency. However the SHG bandwidth correlates negatively with the crystal length such that a thick crystal would allow the doubling of just a narrow section

of the pump spectrum. This issue would negatively affect the performance of the NOPA. The typical SHG BBO crystals employed in NOPA devices have 1 mm thickness. This number represents a good compromise between efficiency and bandwidth.

An inspection of Equation 2.14 shows that for high efficiency we need to satisfy the condition

$$\frac{\sin(\Delta kl/2)}{\Delta kl/2} = 1 \tag{2.15}$$

Equation 2.15 leads to the phase matching formula

$$\Delta k = k(\omega) - k(2\omega) = 0 \tag{2.16}$$

This condition is satisfied by cutting the BBO crystal at an angle of 29.2^0 (for phase matching of 800 nm and 400 nm light). A large SHG spectrum obtained in our lab is presented in Figure 2.6. This spectrum has a FWHM bandwidth of 12 nm and 30% conversion efficiency.

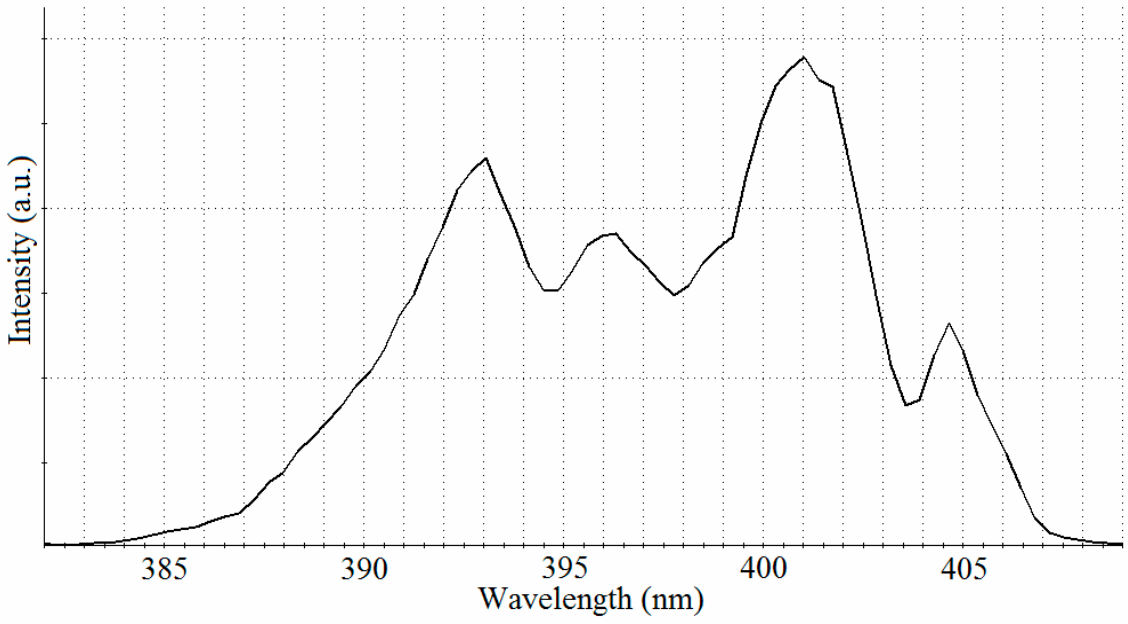

Figure 2.6. A sample spectrum of the blue pump. The FWHM is larger than 10 nm. For regular NOPA operation (i.e. ~ 20 fs output pulses) 5 nm FWHM is sufficient.

2.2.1.3 Pulse Propagation in air

The quality of the NOPA output pulses is intimately connected to the propagation of the near-IR pump pulses, which have to travel ~ 3.5 meters before reaching the NOPA setup. We found that their temporal, spatial and spectral profiles change significantly during air propagation. The spatial profile is actually somewhat improved due to self-focusing effects in air but a significant change has been observed for the spectral profile. Figure 2.7 shows the pump spectrum after the 800 nm compressor (left panel) and before the NOPA (right panel). The spectrum narrows and acquires sharp features which affect the spectrum of the blue pump light because this is derived directly from the spectrum of the fundamental. The spectral modulations get transferred to the NOPA output spectrum. One way to minimize this effect is to attenuate the power of the near-IR pulses from 550 nJ to less than 400 nJ. By doing this both the smoothness and the output power improved.

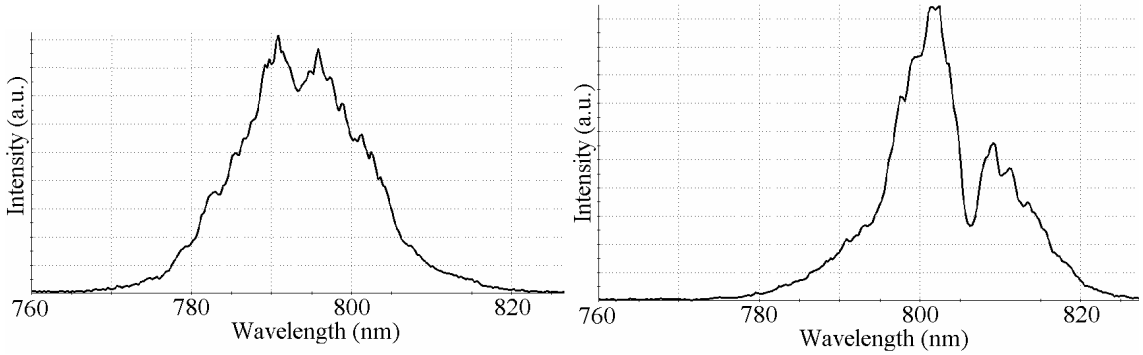

Figure 2.7. The 800 nm spectrum right after the amplifier (left panel) and after propagation through more than four meters of air (right panel). The pulse energy is about 600 μJ, the duration about 70 fs (after compressor). The spectrum experiences a range of non-linear effects, resulting in spectral modulation and spectral shift.

2.2.2 Large Bandwidth NOPA

In the development stage of the experiment we attempted to create ultra-broadband pulses, compressible to 5 fs. The WL seed supports enough bandwidth to reach this figure. However two other obstacles have to be overcome in order to reach this target. The first is the difficulty to amplify the extremely broad bandwidth required. The

NOPA BBO crystals allow a limited amplification bandwidth [2]. In a typical NOPA design, the pump beam (400 nm) and the WL seed cross inside the crystal at an angle $\alpha_{\text{int}\,ernal}$. The group-velocity matching condition in a BBO crystal is

$$V_g^s = V_g^i \times \cos(\alpha_{\text{int}} + \beta) \tag{2.17}$$

Here V_g^s *and* V_g^i are the group velocities for the signal and idler respectively and β represents the angle between the pump and the idler beam. This leads to the NOPA tuning equation, in which the crystal's angle θ is expressed as a function of λ, the seed wavelength, and Λ, the pump wavelength.

$$\theta(\lambda, \Lambda, \alpha_{\text{int}}) = \arccos \sqrt{\frac{\left(\frac{n_E(\Lambda)}{n_e(\lambda, \Lambda, \alpha_{\text{int}})}\right)^2 - 1}{\left(\frac{n_E(\Lambda)}{n_e(\Lambda)}\right)^2 - 1}} \tag{2.18}$$

Figure 2.8 presents the beam geometry (upper panel) and the tuning curves for three different wavelengths within a typical pump bandwidth, each at its own optimized angle (lower panel) [58]. The three pump wavelengths can have different incidence angles if a dispersive element (a prism) is inserted in the pump path. This apparently complicated figure is easy to understand. By rotating the crystal angle we move the horizontal dashed line in the vertical direction. This line intersects each of the three curves at certain wavelengths. It crosses the lower curve at 500 nm, the middle one over a wide spectrum, between 540 nm and 720 nm and the upper one at 830 nm. This means that for that crystal angle ($\theta = 30.5^0$) and for this blue pump bandwidth (402 nm – 407 nm) the amplified spectrum will extend from 500 nm to 830 nm. A more formal way to formulate this is presented below.

If the goal is to amplify a large bandwidth then one should identify the value of α for which the function θ (λ) is the flattest at the central pump wavelength. Each curve is characterized by a flatness merit function defined as

$$F = \sqrt{\overline{\theta(\lambda)}^2 - \overline{\theta(\lambda)^2}} \tag{2.19}$$

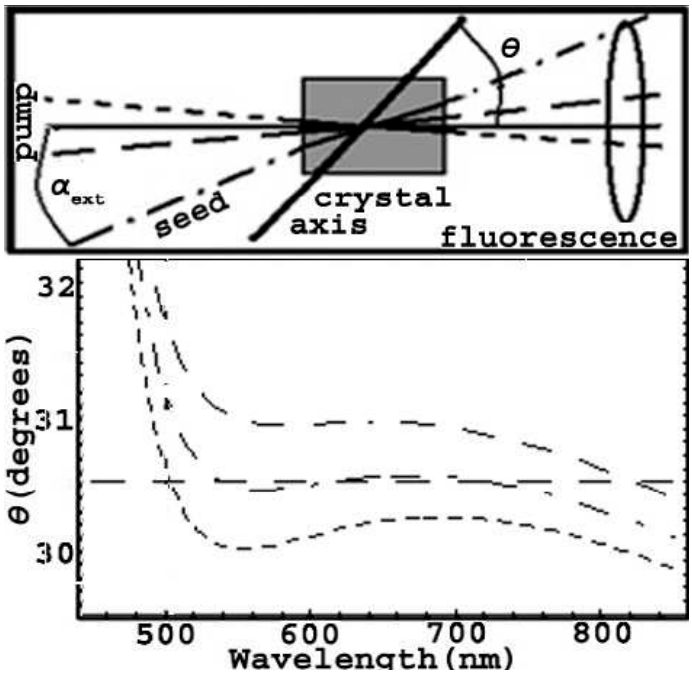

Figure 2.8. Top: the non-collinear geometry (the continuous, dotted and dashed lines represent the angularly dispersed pump beam for three pump wavelengths, the dashed-dotted line represents the seed beam, the thick continuous line is the crystal axis and the circle depicts the chirp-free fluorescence cone). The beams propagate from left to right. Bottom: NOPA tuning curves for $\alpha=3.4^{o}$ & $\lambda=407$ nm (dotted), $\alpha=3.5^{o}$ & $\lambda=405$ nm (dashed-dotted), $\alpha=3.7^{o}$ & $\lambda=402$nm (dashed line) respectively.

The averages are obtained by integrating the curve over the target spectral interval, from $\lambda_{\min}$ *to* $\lambda_{\max}$:

$$\overline{\theta(\lambda)} = \frac{\sum_{i=0}^{N} \theta(\lambda_{\min} + (\lambda_{\max} - \lambda_{\min}) \times \frac{i}{N})}{N+1} \tag{2.20}$$

A similar formula is used for $\overline{\theta(\lambda)^2}$. Table 2.1 shows the result of the calculation for $\lambda_{pump} = 405\,nm$ and a target bandwidth extending from 530 nm to 750 nm.

3.2^0	3.3^0	3.4^0	3.5^0	3.6^0	3.7^0
0.17	0.12	0.08	0.04	0.05	0.1

Table 2.1. The flatness parameter versus α

The optimal angle is $\alpha_{\text{int}} = 3.5^0$ or $\alpha_{ext} = 5.8^0$ if refraction is taken into account. As described above, in Figure 2.8 a horizontal line at 30.5^0 overlaps with most of the $\alpha = 3.5^0$, $\lambda_{pump} = 405\,nm$ curve and reaches the $\alpha = 3.7^0$, $\lambda_{pump} = 402nm$ curve at 505 nm and the $\alpha = 3.4^0$, $\lambda_{pump} = 407nm$ curve at 830 nm, implying that a spectrum extending from 500 nm to 830 nm can be amplified if the pump has an angular divergence of 3.7^0 – 3.4^0 = 0.3^0 over its 5 nm FWHM bandwidth. This was accomplished by inserting a Pellin-Broca prism in the pump's path. Figure 2.9 shows the NOPA setup designed specifically for ultra-broad band amplification.

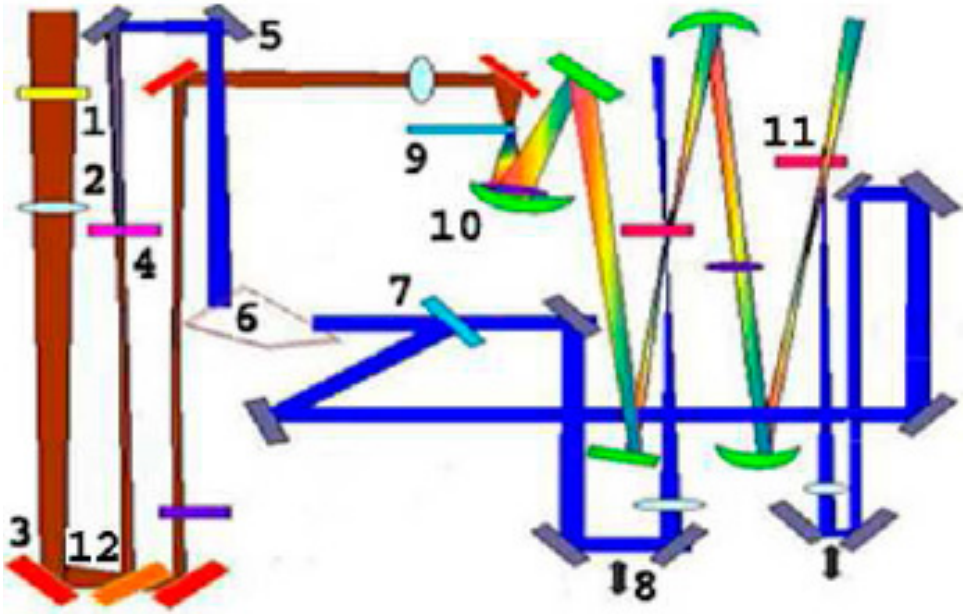

Figure 2.9. The Pellin-Broca prism based NOPA setup. 1: λ/2 plate, 2: FS lenses, 3: 800nm mirrors, 4: SHG BBO crystal (1mm, EKSMA), 5: 400nm mirrors, 6: Pellin-Broca prism, 7: 400nm beamsplitter, 8: translation stages, 9: 2.4mm sapphire plate, 10: white light mirrors (BD1 or ER2, from NRC), 11: 2mm BBO crystals, cut at 31.5^0, AR coated for visible (Kaston), 12: R=99% 800nm mirror.

The pump FWHM extends from 402 nm to 407 nm (see Figure 2.10, bottom right-side panel) and the required angular divergence is ≈ 0.06^0/nm. The angular chirp and the temporal stretch induced by the fused silica prism, obtained from a self-made ray tracing model, are 0.013^0/nm and ~ 400 fs. For focusing the blue pump a f = 200 mm lens is chosen. It is placed at 45 cm after the PB prism's exit face for the first pass, and a 300 mm focal length lens placed at 75 cm for the second pass. In this configuration the angular chirp of the pump becomes close to the theoretical figure. It is known that in this

geometry the blue pump beam generates a fluorescence cone, containing a rainbow of colors (see figure 2.8, upper panel). Normally these colors are angularly dispersed. However, when the pump is spectrally dispersed as described above the cone narrows and all colors are propagating at the same angle. This represents a visual confirmation of the success of the approach

A portion of the 800 nm input light is focused in a 2.4 mm sapphire crystal and generates a WL seed pulse of less than 1 ps duration. The intensity and the spatial profile of the 800 nm light are tuned with the aid of a variable neutral density filter and with an iris. The compressor is optimized for obtaining the best white light generation and not for generating the most intense blue light. Both processes require transform-limited pulses but due to the different dispersions of the 800 nm beam in the blue-generating and WL-generating arms the SHG efficiency is sub-optimal. It is critical to have the 800 nm beam perfectly aligned along the geometrical axis of the focusing lens. If this is not the case the WL beam will be spatially chirped, with adverse effects on the amplification process. Depending on the bandwidth which one desires to amplify the temporal profile of the WL pulse can be manipulated to match the duration of the pump pulse, which in general is shorter. The WL is steered to the BBO crystals using highly reflective BD1 mirrors (Newport Research Corporation), which impart about −50fs group delay per reflection over the visible spectrum (vide supra). This results in partial seed compression and increases the amplified bandwidth. It is possible in principle to bounce the WL pulse many times off these mirrors to obtain even better compression. Alternatively, when the experiment required narrower NOPA pulses the WL pulse is stretched by inserting UV fused-silica slabs. There is a trade-off between the bandwidth and the energy of the amplified pulses. For long WL seed pulses only a narrow spectrum matches the pump temporal window but the amplification efficiency is very high, because we can optimize very precisely the alignment of the NOPA crystals to match that particular narrow bandwidth. For short seed pulses the amplified bandwidth is much larger but the overall efficiency is quite low. For the ultra-broad band version of the device the output is a 1.5 μJ pulse with Gaussian spatial profile, and a spectrum extending between 500 nm and 830 nm (Figure 2.10, upper panel). The total output of the NOPA is ~ 30 μJ, but the spatial and temporal quality is poor because of amplification of spurious background

components. The collimation system of the output beam is located 1 m after the NOPA allowing a good separation between signal and background. No spatial chirp is observed in the output beam and the focus size which can be obtained is close to the theoretical minimum.

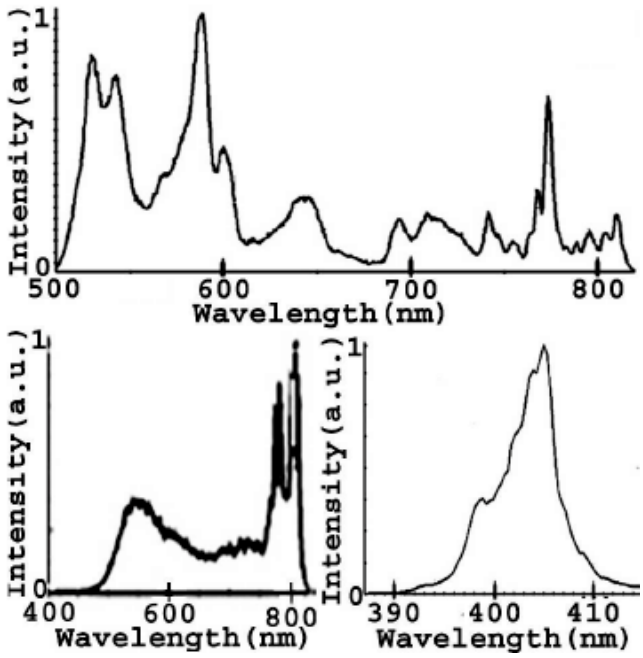

Figure 2.10. The NOPA spectrum (top), the pump (bottom right) and the seed spectrum (bottom left).

The spectrum obtained in this ultra-broadband NOPA version presents multiple spectral modulations but FROG measurements revealed a dominant linear chirp component. This means that the pulse is compressible to a very short duration, provided that one can manipulate the full bandwidth. Broadband pulses with much stronger modulations and similar bandwidths, generated in fibers have been successfully compressed by a number of researchers [59, 60]. However this requires large aperture spatial light modulators and very carefully designed compressors. Since the experiments presented in this work do not need sub-10 fs pulses, the complete compression of the spectrum presented in Figure 10 has not been pursued. Instead the NOPA is adjusted to amplify ~ 70 nm bandwidth, enough for producing 15 - 20 fs pulses. The output energy increased correspondingly to a couple of μJ.

2.3. Pulse Shaping

2.3.1. Theoretical introduction

The electric field of a laser pulse can be written in the frequency domain as [61]:

$$E(\omega) = \left|E(\omega\right| \exp[i\Phi(\omega)] \tag{2.21}$$

The phase is given by

$$\Phi(\omega) = \vec{k}\,\vec{r} - \omega t + \phi(\omega) \tag{2.22}$$

The light is perfectly compressed if the phase is the same across the full frequency range. This condition can be written as $\frac{\partial\Phi(\omega)}{\partial\omega} = 0$, which, assuming a non-dispersive medium (i.e. $\frac{\partial k}{\partial\omega} = 0$) gives

$$t(\omega) = \frac{\partial\phi(\omega)}{\partial\omega} \tag{2.23}$$

Here t (ω) should be interpreted as the arrival time of each frequency component. The expression for the phase of the electric field can be expanded in a Taylor series as:

$$\phi_{LCM}(\omega_i) = \phi_{LCM}(\omega_0) + \frac{1}{1!} * \frac{d\phi}{d\omega}\bigg|_{\omega_0} \times (\omega_i - \omega_0) + \frac{1}{2!} * \frac{d^2\phi}{d\omega^2}\bigg|_{\omega_0} \times (\omega_i - \omega_0)^2$$
$$+ \frac{1}{3!} * \frac{d^3\phi}{d\omega^3}\bigg|_{\omega_0} \times (\omega_i - \omega_0)^3 + \frac{1}{4!} * \frac{d^4\phi}{d\omega^4}\bigg|_{\omega_0} \times (\omega_i - \omega_0)^4 \ldots \tag{2.24}$$

Here i denotes the pixel number and ω_i is the frequency of the light passing through that pixel. The first two terms will give a zero and a constant contribution for t(ω) so they can be dismissed. The derivative of the third term gives a linear function of ω, which is known as the group delay dispersion (GDD). The fourth term gives a quadratic function of ω, which is the third order dispersion (TOD). The GDD is responsible for the linear chirp and the TOD is responsible for the quadratic chirp of the laser pulse. Higher order terms are progressively smaller. The equation suggests a natural way to control the phase of the laser light. If one can individually access each frequency

ω of the spectrum and manipulate its phase then control of the full phase profile of the pulse can be accomplished.

2.3.2 Practical aspects

An essential feature in ultrafast chemistry experiments is the capability of shaping the excitation pulses [10, 13, 16, 35, 61]. Laser light has a number of characteristics such as duration, energy, spectrum, polarization, spatial and phase profile which can change the way the photo-chemical reactions take place. A series of phase and amplitude shaping methods have been developed for controlling all these properties. Pulse shaping technology is at a mature stage and a large range of devices and techniques are available. This section presents only the techniques implemented in this work [35, 36]. A typical pulse-shaping setup is presented in Figure 2.11.

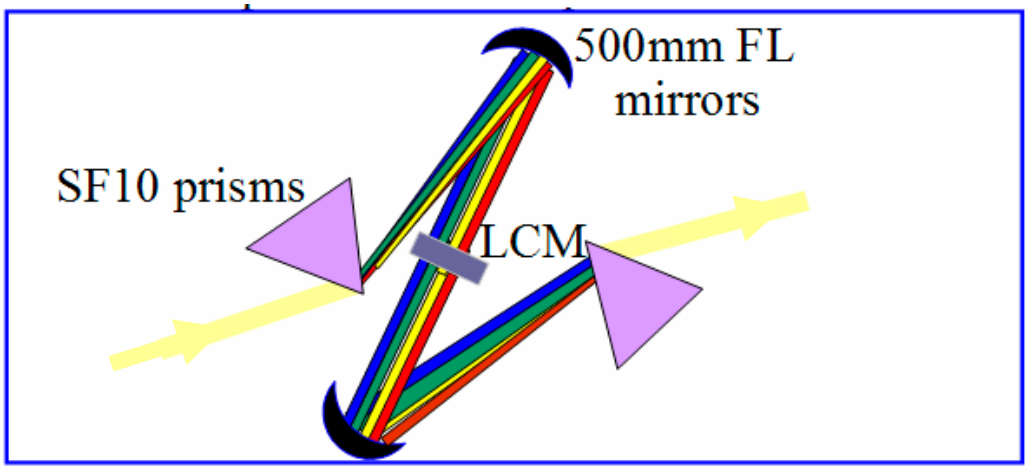

Figure 2.11. Schematic presentation of a 4f pulse shaping setup. Light propagates from left to right, as the arrows indicate. A broadband "white-light" beam is dispersed by the first SF10 prism (other materials can be used, too) and is spectrally collimated by the spherical mirror. In the liquid crystal modulator (LCM) each "color" passes through a different pixel, with a different effective index of refraction. The second mirror – prism pair reassembles the beam, without any spatial chirp.

First the laser pulse is dispersed with the aid of a dispersive element such as a prism or a grating. There are a couple of differences between the two alternatives. Gratings tend to be lossier but they induce a larger angular dispersion. They produce linear wavelength dispersion while prisms produce linear frequency dispersion [59]. As

seen in equation 2.2 spectral shaping can naturally be described in terms of angular frequency, since the "arrival time" of the spectral components is given by

$$t(\omega) = \frac{\partial \phi(\omega)}{\partial \omega} \tag{2.25}$$

This makes prism-based shapers preferable for some applications. The dispersed spectrum is collimated with a focusing element (a lens or a mirror) and sent through a Fourier mask which can be a liquid crystal modulator (LCM) or an acoustic-optical modulator. A LCM has an even number of pixels and each narrow spectral region (or "color") of the dispersed beam sees a different one. By applying individual voltage settings to the pixels one can independently change the properties of the individual colors. The focal length of the mirrors is exactly half of the prism – LCM distance. This means that in addition to spectral collimation the focusing element focuses each color in the LCM mask. After the LCM a second focusing mirror and prism transform the beam back. A variation of this setup uses a flat mirror right after the LCM. The beam is sent backwards on a vertically tilted trajectory and picked-off after the first prism. This configuration has the advantage that it doubles the effect of the LCM phase profile making large phase corrections easier to implement.

The setup described above is commonly named "a 4-f shaping system" because the total length is given by 4f, where f is the focal length of the mirror. In theory the setup should be dispersion free. This is close to being true for grating-based systems. In practice air propagation, the liquid crystal medium and the prisms (for prism-based systems) add a significant GD across the spectrum. An important factor in the 4f shaper is the size of the input beam. If the size is small then the temporal dispersion of the beam through the prisms is small, since the imparted chirp is roughly proportional to the insertion length of the beam in the prism, which, in turn, depends on the beam size. However the focus size at the LCM is inversely proportional to the input beam size, according to the formula:

$$d_o = \frac{4\lambda}{\pi} \times \frac{f}{d_1} \times M^2 \tag{2.26}$$

Here d_0 is the focus size, f is the focal length, d_1 is the input beam diameter and M^2 is the mode quality factor. So for prism-based shapers there is always a trade-off between how tightly the beam can be focused and how much additional chirp can be tolerated. The shaper setup accommodates beams of roughly 8 mm in diameter. This allows a focus size smaller than 100 μm. This number is equal with the pixel width and represents an upper limit for the acceptable focus dimension. The price paid is the addition of ~ 500 fs GD. The shaper is a 4 x 500 mm system and employs two F2 prisms and two silver-coated, 500 mm focal length mirrors. For the bacteriorhodopsin experiment, which has been performed at Stanford University, a setup containing an AOM, gratings with 600 lines/mm and 500 mm FL mirrors has been used.

The operating principles for LCMs and AOMs are detailed in the following paragraph. LCMs have an active aperture containing 128 - 640 pixels, each of them being controlled individually by applying a voltage. The electric field changes the alignment of the molecules and modifies the index of refraction and the optical path length, resulting in a phase shift. Amplitude shaping capabilities can be added by using crossed polarizers. One issue with pixel-based systems is the inter-pixel gap, which is usually between 2 μm and 10 μm. This dead space diffracts part of the beam resulting in energy losses, distortions of the spatial beam profile and unwanted amplitude modulation. Figure 2.12 shows this effect when a set of linear chirps is applied. The left panel shows the voltage applied for each pixel. A second order polynomial phase translates in a linear time delay between adjacent spectral components. The right panel shows the resulting change in the power of the output beam, which can be as big as 5%. All the lab results are corrected for this effect in the post-experimental analysis.

AOMs use a piezoelectric transducer which is driven by an oscillating electric signal. The transducer vibrates and induces an acoustic wave in the AOM crystal. The acoustic wave produces a refraction index grating which diffracts the shaped beam into the first diffraction order. This grating can modulate the intensity and phase of the incoming light. The main advantages of AOMs are the large aperture, the lack of discrete pixels and the low cost. One issue is the lower (~ 60%) efficiency. AOMs have been used initially for shaping the near infrared light generated by Ti: sapphire based amplifiers. In the last years AOMs started to be used in the visible and even in the UV spectral

domains. An important difference between the LCM and AOMs is the mask profile erase/update time, which is tens of milliseconds for LCMs and microseconds for AOMs. Because a stable mask profile in needed across the train of laser pulses, AOMs are suited for kHz applications while LCMs can be used for direct shaping of oscillator output.

The apparatus described here allows the creation of a practically infinite number of distinct laser pulses, each with its own phase and spectral profile. What is needed at this point is an efficient way to find in this "search space" the specific laser pulses which can induce the desired behavior in the molecules under study. For that sophisticated mathematical algorithms are used. An introduction to this subject is presented below.

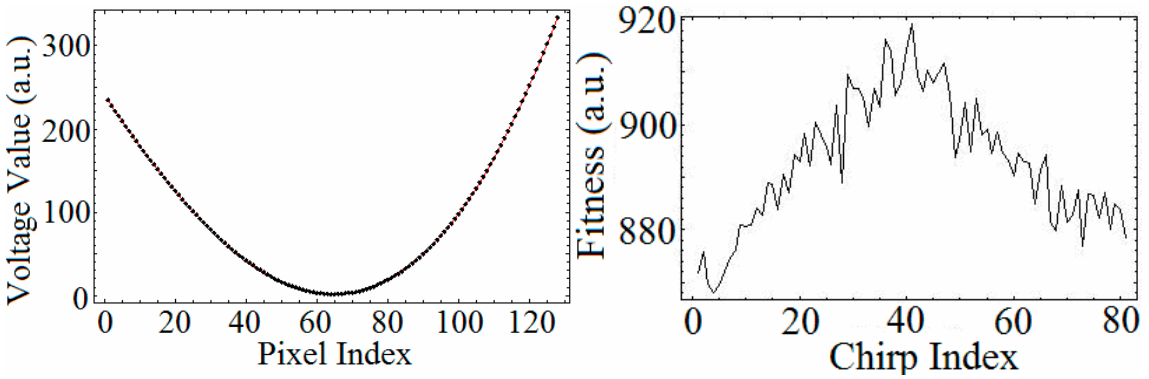

Figure 2.12. Left panel: the voltage values applied to the 128 pixels of the LCM mask. Right panel: undesired amplitude shaping of the laser pulse. Index 41 corresponds to no chirp (zero voltage) across the LCM mask. The fitness is proportional to the total power of the shaped pulse. A 4% intensity modulation is apparent. The chirp limits in the left panel correspond to typical limit values used in our experiments.

2.4 Optimization Techniques

The main purpose of coherent control experiments is to find the excitation pulse shape which is able to maximize the target chemical process. Given that a laser pulse is characterized by energy, spectrum, polarization, phase etc. the inevitable question is how the best performing pulse can be found in this huge search space. A few simplifications have to be made. The experiments presented in this work are performed for fixed pulse energy, spectrum and polarization. Only phase is allowed to change. In recent years

Gerber et al. [62, 63] have developed techniques to shape the polarization and performed polarization control experiments on atomic systems. Intensity is a knob which can easily be controlled. There are many chemical reactions which can be controlled through multi-photon processes where the light intensity is critical. We will detail this point when presenting the learning control experiment in bacteriorhodopsin. Another factor is the excitation spectrum. Most experiments are performed at resonance, where the pump spectrum is assumed to be optimal. In the LD690 experiment it is shown that tuning the excitation spectrum can significantly contribute to control [28]. Here it's necessary to distinguish between general spectral shaping and spectral tuning, which is defined as the shift of the full excitation spectrum in and out of resonance.

Assuming that the experiment is set to scan a certain pulse characteristic, the next question is how one can reliably find its optimal value. A brute force solution is to test all possible values but this is almost impossible. The efficient alternative is the use of search algorithms. It is beyond the purpose of this presentation to detail this large field of mathematics. In Chapter IV we employ one of the proven techniques, a heuristic approach called genetic algorithm (GA) search, which is described below [35, 36].

The GA is inspired from natural evolution and uses concepts like generation, mutation, selection and individual performance. A typical GA starts by creating a first generation, which has ~ 40 laser pulses, picked at random (see Figure 2.13). Each pulse has its own "genetic information" which is stored as a string of numbers corresponding to the voltage applied to the LCM pixels. Each set of voltage settings represents a phase configuration that produces a unique laser pulse. Each individual pulse is used to excite the molecular target and its performance is measured. The performance criterion could be for example the transmission of the probe light through the excited sample. This measure is converted to a number called individual fitness. The individuals of the generation are ordered according to the value of their fitness and a replication strategy is applied (see Figure 2.14). Typically the best 3-5 performers are kept unchanged (the elite) and the rest are modified by a series of genetic mutations. A crossover mutation for example would cut the genetic strings from two laser pulses in half and would switch them. A random mutation would randomly change a piece of a genetic string. The worst performers could be completely eliminated and replaced with fresh random candidates. After the mutations

have been implemented a new generation is tested, its individuals ordered and so on. The GA run is considered successful when a series of criteria are fulfilled. First the fitness of the best individual of each generation has to go up and then flatten, as a sign of saturation (further improvements are less and less likely). Second of all the mean fitness curve needs to move asymptotically towards the best individual fitness curve. Noise and the diversity of the individuals in the generation can prevent the perfect convergence of the two plots. Sample successful GAs can be seen in Figure 2.16 and Figure 4.8. GA settings like the size of each generation, the number of elites or the mutation techniques employed could have a high impact on the speed and quality of the search and are often empirically changed during the experiments. The GA code which is employed here has been developed in our lab [35, 36].

By using this technique there is no warranty that the absolutely best pulse will be found. However many experimental observations show that this method provides excellent results. By repeating the optimization experiments many times very similar solutions are obtained, even though the initial generations are randomly chosen. This means that it is unlikely that the algorithm gets stuck in a local minimum. Genetic algorithms have been used for a variety of molecular and atomic systems and a variety of fitness targets.

A simple case of a GA run is presented below. Each experiment performed in the lab has to start with the compression of the pump pulses, because the TL pulse serves as a benchmark for any measurements. For the purpose of compressing the pulse the beam is focused in a SHG BBO crystal and the intensity of the SH light is measured. From equation 2.14 it is apparent that the signal is proportional to the square of the intensity of the fundamental, which makes it very sensitive to the pump pulse duration. Two possible setups have been used in the lab: the first involves a simple geometry where the pump pulse is focused in the BBO crystal and a filter placed after the crystal separates the fundamental from the second harmonic, the latter being sent to a detector (upper panel of Figure 2.15). An alternative is to use a FROG setup, in which two copies of the pulse intersect in the crystal. The SHG signal is spatially separated from the fundamental and no filters are needed.

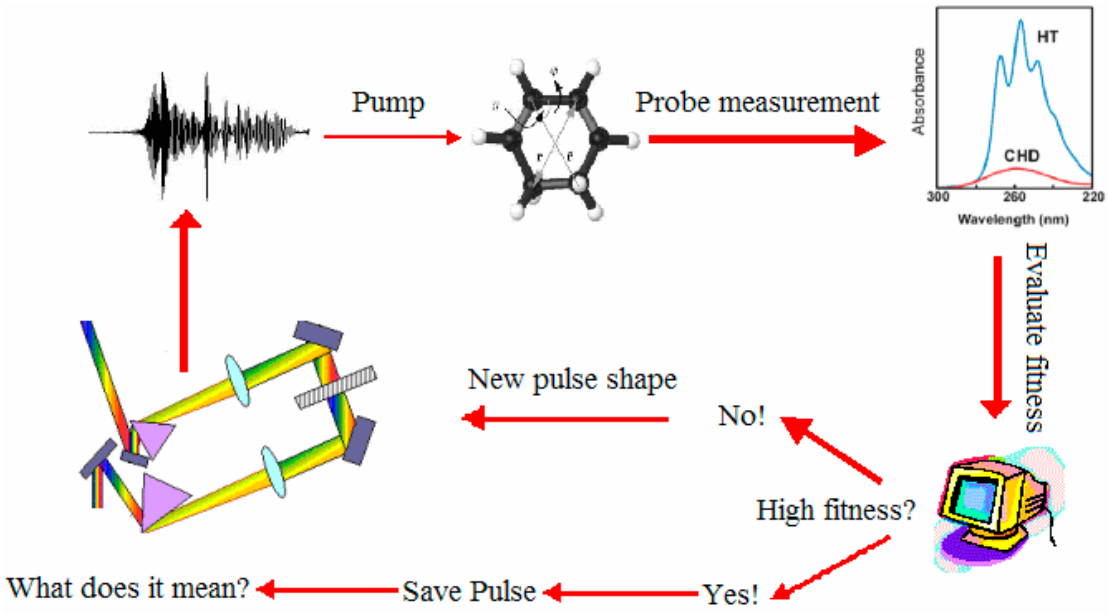

Figure 2.13. Schematic presentation of the coherent control apparatus. The arrows indicate the typical decision-making cycle during one GA loop. The spectra inset (upper right corner) shows the spectral signatures for two possible target states in cyclohexadiene. Similar distinct signatures exist in the LD690 and bR experiments presented in this thesis.

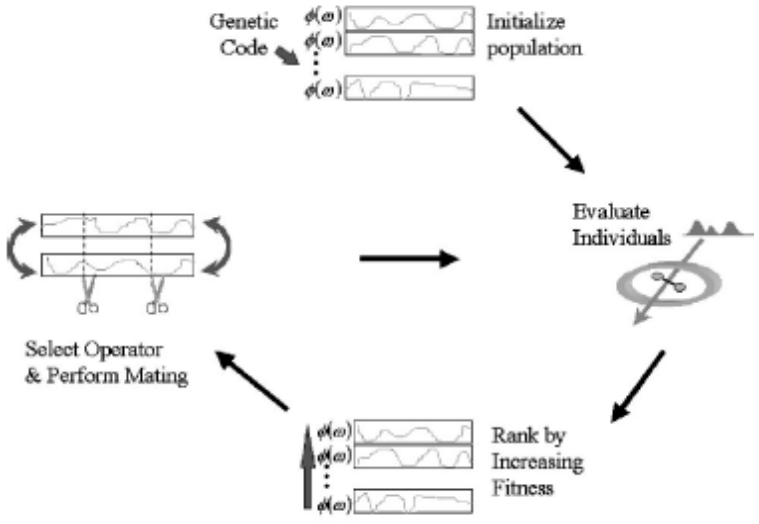

Figure 2.14. The genetic algorithm at work. Four stages can be discerned: initialization of the starting generation, evaluation of individuals, ranking of individuals according to performance and creation of a new generation.

This is important since for large bandwidth pulses the filters can distort the detected spectrum. Another advantage is that the FROG setup is designed for pulse measurement so the TL pulse can be characterized on the spot, after compression. The downside is that the two pump pulses need to be perfectly overlapped in time, but this can be done with good accuracy [5].

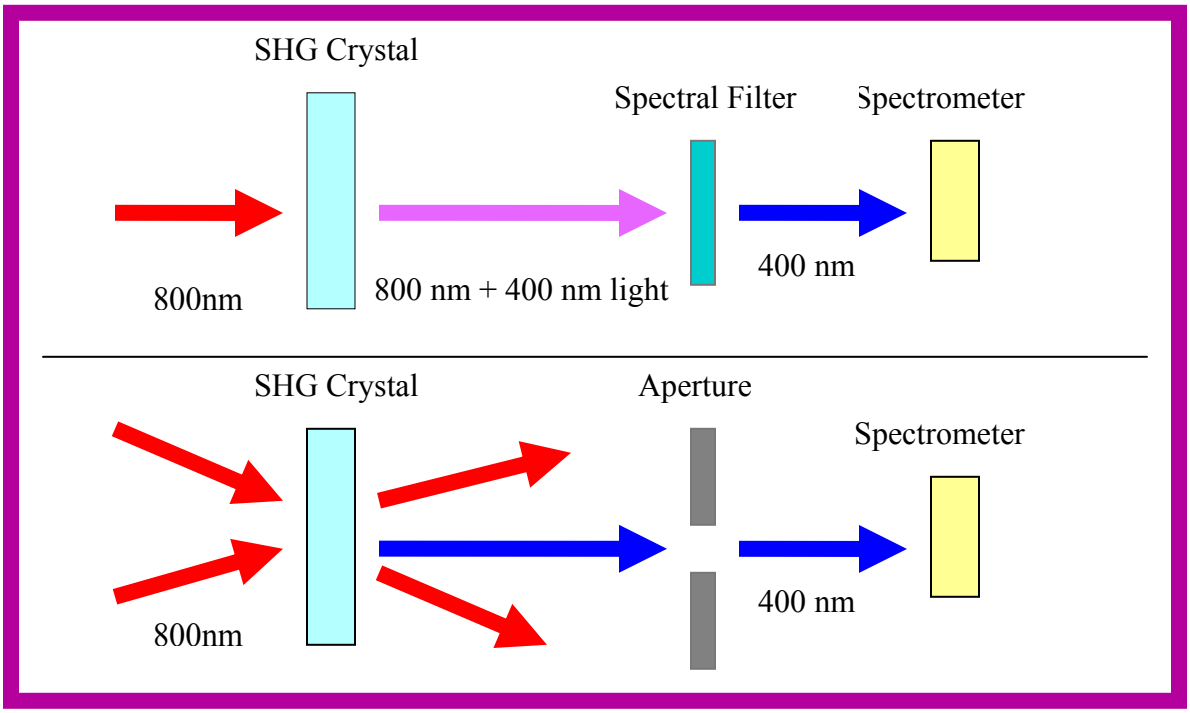

Figure 2.15. Two possible second-harmonic generation setups for pulse compression. Both present advantages and disadvantages. Upper panel: a simple SHG configuration. Bottom panel: a FROG setup.

Figure 2.16 shows a GA run which uses the FROG for compressing the output of a NOPA. The blue line represents the normalized fitness values for the best pulse shape of each generation, while the pink line represents the average fitness value of that generation. As described above, two quick measures can be used to quantify the success of the run. The first is how fast the blue line converges and we see that after 25 generations we reach the optimal shape. A comparison of the best pulse shapes for generations 25 to 50 shows little difference between them. The second measure is how close the average fitness converges to the best fitness. For a long run the GA is expected

to reach the conclusion that all pulses should have the same shape as the best of them in which case the average would be very close to the best fitness line. In practice noise prevents this, but it is obvious that the average line follows closely the best fitness line. In addition the GA by default introduces diversity in each generation of pulses, which means that always some pulses will be different from the optimal shape. In this example the GA managed to increase the efficiency of the SHG process by more than 100%.

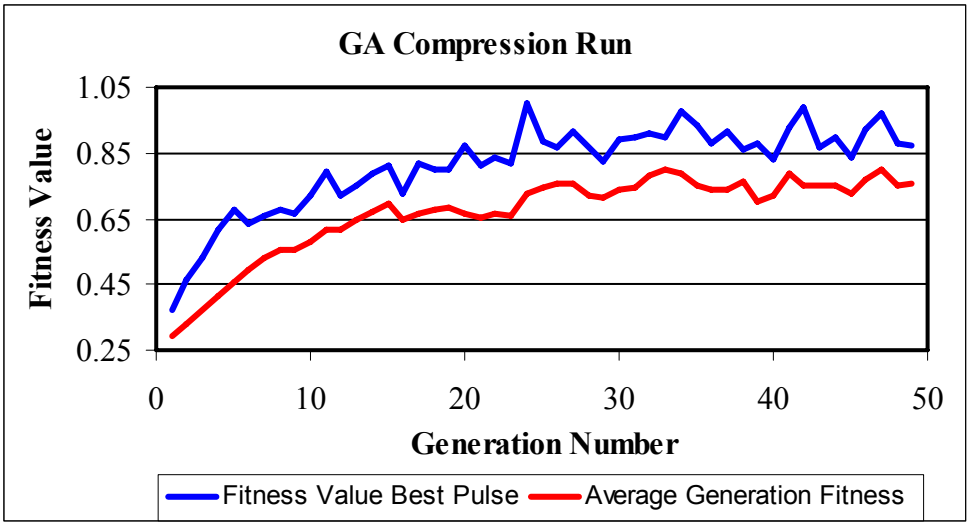

Figure 2.16. A typical compression GA, using as feedback a SHG FROG setup.

2.5 Pulse Compression

The 4f shaping setup alone is unable to compensate for the group delay of the NOPA pulses. Ideally the LCM should be used to modify the phase profile of an already perfectly compressed pulse. A prism-based compressor is used to flatten as much as possible the phase profile before the adaptive compression [64, 65].

The principle of a prism compressor is simple: the first prism disperses the incoming laser pulse and the second prism collimates the diverging colors. Figure 2.17 shows the colors of longer wavelength (further in the red) pass through a thicker section of the second prism compared to the shorter wavelength colors. On the other hand the air path between the two prisms is longer for blue wavelengths. The NOPA pulses usually have positive chirp (the red colors “arrive” before the blue colors).

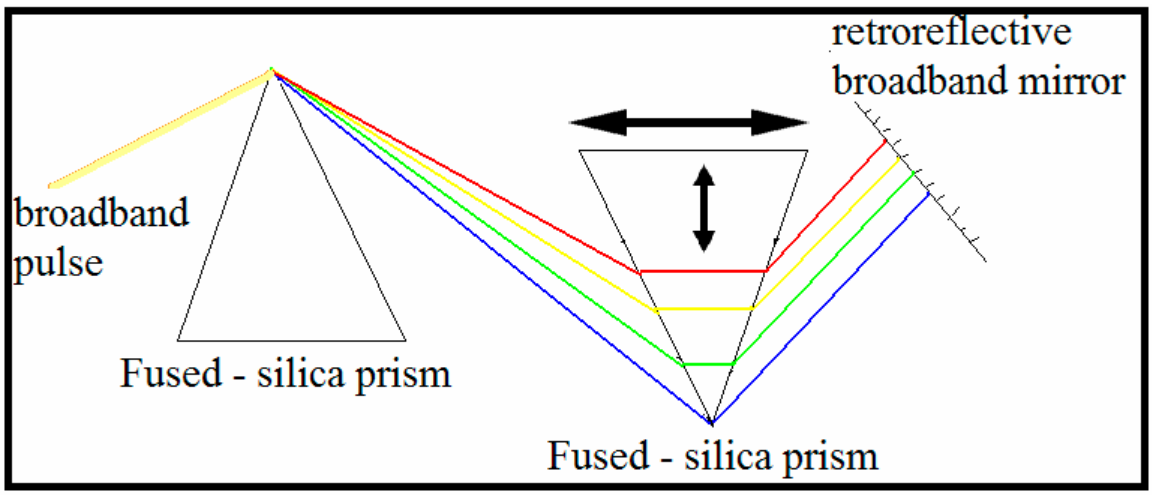

Figure 2.17. A schematic presentation of a prism-based double-pass compressor. The first prism disperses the spectrum. The second prism can be translated along the double-arrowed directions, tuning the group delay across the pulse.

The second prism adds delay to the redder colors such that, when the compressor is well aligned, all the wavelengths of the output beam arrive at the same time. Three parameters affect the phase correction profile of the compressor: the angle of the prisms, the inter-prism distance and the insertion depth in the second prism. The first two factors determine how spread out the spectrum will be at the second prism. The last parameter influences the actual optical path difference seen by the different spectral components. In practice the prisms are set at the minimum deviation angle. Then the inter-prism distance is varied and for each intermediate position the pulse duration is measured until a minimum is found. For that position the insertion of the second prism is changed until an even better minimum is observed. Occasionally this procedure needs to be iterated a few times before a good compression is reached. Alternatively, if the distance between prisms is small the positive chirp induced by the different air path lengths dominates compared to the negative chirp induced by the glass of the second prism and the "compressor" acts like a stretcher.

As mentioned in the section describing the 4f shaping system, prisms are good at reducing the second order phase for medium broadband pulses. Higher orders are more difficult to correct. That's why a compressor configuration is considered good if the pulse is compressed to within 15% of its minimum bandwidth-limited duration. For this

compressor configuration the compression optimization algorithm is run. In this way the prism compressor eliminates a large part of the compressing "burden" of the 4f system.

A plot of the group delay (or, equivalently, the arrival time) versus the pulse spectrum is presented in Figure 2.18 for a series of compressor configurations.

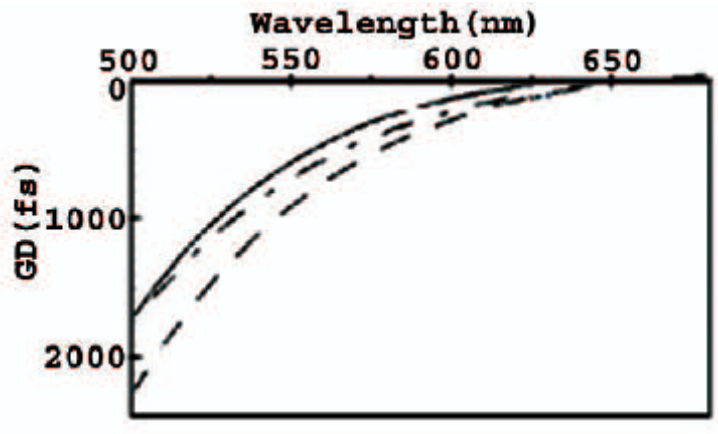

Figure 2.18. The group delay (500 nm – 650 nm spectrum) for three compressor configurations. l is the inter-prism distance and i is the insertion depth. Settings: l = 1.7 m & i = 2 cm (dashed line), l = 1.7 m & I = 2.5 cm (continuous line) and l = 1.3 m & I = 1.5 cm (dashed-dotted line).

The plots show that the GD of the different optical paths is not linear while the chirp of uncompressed NOPA pulses is mostly linear. However for a pulse of ~ 50 nm bandwidth the prisms compressor can offer reasonable chirp compensation.

2.6 Pulse Characterization

Very important for any coherent control experiment is the capability of accurately measuring the laser pulse shapes. Many measuring devices exist today: SPIDER, FROG, GRENOUILLE etc. [66]. The principle lying at the base of these designs is simple: in order to measure an ultrashort pulse it is necessary to have another pulse at least as short and the most convenient to use is the pulse itself. This is why many methods involve splitting the pulse in two replicas by using a beamsplitter and then recombining them in a

non-linear medium. Each type of device presents certain advantages and disadvantages. The experiments reported below use a SHG FROG, which is described in Figure 2.19.

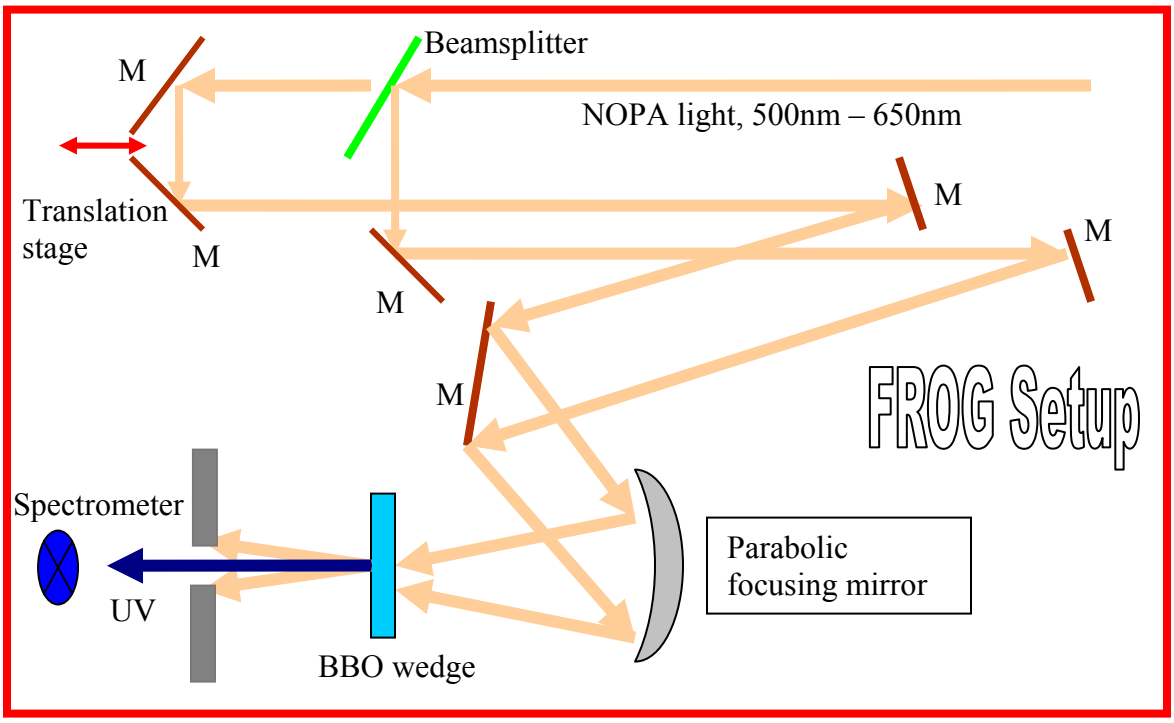

Figure 2.19. A typical SHG FROG setup. M = metallic, low dispersion mirror. The spectrometer is typically an Ocean Optics SD2000 or HR4000 unit, fiber coupled.

The laser pulse is split in two identical copies with a two microns thick pellicle beamsplitter, AR coated for visible light. The transmitted beam is retro-reflected with two mirrors placed on a delay stage, which is computer-controlled and has a step resolution of 500 nm (or $2 \times 0.5mm \times \frac{3.3\,fs}{1mm} = 3.3\,fs$ temporal resolution). All mirrors are aluminum-coated for minimum dispersion. The total air path in the FROG device has been matched with the total air path for the beam up to the experimental cell and a fused silica slide of the same thickness as the cell wall is inserted in the path in order to precisely reproduce the real pulse duration in the molecular sample. The nonlinear crystal is a BBO wedge (EKSMA, Lithuania) with thickness varying between 5 µm and 20 µm and is glued to the front face of a 2 mm thick UVFS slide. The BBO crystal has to be very thin since the maximum SH bandwidth is inversely proportional to the BBO length (see Equation 2.14).

This phenomenon is called spectral filtering and can be acute for broadband pulses. A plot of the SH bandwidth for crystal thicknesses of 5 μm (red curve), 10 μm (blue curve) and 20 μm (green curve) is presented in Figure 2.20.

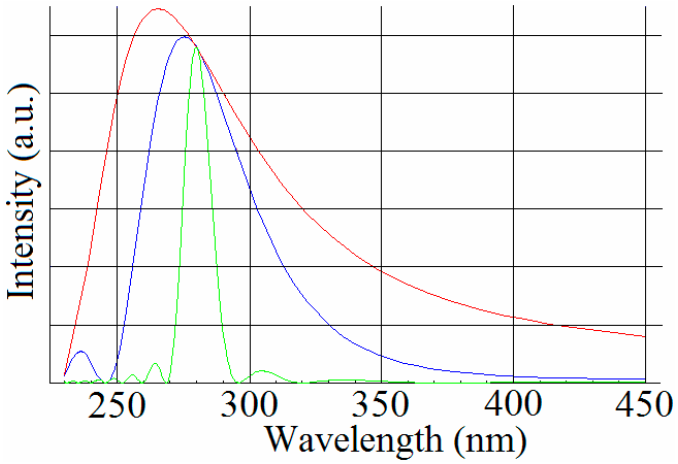

Figure 2.20. The phase-matching bandwidth in BBO crystals of various lengths. Red curve: 5 microns; blue curve: 10 microns; green curve: 20 microns. The bandwidth is very sensitive to the thickness parameter.

A sample result for compressing the NOPA output according to the above prescription is shown Figure 2.21. The right-hand panel shows that the phase profile (the dashed line) is flat over almost all the pulse spectrum (continuous line). The pulse duration is about 20 fs FWHM, as seen in the left-hand panel. The technology described in detail above (pulse generation in the NOPA, then compression, shaping and measurement) is used for all the experiments described in this thesis.

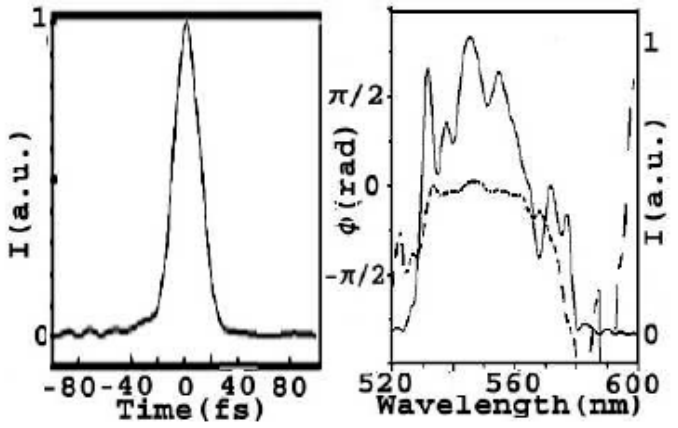

Figure 2.21. The intensity profile of the optimized pulse (left panel) and the retrieved phase (dashed line) and spectrum (solid line) profiles (right panel).

Chapter III

Control of Vibrational Coherences in LD690

3.1. Introduction to Coherent Control

The field of coherent control is a relatively young domain of physical chemistry. The advent of the ultrafast lasers allowed scientists to observe atomic and molecular motion on a very fast time scale and, naturally, the idea of controlling the dynamics arrived [2, 10, 15, 21, 24]. A very important point was the paper published in 1992 by R. S. Judson and H. Rabitz, titled "Teaching Lasers to Control Molecules" [10]. This paper outlines the basic principles of laser control and compares the approach with "an analog computer" which solves exactly Schrödinger's equation. As it is well known, this equation has the form:

$$H(t)\left|\psi(t)\right\rangle = i\hbar\frac{\partial}{\partial t}\left|\psi(t)\right\rangle \tag{3.1}$$

The Hamiltonian of the quantum system can be written as

$$H(t) = T + W(r,t) \tag{3.2}$$

T is the kinetic energy and W(r, t) is the potential energy of the system. A laser pulse interacts with atoms and molecules through its electro-magnetic field, which contributes to W(r, t). If we write the total energy of the interaction between a distribution of charges and an electric potential φ we get

$$W = \sum_i q_i \times \varphi(r_i) \tag{3.3}$$

After expanding the potential in Taylor series the equation becomes

$$W = q\varphi - \vec{\mu} \times \vec{E} - \frac{1}{3}\Theta \times \nabla \vec{E} \ldots \tag{3.3}$$

As seen in Equation 3.1 the Hamiltonian drives the dynamics of the system, and W(r, t) depends on the electric field so laser pulses can be used to steer the quantum evolution. Most times we deal with neutral atoms and molecules so the first term of the series is null and the strongest interaction is given by the dipole term.

As explained in the experimental section, optimized coherent control is achieved by searching through the space of possible laser pulses and finding the one which maximizes the control target. This is different from the traditional way in which physics problems are solved. Usually scientists analyze theoretically a certain system and then propose an optimal tool (i.e. a laser pulse) for accomplishing control. This approach could work for very simple systems like atoms or diatomic molecules but when the number of atoms increases it becomes much harder to implement. Of big interest for the scientific community is the control of molecules in liquid solution, which adds another element of complexity, the interaction with the environment. In this situation it is impossible to theoretically find the Hamiltonian and solve Schrodinger's equation. Coherent control techniques leave the job of finding the optimum Hamiltonian to nature. At the end of a GA search the best laser pulse represents the optimal solution to the problem under the given experimental conditions. All we had to do was to search the space of possible solutions and monitor the fitness function.

However the most important part of the work starts here. The optimal laser pulse is valuable because it provides a "black-box" solution for our given optimization problem. But this pulse should be analyzed to discover the underlying control mechanisms. A FROG measurement will reveal the phase profile of the pulse, which, correlated with the absorption spectrum tell what time ordering of the spectral components is most efficient. By tuning the pump spectrum or the phase profile we can see how non-optimal pulses interact with the molecule and isolate the specifics of the optimal mechanism. This approach relies heavily on a priori knowledge about the

molecular system under study. Another systematic approach used in our group is principal component analysis (PCA) [36]. A couple of studies addressed the issue of the complexity of the GA solutions. Hornung et al. show that in some cases a small number of pulse features could be responsible for most of the fitness [67].

3.2. Overview of LD690 Chemistry

A large number of systems in both gas and condensed phases have been investigated in the last decades [1, 8, 14, 20, 23, 24, 30-32, 68-73]. Among these, dye molecules in solution have been studied extensively because they have important characteristic advantages [14, 23, 24, 31, 32, 68, 70, 71]. Most dyes exhibit strong absorption in the visible part of the electromagnetic spectrum, where reliable ultrafast laser sources are readily available; they are photostable over a large number of excitation de-excitation cycles; the ground and excited-state dynamics and structure are in general well characterized; and their size and structures make them good prototypes for more complex biological chromophores. For the most part, coherent control studies on dyes have been concerned with manipulation of the ground and excited-state population and linear chirp has emerged as the single most important control parameter [14, 24, 31, 68, 70]. Pioneering work in this field was done by Shank and co-workers, who studied the LD690 (oxazine 4 or 3-ethylamino-7-ethylimino-2, 8-dimethylphenoxazin-5-ium perchlorate) dye molecule among other systems [22, 37, 74-76]. These experiments demonstrated that high-power positively chirped excitation enhances the total fluorescence signal (i.e., the excited-state population), while high-power negatively chirped excitation suppresses fluorescence [74, 77]. An intra-pulse pump-dump model was invoked to explain this result (Figure 3.1).

In the case of negative chirp, excitation is initiated by the blue edge of the spectrum. The instantaneous frequency of the remainder of the pulse follows the shift of the Frank – Condon overlap caused by the motion of the wave packet to the right of the inner turning point (see Figure 3.1). As a consequence, population is resonantly dumped back to the ground state by stimulated emission. In contrast, positive chirp pumps population to the upper level, beginning in the red and continuing to pump higher into the

excited state as the pulse tunes blue, rather than dumping population back to the ground state. Coherent ground and excited-state dynamics may play an important role in many chemical reactions [11, 77-81]. Selective excitation of the vibrational modes of a molecule can lead to bond breaking and/or steer the system toward a desired target state.

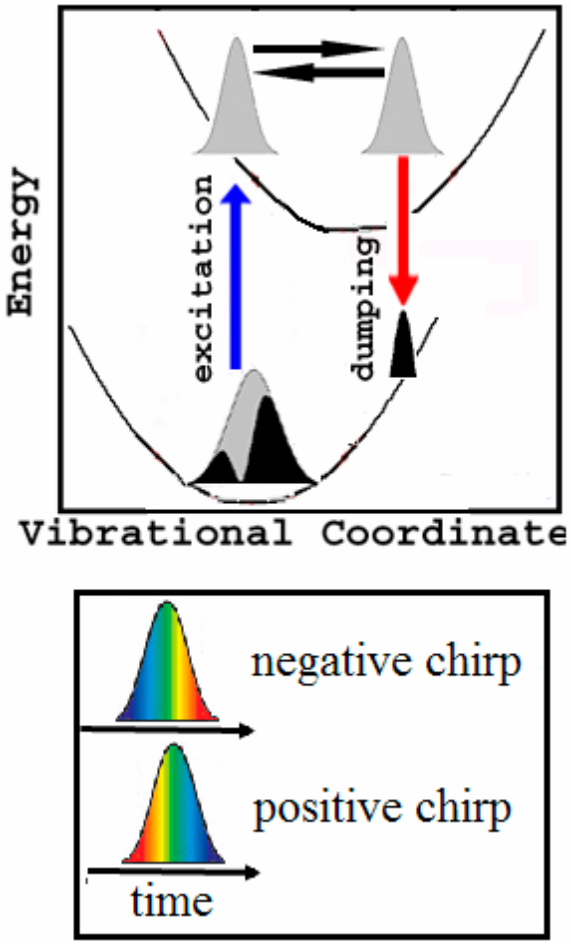

Figure 3.1. Schematic presentation of a pump-dump mechanism. This type of model is frequently used to explain molecular dynamics in simple two-level molecular systems (see text for details). The bottom figure depicts the time ordering of spectral components for negative and positive chirped pulses.

Optical pulse shaping can be extended from the control of population in electronic states to the control of vibrational coherences through Raman-type processes [22, 37, 78, 82]. In many cases it is not trivial to separate the ground and excited-state contributions

to the coherence signal. A number of experimental and theoretical papers have dealt with this problem [83-88]. The amplitude, frequency, phase, and damping times of the coherent oscillations can be used to deduce the ground or excited-state nature of the vibrational wave packet(s) generated in the excitation process. Chirped pulse excitation was found to have a significant impact on the amplitude of the wave packet oscillations [22, 37]. Negatively chirped pulses stimulate ground state coherences, while transform-limited and positively chirped pulses enhance the excited-state component [22, 37, 75, 76]. In this work we explore the influence of both spectral shaping and phase shaping of the excitation pulse on the observation of vibrational coherences for the LD690 dye molecule. These results are compared with the results of prior experimental investigations. LD690 is a convenient molecule as it has a rigid structure and exhibits a single dominant Franck-Condon active mode at about 586 cm^{-1}, assigned to a ring breathing motion [75].

In the present study we find that changing the pump spectrum allows selective excitation of ground or excited-state coherences. For a given pump spectrum, phase shaping can further improve control of the vibrational coherences. Negative chirp enhances ground-state coherences in many cases [37, 78], but when coupled with blue detuning of the pump spectrum away from the 0-0 region of the electronic transition, negative chirp suppresses the observation of coherent oscillations in the transient absorption signal. In contrast, positive chirp for the same pump spectrum increases the intensity of the vibrations. This effect is dominated by the excited-state contribution to the signal.

3.3 Experimental Setup

The NOPA pulses used in this study have 150-350 nJ energy, 50-70 nm spectral bandwidth, and a peak wavelength tunable between 570 and 630 nm. The NOPA was tuned to produce four different pump spectra. The first pump spectrum overlaps with the peak and the red edge of the LD690 absorption profile. The second pump spectrum extends over most of the absorption spectrum, with the peak intensity tuned to the blue of

the absorption peak. To better understand the effects of the spectral shaping of the pump pulse on the vibrational dynamics, two additional pump spectra were also employed, one truncated at 610 nm and the other truncated at 600 nm. These blue-tuned pulses enhance the excitation of the excited vibrational levels of the S1 electronic state. These four pulse spectra are referred to as red-tuned (RT), broadband (BB), and blue-tuned (BT1 and BT2, respectively) – see Figure 3.2.

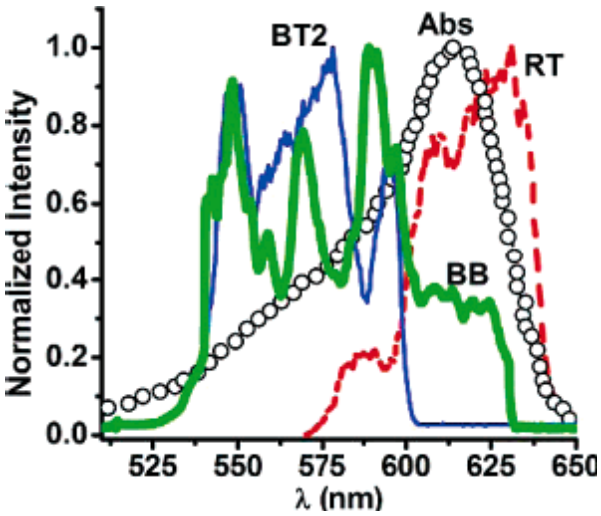

Figure 3.2. LD690 absorption spectrum (black open circles) and three of the pump spectra: red-tuned (RT, red dashed line), broadband (BB, green thick solid line), and the blue-tuned spectrum cut at 600 nm (BT2, blue thin solid line). BT1 is similar to BT2 but truncated at 610 nm rather than 600 nm.

Figure 3.2 shows the static absorption spectrum of LD690 in ethanol and three of the pump-pulse spectra. The LCM used for pulse compression was also used to produce pulses having predefined linearly chirped phase profiles for the experiments described below. For the red-tuned pulse shown seven sets of phase settings were applied to the LCM, corresponding to the TL pulse (33 fs) and three pairs of positively and negatively chirped pulses, with $\Phi''(\nu) = \pm 20\,000, \pm 40\,000$, and $\pm 80\,000$ fs^2 respectively. We will refer to these pulses as TL, PC1, PC2, PC3, and NC1, NC2, NC3. With the broadband excitation pulse, only three phase profiles were utilized, the transform limit and one positively and one negatively chirped phase profile. Because the spectrum is broader, the TL pulse was about 20% shorter than the TL pulse with the red-tuned spectrum (26 fs vs.

33 fs FWHM), although the structure in the spectrum will also contribute to intensity in the wings of the pulse. The chirped pulses (designated PC4 and NC4) had durations of about 40 fs and chirp rates of $\Phi''(\nu) = \pm 32\,000$ fs^2, intermediate between the chirp rates for the PC1/NC1 and PC2/NC2 pulses with the red-tuned spectrum. Finally, the pump spectra truncated at 610 and 600 nm (BT1 and BT2) were used in tandem with five phase settings, TL, two positively chirped, and two negatively chirped. The corresponding chirp rates are $\Phi''(\nu) = \pm 10\,000$ fs^2 (PC0/NC0) and $\Phi''(\nu) = \pm 40\,000$ fs^2 (PC2/NC2), respectively.

For the experiments described here, both the temporal and spectral structure of the excitation pulses is of particular concern. The red-tuned excitation pulse shown in Figure 3.2 exhibits a relatively smooth spectral profile. Thus, the temporal profile of the TL pulse is relatively smooth as well. However, the detuned pulses exhibit some spectral modulations, which, combined with the particular phase profiles applied to the shaper, could lead to peculiar temporal profiles. To analyze this possibility in greater detail, the FROG traces and retrieved temporal profiles for the broadband TL and NC cases are shown in Figure 3.3.

For the transform-limited pulse, each of the satellite pulses has total energy < 3% that of the main pulse. To a large extent, these satellites are due to incomplete compensation of the phase by the compression algorithm since a Fourier transform of the spectrum (not shown) exhibits minimal satellite structure. This analysis supports the hypothesis that, at least for the TL case, the changes reported in this work are due to the tuning of the pump spectrum and not to the spectral modulations observed in Figure 3.2. For the NC pulse on the other hand, the combination of spectral and phase modulations results in a more complicated temporal structure. There is one dominant lobe followed 30 fs later by a satellite pulse whose total energy is about 20% of the main lobe. Due to the linear chirp imparted on the spectral profile, the main pulse is shifted compared to the post pulse, so the time ordering of colors, essential for the pump-dump mechanism, is maintained. In conclusion, the spectral modulations seen in the broadband spectrum do result in some temporal structure for the linearly chirped pulses, but the extent of this temporal structure does not undermine the pump-dump model as the chief excitation mechanism.

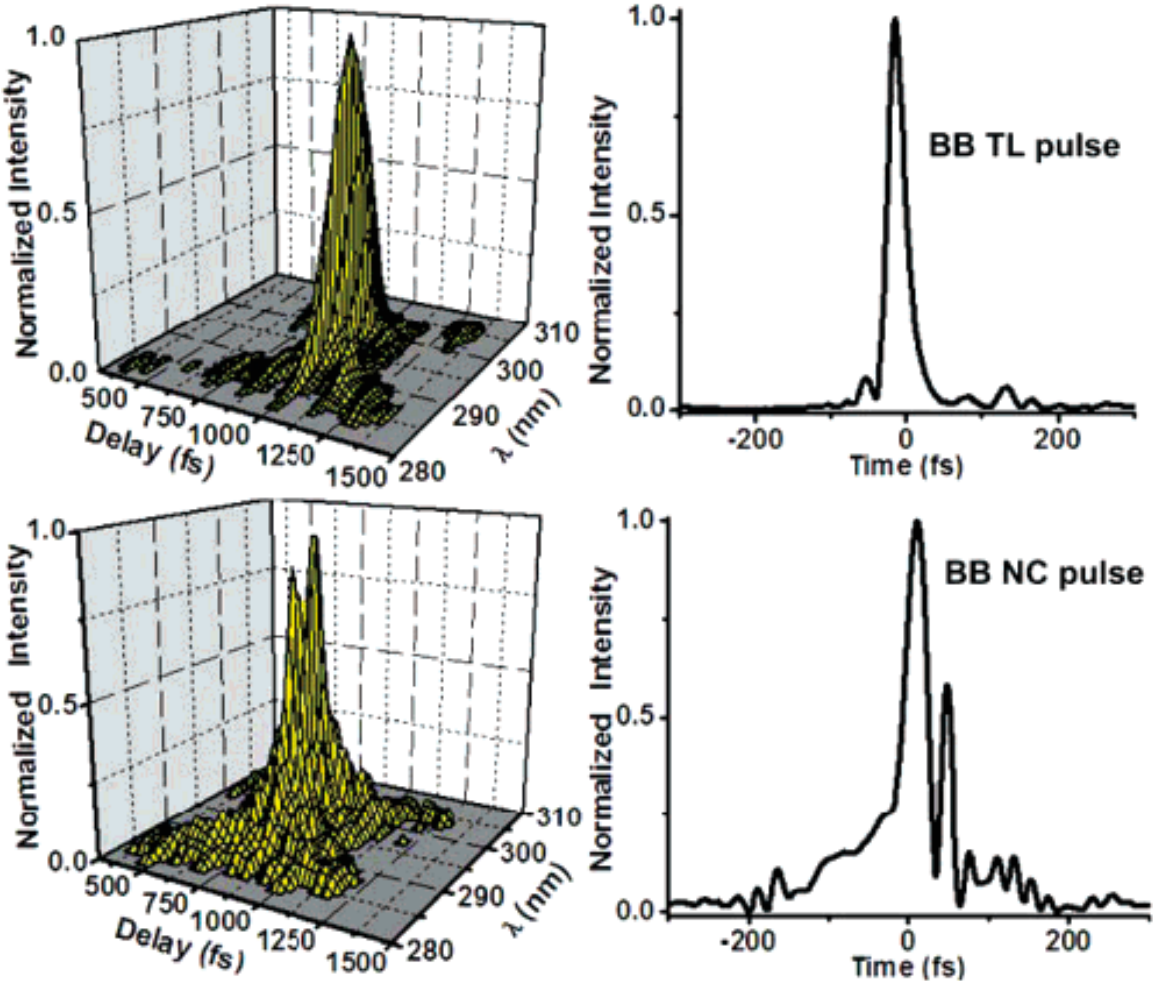

Figure 3.3. Experimental FROG traces (left-side column) and the retrieved time profiles (right-side column) of the excitation pulses for the broadband TL and NC cases.

For transient absorption measurements, a broad white light probe pulse is generated by focusing a fraction of the 790 nm fundamental beam of the laser into a piece of sapphire. The relative timing of the white light (WL) probe with respect to the pump pulses is controlled by using a computer-controlled translation stage (Newport, 25 cm range, 0.1 μm step size). The white light probe produced in sapphire exhibits a temporal chirp across its spectrum and the typical FWHM of the pump-probe correlation signal over a narrow probe wavelength range was ~ 40 fs. The resolution with which the pump-probe kinetic traces are sampled is in practice even better than 40 fs. This figure is consistent with previous measurements reported in literature. In a detailed analysis of the

time resolution of pump-probe spectroscopy experiments, Kovalenko et al. [52] showed that even for 50 fs pump pulses and WL chirps of 300-400 fs, the temporal features can be characterized with a resolution better than 10 fs. In the present experiment, the TL pulses are shorter (20-30 fs) and the chirped pump pulses (red-tuned PC2/NC2 and PC3/NC3) do not exceed 50-70 fs.

The sample, a 1 mM solution of LD690 (Exciton) in ethanol (99%, Aldrich), is flowed through a quartz cell with 100 μm path length to refresh the sample volume between consecutive laser shots. A mirror with a 250 mm focal length focuses both the pump and the probe on the sample. The upper limit of the pump intensity at the focus is 10^{11} W/cm^2. The absorbance of the sample is 1.1 OD and the maximum value of the transient absorption signal is 0.65 OD when pumping with the resonant, red-tuned excitation spectrum. This signal is a combination of stimulated emission and ground-state bleach, from which it can be inferred that ~ 30% of the ground-state population is excited. The probe light is collected after the sample and coupled by an optical fiber into the Master channel of a SD2000 Ocean Optics spectrometer (0.3 nm resolution), while the reference is picked-off before the sample and coupled into the Slave channel. The signal was calculated as $Log\frac{I_{probe}(t)}{I_{reference}(t)}$ and typically averaged over 1000 shots.

3.4 Experimental Results

A typical chirp corrected pump-probe kinetic trace is shown in the left-hand panel of Figure 3.4. These data illustrate the evolution of the transient absorption signal over the first 2 ps of the scan. A strong oscillatory component is evident in the region between 580 and 650 nm, arising from the coherent motion of the wave packet created by the laser excitation. The early time oscillatory features (before zero time delay and within the width of the pump pulse) are due to pump-probe coherent effects and are not investigated further in this work [52]. The right hand panel of Figure 3.4 shows the static absorption spectrum, and the fluorescence spectrum of LD690, along with a lineout of the transient

difference spectrum averaged over the first 2 ps after excitation. The peaks of the three spectral profiles are at 615, 637, and 620 nm, respectively. Three separate regions can be distinguished in the transient difference spectrum. The absorption change in the region between 450 and 550 nm has positive values and is dominated by the excited-state absorption. The region between 550 and 650 nm has a negative signal and is due to a combination of ground-state bleach and excited-state stimulated emission. The peak transmission in the transient difference spectrum is shifted by about 5 nm to the red compared with the static absorption spectrum due to the Stokes shift of the stimulated emission and the positive contribution of the excited-state absorption on the blue side of the spectrum. The far-red side of the spectrum is dominated by the stimulated emission from the excited state.

Analysis of the pump-probe scans consists of a multistep procedure. The signal-to-noise ratio is improved by averaging the data over three adjacent spectrometer channels (3 × 0.3 nm bandwidth). The electronic population component of the signal is extracted by fitting the data to a model consisting of biexponential decay to a plateau. Figure 3.5 shows the oscillatory component obtained at the probe wavelength of 610 nm, for red-tuned and broadband TL excitation, after the execution of the steps described above.

This oscillatory component was analyzed by using a fast Fourier transform algorithm and by using a Levenberg-Marquardt nonlinear fitting algorithm to fit the data to a sum of decaying cosine functions. The FFT analysis is used to extract quantitative information about the intensity and frequency of the oscillations. However, the time resolution of the FFT technique is inherently limited by the delay span of the pump-probe kinetic traces and this limits the spectral resolution when measuring the oscillation frequency. Because the analysis of the oscillation frequency occupies a central point in the ensuing discussion, it is important to provide a mathematically independent technique for its measurement. This is the intent of the nonlinear fitting algorithm, which is used for the determination of the oscillation frequency and dephasing times. The two methods give consistent results, as expected, and both analyses will be discussed below.

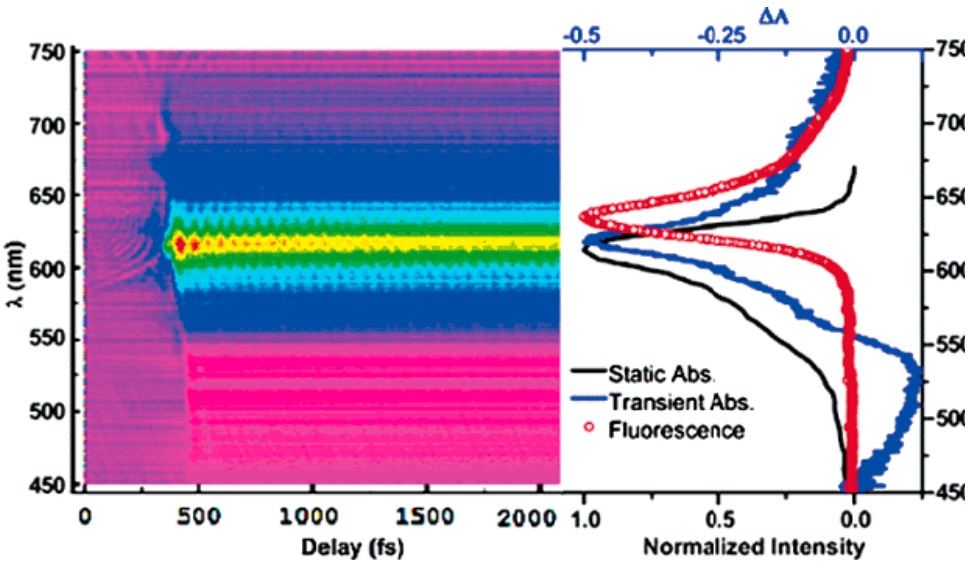

Figure 3.4. Left panel: typical two-dimensional plot of the transient kinetics. Right panel: the absorption and fluorescence spectra. Note the different scales for the transient absorption spectrum. The transient absorption signal ΔA is defined as $Log\frac{I_{probe}(t_0)}{I_{reference}(t_0)} - Log\frac{I_{probe}(t)}{I_{reference}(t)}$. The time t_0 represents the initial delay between the probe and the pump pulses with the probe pulse preceding the pump pulse. The molar absorptivity for LD690 in ethanol is 10.9×10^4 L/(mol × cm) at 615 nm, which gives an absorbance $A = 1.1$.

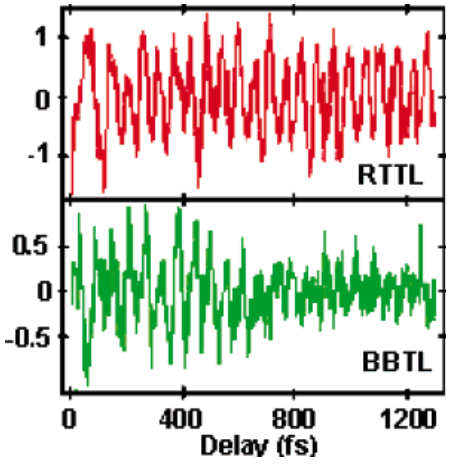

Figure 3.5. Pump-probe kinetic traces collected at 610 nm, produced by excitation with the red-tuned (RT) and broadband (BB) TL pulses.

3.4.1 FFT Analysis of the Oscillatory Component

The oscillatory component extracted from the data is analyzed using a fast Fourier transform (FFT) algorithm (Mathematica 5.2 Wolfram Research). The resulting FFT spectra are normalized by the average electronic population signal for each probe wavelength. The shortest experimental scans are about 1.7 ps long and the longest about 13 ps. These full traces are subject to the FFT to determine the vibrational frequencies. However, the dephasing times depend on the probe wavelength and the amplitudes obtained from Fourier transforms over long scans will be distorted by the damping of the oscillation. Thus, the FFT is confined to the first 256 points (850 fs) for determination of the amplitude profiles. Figure 3.6 shows a plot of the frequency of the dominant ring breathing mode as a function of the probe wavelength for the BB and RT pump spectra. From this plot, it is clear that the observed vibrational frequency is consistently higher for the red tuned pump than for the broadband pump. Some longer scans were taken for RT TL (i.e., red-tuned transform limited, in general pulses are designated by the pump spectrum phase profile as in Table 3.1) and BB PC excitation conditions (the solid blue shapes in Figure 3.6), confirming the results obtained for the shorter scans.

	$\Phi''(\nu)$ (fs^2)				
Spectrum	±10 000 PC0/NC0	±20 000 PC1/NC1	±32 000 PC4/NC4	±40 000 PC2/NC2	±80 000 PC3/NC3
Red-tuned (RT)		+		+	+
Broadband (BB)			+		
Blue-tuned 1 (BT1)	+			+	
Blue-tuned 2 (BT2)	+			+	

Table 3.1. Spectra and chirp rates used in the LD690 experiment.

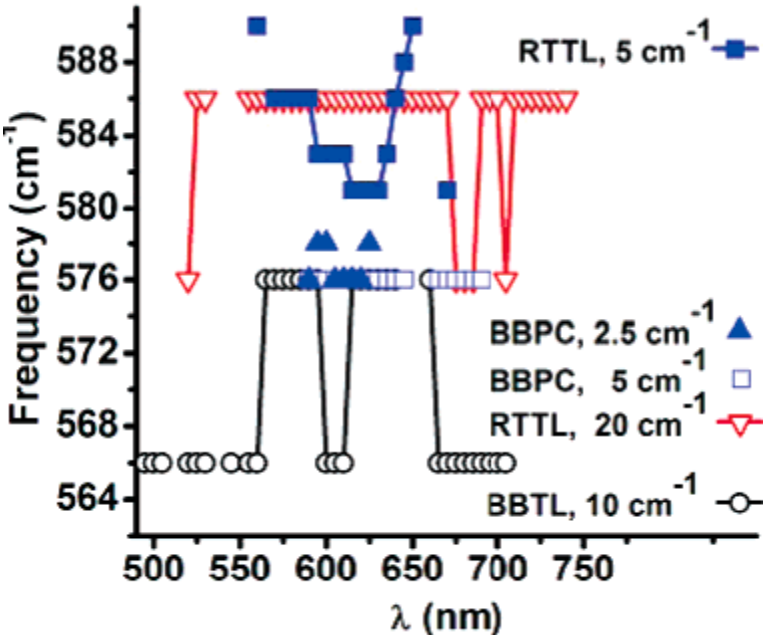

Figure 3.6. Frequency of the dominant mode vs. the probe wavelength, retrieved with the FFT procedure. The FFT point spacing is 20 or 5 cm^{-1} for RT TL data sets, 10 cm^{-1} for the BB TL data set, and 5 or 2.5 cm^{-1} for the BB PC data sets. The peak frequency can be determined with somewhat better resolution. For the two blue-tuned spectra (BT1, BT2, not shown), the oscillation frequency is 576 cm^{-1} in all cases and the FFT resolution is 5 cm^{-1}.

3.4.2 Analysis of Vibrational Frequencies and Dephasing

In addition to the FFT analysis, a Levenberg-Marquardt nonlinear fitting algorithm (Mathematica 5.2, Wolfram Research) was used to extract the damping times, the vibrational frequencies, and the corresponding standard errors from the data (see Figure 3.7).

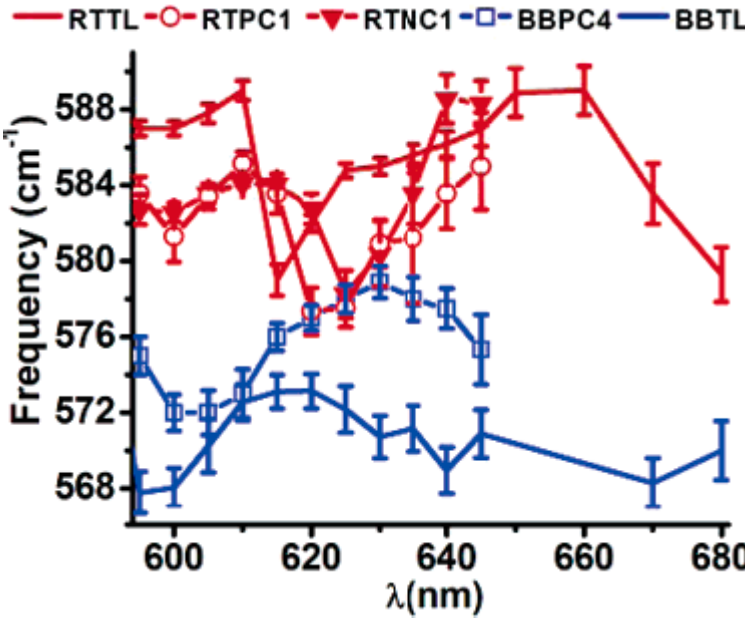

Figure 3.7. Frequency of the dominant vibrational mode vs. the probe wavelength for the red-tuned (red lines) and broadband (blue lines) cases. Pulse phases as indicated: TL, no symbol; PC1, circles; NC1, triangles; PC4, squares.

In this analysis, the kinetic traces are fitted with the sum of two exponentially decaying cosine functions. The fitting procedure always pulls out one frequency corresponding to the ring-breathing mode. The other oscillatory component typically has small amplitude and a much faster damping constant, making a significant contribution only at time delays smaller than 300 fs and representing at most 25% of the amplitude. Its frequency fluctuates with the probe wavelength and does not correspond to a value expected from the Raman spectrum of LD690. As in the case of the FFT study, the kinetic traces were corrected by subtracting the contribution to the signal arising from

population dynamics before analysis. Nevertheless, the correction is not perfect, and for some kinetic traces, it produces spurious features at very early time delays. Investigation of the fitting results shows that the minor frequency component of the fit function is necessary to compensate for these artifacts.

A comparison of Figures 3.6 and 3.7 shows that the two methods produce frequency plots having similar features. In both graphs, there is a clear frequency shift between the broadband and red tuned excitation. For the broadband TL excitation pulse, the frequency shift is largest at the shortest and longest wavelengths. The frequency of the dominant vibrational mode observed following excitation with the red-tuned pump pulse is about 580-588 cm^{-1} on average. In contrast, the frequency of the dominant vibrational mode is about 10-15 cm^{-1} lower following excitation with the broadband pump pulse centered in the blue. For the broadband pump pulse, negative chirp suppresses the observation of coherent oscillations and the nonlinear fit procedure cannot retrieve reliable values. In the case of red-tuned excitation with either TL or PC1 phase profiles, the dephasing of the coherent oscillations is very slow compared with the length of the analyzed traces for probe wavelengths around 615 nm. To determine realistic limits for the dephasing times, the retrieved fit function was used as a starting point and the time constant for the decay was varied until a significant deviation of the fit from the experimental trace was apparent. This deviation corresponds to an increase of about 3% in the value of χ^2 for the fit. The results of this analysis are summarized in Table 3.2.

Pump pulse	600	605	610	615	620	625	630	635	640
RT TL	3±0.7	2.7±0.7	> 6	> 8	1.3±0.2	0.8±0.1	0.7±0.1	0.7±0.1	0.7±0.1
RTPC1	0.8±0.2	1.1±0.2	1±0.1	> 2.4	> 3.3	1.1±0.2	0.7±0.1	0.4±0.1	0.7±0.2
RTPC2	1±0.1	1.8±0.2	1.2±0.1	2.3±0.5	2.5±0.6	1.9±0.4	0.8±0.2	-	-
RTNC1	1.1±0.2	1.5±0.2	2±0.4	2.8±1.1	4±2.6	1.2±0.4	0.6±0.1	0.9±0.2	0.9±0.2
BB TL	1±0.2	0.7±0.1	0.8±0.1	0.9±0.1	0.9±0.2	0.8±0.2	0.8±0.1	0.9±0.2	0.9±0.2
BBPC4	1.6±0.4	1.5±0.5	0.9±0.2	1.3±0.2	1.6±0.4	1.9±0.5	1.3±0.2	1.1±0.3	1.6±0.5

Table 3.2. Effective Damping Times in Picoseconds, with Error Bars, for Red-tuned and Broadband Excitation

3.4.3 The Intensity of the Oscillations vs. the Probe Wavelength

Figure 3.8 shows the vibrational spectrum obtained from the FFT of the transient absorption data, for red-tuned TL excitation. Analysis of the shortened traces is preferred when making statements related to the amplitude of the oscillations, as discussed above. Thus, Figures 3.8-3.13 have been generated by using 256 points (850 fs). Figure 3.8 highlights the amplitude variation of the dominant 586 cm^{-1} mode as a function of probe wavelength. The main features in this plot are the equally intense peaks on the red and blue sides of the peak of the ground-state bleaching (615 nm) and the gap in the intensity of the oscillations between 610 and 630 nm. Figures 3.9 and 3.10 plot the amplitude of the dominant mode in the Fourier transform as a function of the probe wavelength for data taken with negatively and positively chirped excitation pulses, respectively. The amplitudes of the oscillations observed with negatively chirped excitation again exhibit a minimum between 620 and 630 nm. However, the relative amplitudes of the oscillations on the blue and red sides of the gap depend on the magnitude of the chirp. For positively chirped excitation, the gap is not observed and the oscillation on the red side of the spectrum, in the region dominated by stimulated emission, is suppressed compared with the blue side of the spectrum. For the largest chirp, the oscillations are also suppressed on the blue side of the transient absorption spectrum. Figure 3.11 shows plots of the FFT intensity vs. the probe wavelength under excitation by the broadband TL, PC4, and NC4 pulses. The gap at 610-630 nm characteristic of RT excitation has disappeared, the most noticeable feature now being a sharp gap at 650 nm, for TL and PC excitation. The trends are less clear for the negatively chirped pulse (blue line). Plots of the results of the FFT analysis for the BT1 and BT2 excitation pulses are shown in Figures 3.12 and 3.13. None of these plots exhibit any minimum around 615 nm, although a minimum near 650 nm is observed for TL and PC0 excitation. To test the reproducibility of the spectral variations in FFT amplitude, a series of consecutive scans, performed under the same excitation conditions, were analyzed independently and the results compared. The variation of the FFT intensity profiles was within (15% from run to run. The minimum observed at 650 nm can be observed to some degree for all the runs but appears the most clearly in the analysis of the averaged trace.

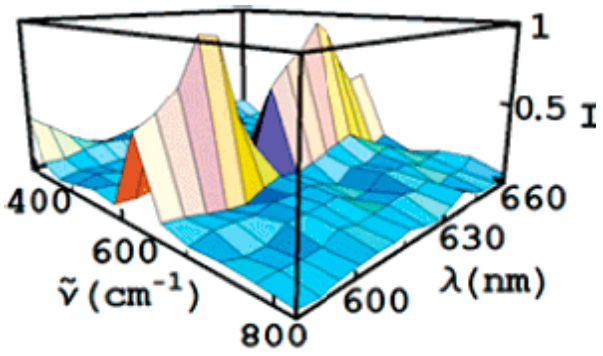

Figure 3.8. Fourier power spectrum produced under excitation with the red-tuned TL pulse.

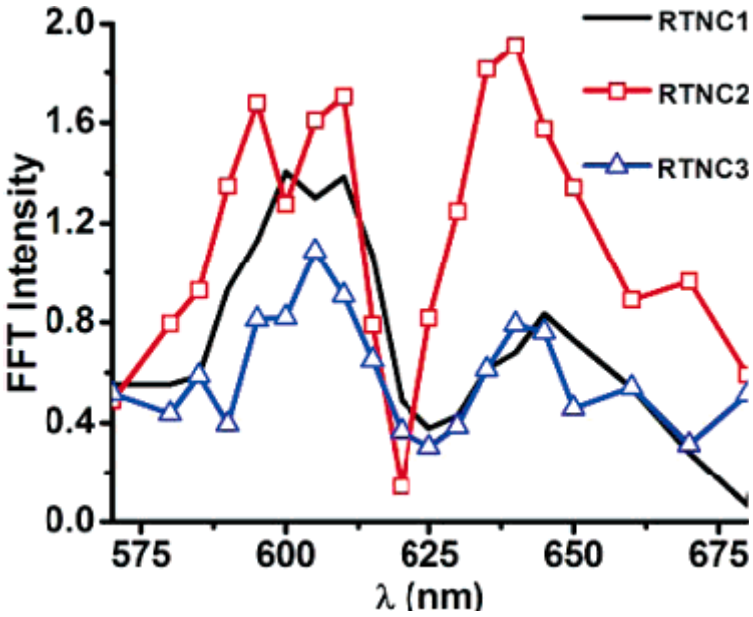

Figure 3.9. Fourier intensity of the ring-breathing mode vs. the probe wavelength, for red-tuned excitation: black line, NC1; red with squares, NC2; blue with triangles, NC3.

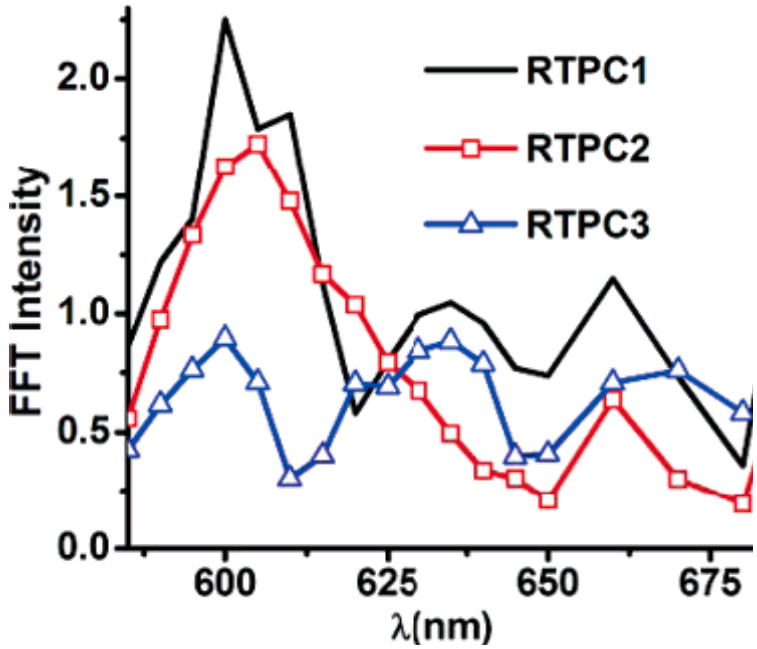

Figure 3.10. Fourier intensity of the ring-breathing mode vs. the probe wavelength, for red-tuned excitation: black line, PC1; red with squares, PC2; blue with triangles, PC3.

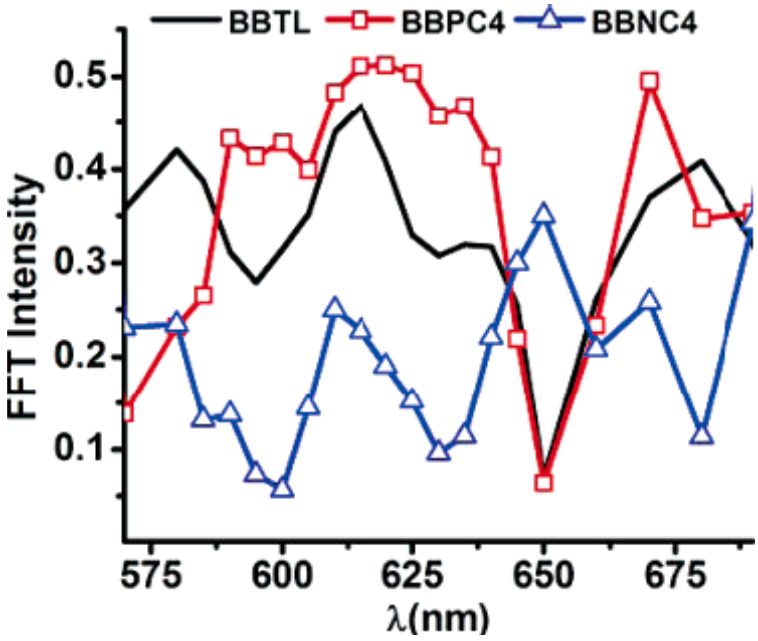

Figure 3.11. Fourier intensity of the ring-breathing mode vs. the probe wavelength, for broadband excitation, with TL (black line), PC4 (red line with squares), and NC4 (blue line with triangles) phase profiles.

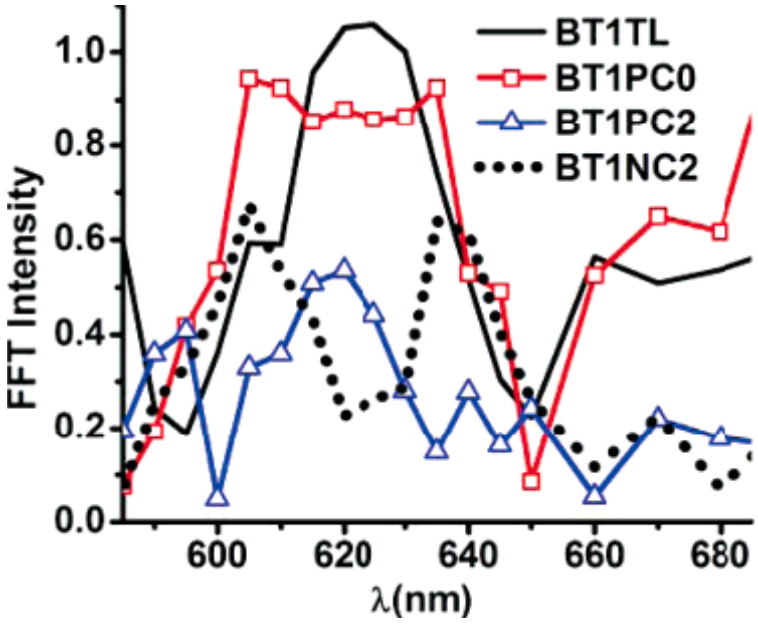

Figure 3.12. Fourier intensity of the ring-breathing mode plotted as a function of the probe wavelength, for BT1 excitation, with TL (black line), PC0 (red line with squares), PC2 (blue line with triangles), and NC2 (dotted line) phase profiles.

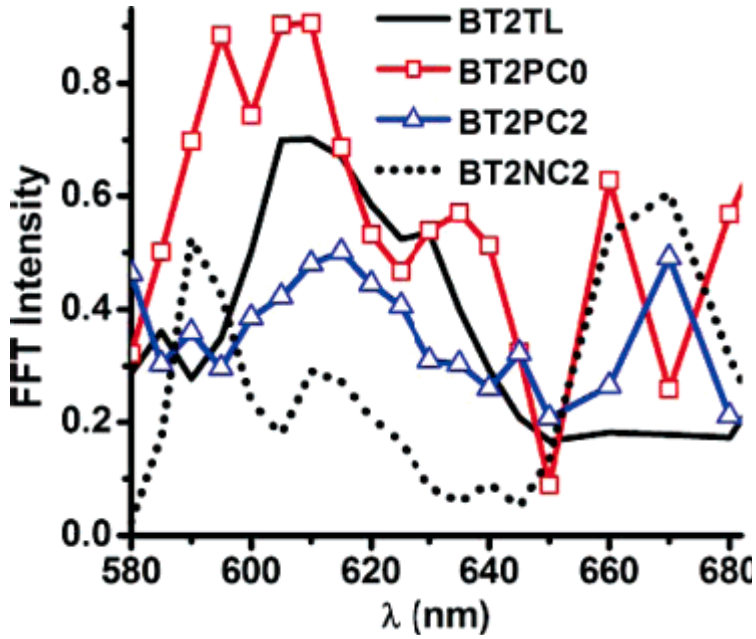

Figure 3.13. Fourier intensity of the ring-breathing mode plotted as a function of the probe wavelength, for BT2 excitation, with TL (black line), PC0 (red line with squares), PC2 (blue line with triangles), and NC2 (dotted line) phase profiles.

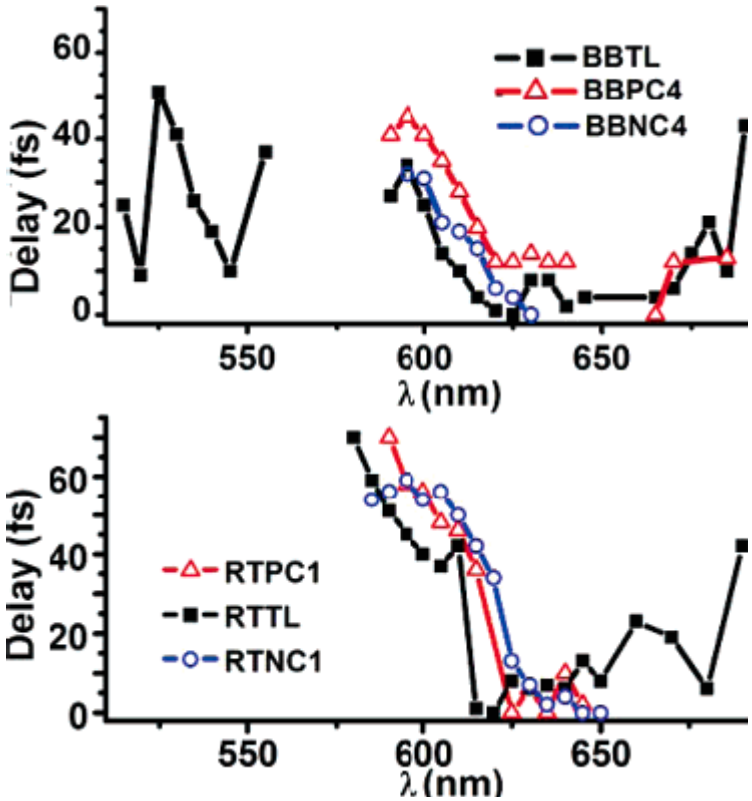

Figure 3.14. Bottom panel: wavelength dependence of the relative phase of the oscillations for RT excitation, with the TL (black line with squares), PC1 (red line with triangles), and NC1 (blue line with circles) phase profiles. Top panel: wavelength dependence of the phase of the oscillations for BB excitation, with the TL (black line with squares), PC4 (red line with triangles), and NC4 (blue line with circles) phase profiles.

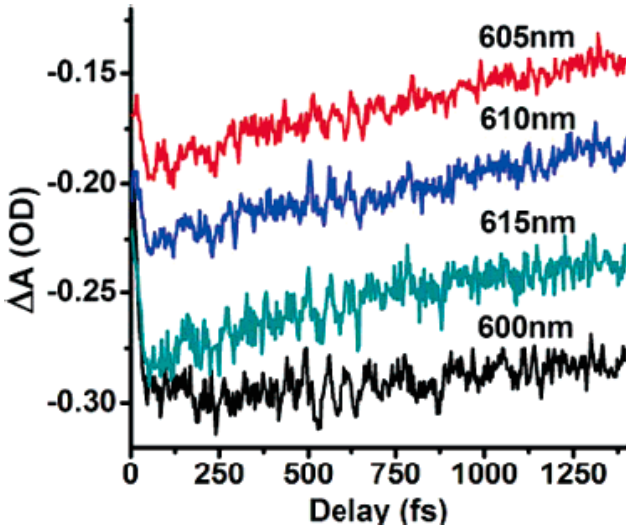

Figure 3.15. Kinetic traces obtained using negatively chirped broadband excitation for the probe wavelengths indicated on the figure.

3.4.4 The Phase of the Oscillations as a Function of Wavelength

The phase of a coherent oscillation as a function of wavelength can also shed light on the nature of the vibration [37]. The wavelength-dependent phase profiles for the red-tuned and broadband excitation pulses are presented in Figure 3.14. For both broadband and red-tuned excitation pulses, the phase profiles depend approximately linearly on the probe wavelength between 580 and 625 nm, with slopes between 1 and 1.3 fs/nm. For the transform-limited broadband excitation pulse, the oscillations were apparent for wavelengths as short as 520 nm and the phase was determined over the entire range. In this case, the phase difference exceeded the period of oscillation and was wrapped accordingly. On the other hand, the phase profile is relatively flat from 625 to 700 nm within (5 fs in the regions where the intensity of the oscillation is sufficient to permit determination of phase.

3.4.5 Revivals in the Coherent Oscillations

The results described above indicate that broadband pulses with negative chirp act to suppress the observed coherent oscillations. This is an interesting result and can be considered in more detail by inspecting the kinetic traces observed following excitation with these pulses. Line-outs between 600 and 615 nm are plotted in Figure 3.15. The oscillations are very weak right after t_0 but exhibit a clear increase approximately 500 fs later. Under all the other excitation conditions, the oscillatory contribution to the signal exhibits a typical exponential decay, without clear revivals, as shown for the data in Figure 3.5. It is difficult to model these data quantitatively, but this trend is qualitatively consistent with out-of-phase ground and excited-state ring-breathing vibrations and sub-picosecond dephasing. Blue-tuned broadband excitation enhances the excited-state vibrational coherence while negative chirp favors the dumping of the population back to

the ground state, enhancing ground-state coherences. These two competing processes could combine to give the signals observed in Figure 3.15.

In the case of transient scans performed under other excitation conditions the analysis of the oscillatory component allows the retrieval of the frequency, phase or dephasing time. These, in turn, show what the corresponding electronic potential energy surface is. The oscillations in Figure 3.15 are very short lived and the retrieval of the corresponding characteristics is difficult. The FFT analysis retrieves an oscillation frequency 10 cm^{-1} blue shifted compared to the 568 cm^{-1} excited state frequency. This suggests that the ground state contribution is dominant. Future molecular dynamics simulations could clarify the origin and behavior of this feature.

3.5. Discussion

The experimental results outlined above demonstrate that the phase, amplitude, dephasing time, and frequencies of the oscillations observed in the transient difference spectrum following excitation of LD690 depend strongly on the pulse characteristics, including both the pulse spectrum and the spectral phase. Because a transient absorption measurement probes ground and excited electronic states simultaneously, the assignment of the observed features is nontrivial. A number of earlier experimental and theoretical investigations have explored various aspects of this problem [37, 83-90]. In an early experiment, Joo and Albrecht used an excitation pulse spanning the region from 590 to 645 nm to measure the time-resolved four wave mixing signal from LD690 in ethylene glycol [90]. This pulse is similar to the red-tuned pulse in Figure 3.2. Two vibrational modes at 572 and 586 cm^{-1} were extracted from the oscillatory signal. The 586 cm^{-1} mode was assigned to the ground-state ring-breathing mode, which dominates the resonance Raman spectrum of LD690. The 572 cm^{-1} mode was tentatively assigned to an excited-state vibrational mode, presumably corresponding to the normal coordinate observed at 586 cm^{-1} in the ground state. Joo and Albrecht also find that the vibrational dephasing time distinguishes ground (~1 ps) and excited-state (520 fs) vibrations. Bardeen et al.

have reported extensive studies of vibrational coherences in LD690 as a function of spectral phase using a broad 12 fs pump pulse spanning 100 nm of spectrum from ca. 560 to 660 nm FWHM [37]. This pulse spectrum is unlike any of the pulses used in the current work in that it spans most of the LD690 absorption band and extends through the region of the LD690 fluorescence spectrum as well. Despite this difference in excitation spectrum, the trends observed by Bardeen et al. are similar to those reported here for the red-tuned excitation pulse, although there are a few significant differences. Both data sets are dominated by a vibrational coherence with a frequency of 586 cm^{-1}. Bardeen et al. also observe a 571 cm^{-1} vibration but suggest that it is ground state in origin, appearing as a small shoulder on the highly displaced 586 cm^{-1} peak in the Raman spectrum. In fact, Bardeen et al. find no evidence requiring a change in vibrational frequency between the ground and excited electronic state. Thus, any given oscillatory signal could in principle arise from either a ground or an excited-state wave packet. Ground and excited-state vibrations are identified primarily by comparison with theoretical calculations and by the influence of the electronic state on the vibrational dephasing time. However, the degree of vibrational excitation within the S_1 or S_0 state also influences the dephasing time.

3.5.1 The Oscillation Frequency

One key feature of the experimental results presented here is the dependence of the oscillation frequency on both the spectrum of the pump pulse and the probe wavelength. The frequency of the coherent oscillations observed with excitation pulses centered in the blue is consistently lower than the frequency observed following excitation with red-tuned pulses (see Figures 3.6 and 3.7). For broadband transform-limited excitation, the frequency is $\leq$ 568 cm^{-1} on the blue side (<590 nm) and $\leq$ 570 cm^{-1} on the red side (>640 nm). For all probe wavelengths, the frequency is $\leq$ 578 cm^{-1}. The interpretation of the wavelength dependence of the oscillation frequency is based on the assumption that at any probe wavelength the signal represents a mixture of ground and excited-state coherences. The dephasing time of the vibrational wave packets, the signal-

to-noise ratio of the data, and the range of time-delay measured all serve to limit the accuracy with which vibrational frequencies are extracted from the data. Thus, the measured frequency at each wavelength represents a weighted average of the ground and excited-state frequencies. The spectral regions below 550 nm and above 670 nm are dominated by excited-state absorption and excited-state stimulated emission, respectively. Accordingly, the lower frequency (ca. 568 cm^{-1}), observed in these spectral regions following blue-tuned excitation, likely represents the true excited-state frequency. A modest frequency shift is often observed for excited-state vibrations [80, 82, 85, 86, 89] and thus, it is not unreasonable to observe a 2-3% decrease in the frequency of the ring breathing mode in LD690. This interpretation of the data is consistent with the observations around 615 nm for both red-tuned pulses and blue-tuned pulses, where the vibrational frequencies converge toward an average value. The ground-state contribution to the Fourier power spectrum exhibits a minimum at the peak of the ground state bleach, tending to emphasize the importance of excited state contributions to the signal, and as a consequence, the observed frequency with following excitation with RT pulses decreases in this region as the excited-state and ground-state contributions become comparable [37]. On the other hand, the dominant contribution to the transient absorption signal in this region is the ground-state bleach, which tends to emphasize the importance of the ground-state wave packet. Thus, the observed frequency increases in this region following excitation with BB or BT1/BT2 pulses, as the excited-state and ground-state contributions become comparable. The analysis of the FFT spectra for negatively chirped broadband excitation (not shown in Figure 3.6 because the frequency could be retrieved only for a few probe wavelengths) also shows a blue frequency shift of 10 cm^{-1} compared with the transform-limited and positively chirped pulses. Finally, the recurrence observed for these negatively chirped pulses is consistent with beating between out-of-phase ground and excited-state oscillations of slightly different frequency. While the present work does not completely rule out a ground state origin for the observed 566-576 cm^{-1} vibrations, the predominance of the red shift in the spectral regions dominated by excited-state absorption and stimulated emission from the excited state are consistent with wave packet oscillation in the S_1 state. Thus, the data presented here provides strong evidence

for a small frequency change in the dominant ring-breathing mode between the ground and excited electronic states.

3.5.2 Vibrational Dephasing

The dephasing time of the observed oscillations is characteristic of both the average vibrational excitation within an electronic state manifold and the assignment to the ground or excited electronic manifold [89, 91]. For the data obtained in these experiments, Table 3.2 contrasts the cases of broadband and red-tuned excitation. Under RT excitation, the dephasing near the peak of the ground-state bleach (ca. 615 nm) is very slow. This is consistent with the model of Bardeen et al. where ground-state coherences dominate the signal in this region. Because the ground-state wave packet is produced near the bottom of the harmonic well, involving a few low-lying vibrational levels, it has a long damping time. For BB excitation, the dephasing times are 0.7-1.9 ps for all probe wavelengths and no clear trend can be established. The fact that for BB pulses the dephasing is as fast around 615 nm as for the other wavelengths suggests that the coherences are produced in the excited state. However, a faster dephasing time is also consistent with the production of a higher energy ground-state wave packet. Excitation energy overlapping with the vibronic structure of the absorption spectrum, as it is the case for BB pulses, will lead to the excitation of higher ground state vibrational levels, with consequent faster dephasing of the wave packet. Finally, it should also be noted that the influence of the beating between the ground and excited-state frequencies may also affect the apparent dephasing rate in any given measurement. It is interesting that the positively chirped broadband excitation pulse leads to slower dephasing than observed for the spectrally equivalent transform-limited pulse. Following excitation with a positively chirped pulse, the excitation process produces both ground and excited-state wave packets and the observed frequency is a weighted average of the ground and excited-state frequencies. The apparent dephasing time is ca. 1.4 ± 0.5 ps across the spectrum from 600 to 640 nm arising from the dephasing of the ground-state wave

packet, the excited state wave packet, and the influence of the beating of these two contributions. In the absence of a simulation utilizing a model including both ground and excited-state contributions, it is difficult to separate these effects. With BB TL excitation, the observed oscillations have consistently lower frequency and are dominated by the excited-state coherence. The dephasing time (0.85 ± 0.15 ps) arises from the dephasing of the wave packet in S_1.

3.5.3 The Intensity of the Vibrational Coherences

For a one dimensional displaced harmonic oscillator, the centroid of the difference spectrum shifts linearly to lower frequencies as the wave packet moves away from the Franck-Condon region [90, 92]. The broad probe spectrum used in these experiments effectively samples the wave packet at different regions of the potential energy surface. The signal measured at each probe wavelength is then sensitive to the time-dependent character of the vibrational wave packet. The motion of the wave packet also results in time-dependent Franck-Condon factors. Through these two mechanisms, the magnitude of the observed oscillations in the time-resolved absorption depends on probe wavelength. This dependence is clearly observed in Figures 3.8-3.10 following excitation with red-tuned pulses. A minimum in the oscillation strength is observed between 610 and 630 nm under TL and NC excitation. No systematic dependence on the magnitude of the chirp is apparent however. Positive chirp also influences the spectrum, with increasing positive chirp serving to decrease the amplitude of the oscillations, especially for longer wavelengths. These trends are also consistent with those measured and simulated by Bardeen et al. [37]. In contrast to the spectral profiles obtained with red-tuned excitation, the data obtained with broadband or blue-tuned excitation pulses shows little evidence for a minimum around 610-620 nm. The only possible exception to this is the BT1 NC2 profile (Figure 3.12 dotted line). Rather, the data is characterized, on average, by a minimum around 650 nm for transform-limited and positively chirped excitation and a relatively flat profile for negatively chirped excitation (except perhaps

for BT2 NC2). This is again consistent with blue-tuned excitation producing coherences predominantly on the S_1 excited electronic state.

3.5.4 The Phase of the Oscillations

The phase profiles shown in Figure 3.14 can be used to extract information regarding the wave packet dynamics in the ground and excited state. In recent work, Carson et al. [88] analyzed the phase of coherent oscillations in the dye IR144 to separate the regions where the ground or excited-state contributions dominate. A π phase shift was observed as the probe wavelength was swept from a region dominated by ground state coherences to a region dominated by excited-state coherences. Detailed theoretical analysis by Kumar et al. showed that a $\pm\pi$ phase jump is expected at the peak of the absorption and florescence spectra for pure ground or excited-state oscillations [84]. In the present work, a $\sim \pi$ phase jump is observed for red-tuned excitation at a probe wavelength close to the peak of the absorption spectrum. For the broadband excitation pulse, the phase changes slowly around 620 nm. The lack of a phase jump supports an excited-state assignment. Although a phase jump is expected between 640 and 650 nm, the absence of strong oscillations prevents characterization in this region. An interesting feature in the data is a fast phase change around 530 nm, where excited-state absorption dominates the transient absorption signal. This fast phase change could reflect the steep slope of the excited state potential energy surface, given the 110 nm separation from the bottom of the excited state well (~ 640 nm).

3.5.5 Involvement of Higher Excited States

A final point to be discussed is the influence of higher excited states on the molecular dynamics in the first excited state. The spectral profile and the magnitude of

the $S_1 \rightarrow S_n$ excited-state absorption can be estimated by computing the difference between the normalized transient and static absorption spectra. The result is presented in Figure 3.16 and should be taken only as a guide.

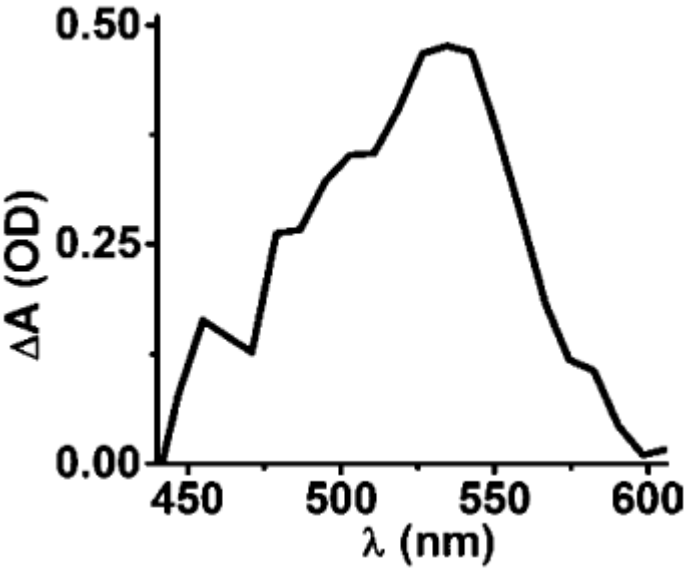

Figure 3.16. Estimated absorption profile of the first excited electronic state.

Since the red-tuned excitation pulse does not have a significant overlap with the excited-state absorption, only the first two electronic levels will be involved in the excitation process. On the other hand, the three blue-tuned pump pulses are resonant with both the $S_0 \rightarrow S_1$ ground-state transition and the $S_1 \rightarrow S_n$ excited state transition. Thus, an excitation mechanism with S_1 population produced by coherent or incoherent passage through the S_n state may influence the observed coherences. A three-photon mechanism with population of S*n* followed by ultrafast dumping to the first excited state may influence the successful creation of vibrational wave packets on the S_1 excited state. Alternatively, two-photon excitation of the S_n state followed by rapid, presumably incoherent, internal conversion from S_n to S_1 would suppress the formation of excited-state wave packets. The mechanism of coherent multi-photon excitation is under investigation and will be the subject of a future publication. The time window investigated here does not include the immediate vicinity of the coherence spike, thus we cannot speak to the mechanism controlling the magnitude of excited-state coherences.

The inspection of the pump-probe scans analyzed here shows no identifiable contribution that could be assigned to internal conversion from the S*n* state populating the S_1 state.

3.6. Conclusions

The combination of spectral tuning and simple shaping of the excitation pulses leads to rich wave packet dynamics in the LD690 dye molecule. The work reported here explored the dependence of the oscillation frequency, amplitude, phase, and dephasing as a function of probe wavelength on the spectrum and linear chirp of the excitation pulse. Our analysis is based on the simple model of displaced harmonic oscillators and makes comparison to previously published experimental work for analogous excitation conditions. The emerging picture suggests that spectral shaping can enhance the ability to selectively excite ground or excited-state coherences. Specifically, tuning the pump spectrum to the blue edge of the absorption spectrum, in connection with TL or PC phase profiles, results preferentially in excited-state wave packets. Changing the spectrum influences the effect of chirp. Most notable, the frequency of the oscillations is found to be 586 cm^{-1} under conditions that favor the formation of ground-state coherences, 568 cm^{-1} under conditions favoring the formation of excited-state coherences, and at intermediate values representing a weighted average of these frequencies under conditions where both ground and excited state coherences are excited. The observed influence of chirp and spectrum on the dephasing and the spectral profile of the oscillations provide additional support for this conclusion. The LD690 molecule is a rigid, unreactive laser dye. However, these results suggest that a systematic search of the excitation conditions including both pulse spectrum and phase may lead to excitation conditions permitting control of reaction dynamics in reactive chromophores. These results also highlight the need for theoretical models that realistically reproduce the experimental conditions to model ground and excited-state coherences, with possible involvement of higher excited states at the earliest stages of the process.

Chapter IV

Control of Retinal Isomerization in Bacteriorhodopsin

4.1 Introduction

4.1.1 Bacteriorhodopsin Chemistry

Bacteriorhodopsin (bR) is a protein found in the purple membrane of *Halobacterium salinarum* [93, 94]. *Halobacterium salinarum* is part of one of the oldest families of living organisms on Earth, *Archaea*, which developed more than three billion years ago. The distinct feature of *Archaea* is their adaptation to extreme environments such as temperatures above 100^0 C and very high salinity or acidity. *Halobacterium salinarum* is part of the halophiles subgroup and is found in salty marshes. Bacteriorhodopsin, through its light absorption and energy storage function, plays an important role in the adaptation of the organism to this hostile environment. The bacteriorhodopsin molecules are organized in triplets, which form hexagonal two-dimensional crystals covering up to 50% of the surface of the archaeal cell. They consist in seven helices. The molecule responsible for light absorption, retinal, can be found buried deep between them. An image of retinal is presented in Figure 4.1.

Retinal is found in a large array of light-absorbing cells, most notably in the photoreceptor cells of the retina. Its function, chemistry and absorptive properties change

significantly depending on the environment. When absorbing a photon retinal changes its shape, going from an all-trans configuration to a cis conformation or vice-versa [7, 42, 43, 93-97]. All-trans retinal in solution has a peak absorption spectrum in the near-UV, around 400 nm. However, in a cell environment, the absorption peak can be close to 550 nm, which is the peak of the sun spectrum.

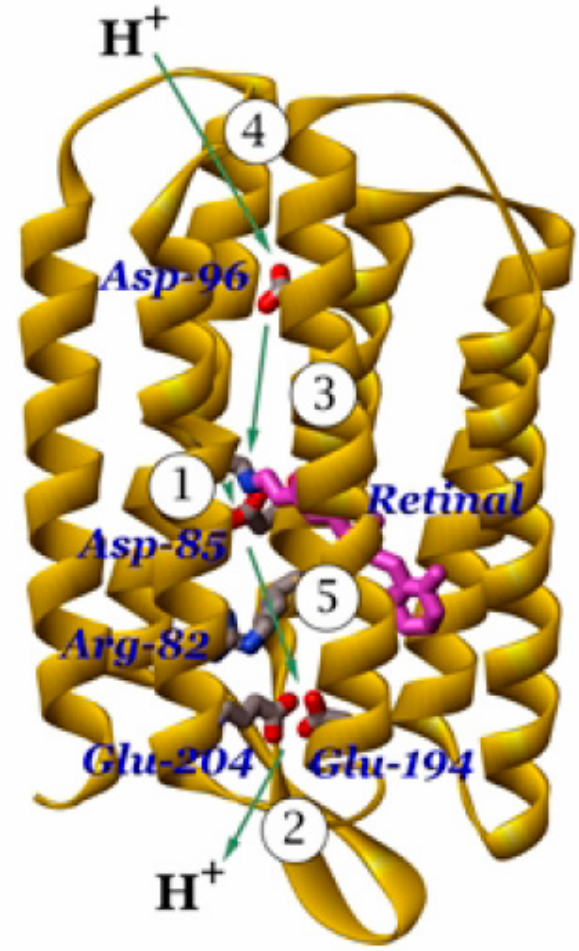

Figure 4.1. An overview of the seven-helical structure of bacteriorhodopsin. The all-trans retinal is shown in purple, important residues in blue. The path of proton translocation is shown with green arrows. Protonation/deprotonation steps follow one another as numbered: *step 1* is protonation of Asp-85 by the Schiff base, *step 2* is proton release to the medium, *step 3* is reprotonation of the Schiff base by Asp-96, *step 4* is reprotonation of Asp-96, and *step 5* is proton transfer from Asp-85 to the proton release group. (Image and caption reproduced with permission from Professor Janos Lanyi;

Luecke et al. Science 286, 255-260, 1999. Copyright 1999 American Association for the Advancement of Science).

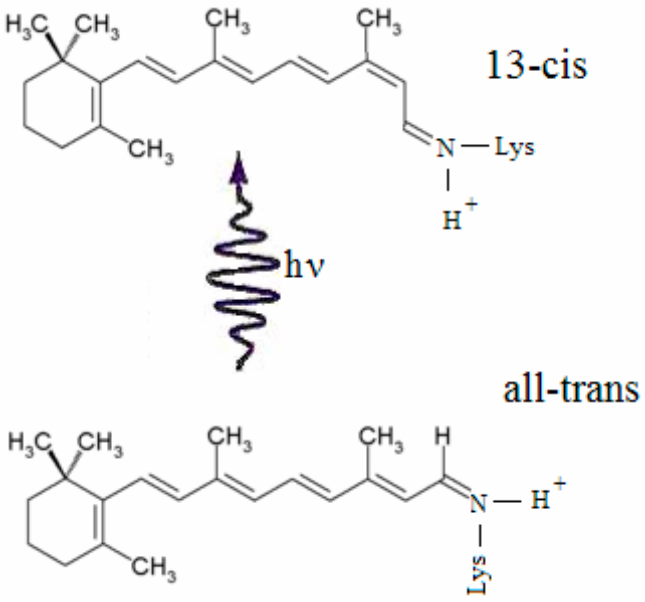

Figure 4.2. Retinal isomerization from the all-trans to the 13-cis isomer after photon absorption. Retinal is coupled to the environment (i.e. Lys-216 and the rest of the bR molecule) through a protonated Schiff-base.

The isomerization of retinal in bR is different from the isomerization reaction of retinal in the eye's photoreceptor cells. In the eye retinal is found predominantly in the 11-cis conformation and light absorption triggers the conversion to the all-trans isomer. The change in shape cannot be accommodated by the cell environment. The mismatch triggers larger scale changes culminating with the transmission of an electric signal to the brain. In bacteriorhodopsin the isomerization process involves the all-trans → 13-cis transition. As in vision, large scale changes are triggered (the helices bend), which makes possible the transfer of a proton from one side to the other of the membrane [94]. The electric potential difference is used to store energy, helping the normal functioning of the archaeal cell [98].

The isomerization reaction is the initial step of a long cycle of bR intermediates, which are labeled bR_{570}, I_{460}, J_{625}, K_{590}, L_{550}, M_{412}, N_{520} and O_{640} [95, 96]. K_{590} represents

the 13-cis conformation and bR_{570} designates the light-adapted, all-trans bR conformer. The subscripts designate the peak absorption wavelength. After the initial photon absorption the $bR_{570} \rightarrow I_{460} \rightarrow J_{625} \rightarrow K_{590}$ segment of the reaction is finished in about 40 ps. These early time changes will be the focus of the present study. The next steps take tens of microseconds or milliseconds to complete and, while having a large scientific and industrial importance, are not discussed in this work.

Bacteriorhodopsin has been studied intensively in the ultrafast spectroscopy community over the last decades [19, 33, 37, 39, 40, 43, 97-113]. A large range of techniques have been used, with emphases on various aspects of the isomerization reaction. The core question is to elucidate the potential energy surface structure of bR, both in the ground and the first excited state. Once the potential energy surfaces are known the molecular dynamics can be understood. Very quickly it has been realized that various molecular vibrational degrees of freedom play a significant role in the isomerization process and their coupling with each other and with the electronic PES needs to be explained [37, 40, 43, 99, 101, 107, 113]. Another focus is the role of the environment, in particular Lys-216, the retinal Schiff base binding site which connects the retinal with the seven-helix structure [97, 109]. A significant number of experimental works are published each year and theorists try to create consistent theories to incorporate them. Significant progress has been made, but points of debate still exist [7, 42, 93].

In what follows we present the bR model which gained the largest acceptance in the scientific community. Figure 4.3 shows a plot of the potential energy surfaces (PES) in bR. The initial state is the light adapted form, which can be obtained by ambient illumination for a couple of hours. This state is characterized by all-trans geometry (see Figure 4.2, bottom molecular structure). After photo-excitation the H conformer is reached. It designates the excited state conformation situated vertically above the ground state minimum. Its existence has been deduced indirectly from ultrafast experiments and its direct spectral identification is still waiting. Its main proof of existence is the fact that the stimulated emission and absorption signals from the next intermediate conformer, I_{460}, appears with a ~ 100 fs delay after the initial photo-excitation event. One difficulty with the spectroscopic analysis of the bR intermediates is that they have broad and very similar absorption spectra (spectral congestion). In addition many processes (absorption,

stimulated emission, fluorescence) can contribute to the observed signals, making their identification hard. Overlapping absorption and stimulated emission features could cancel each other. The direct observation of H is likely hindered by the spectral congestion. From H the excited wave packet slides down to the I_{460} conformation, whose absorption signal reaches its peak 200 – 300 fs after excitation. In many molecular systems the excited state experiences a (Stokes, or red) shift of the peak absorption or stimulated emission wavelength, because the wave packet slides down towards the PES minimum. This is common in laser dyes for example. The lack of a red-shift for I_{460} suggests the existence of an excited state barrier through which the wave packet leaks towards the bottom of the excited state PES (see Figure 4.3). Theoretical calculations showed that bR has a number of excited potential energy surfaces. They intersect, resulting in a number of conical intersections. The small barrier in Figure 3 is the result of the intersection between the A_g and B_u electronic PES. After passing over the barrier the population reaches the bottom conical intersection (CI), from which it can go either towards the all-trans or the 13-cis conformation. This intermediate zone has been assigned to the J_{625} conformation. There is an ongoing debate regarding the fact that this state is situated before or after the CI. Vibrational spectroscopy studies showed that the J_{625} state does not exhibit vibrational modes characteristic for a planar molecular geometry so it must represent an intermediate, orthogonal geometry. This supports its assignment to the conical intersection region. The model presented above is named “the three-state model” in literature, because the barrier requires the presence of another excited PES, as explained above. The alternative model, “the two-state model”, does not accept the existence of the barrier and lost some traction in the last years. Both models fail to explain the full range of experimental observations. Additions and revisions are frequently made.

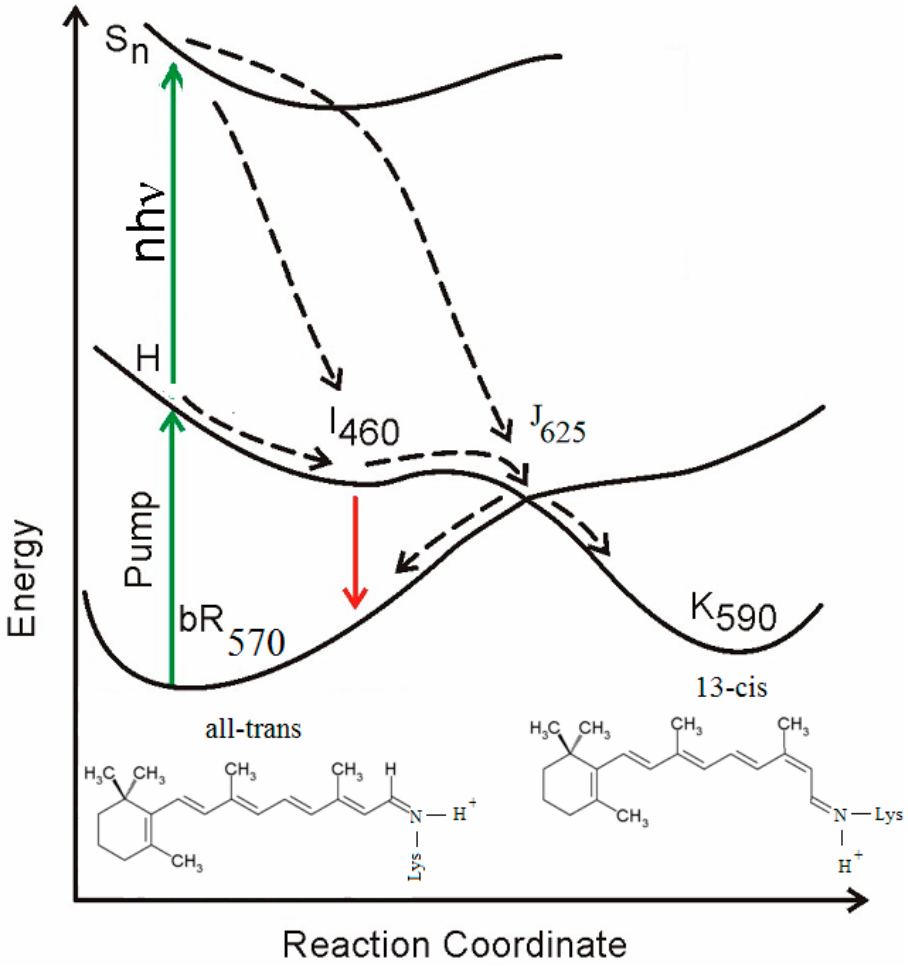

Figure 4.3. The three-state model of retinal isomerization in bR. Straight vertical arrows designate photon interactions (green: pump absorption; red: stimulated emission). The dashed-line arrows describe molecular dynamics.

Another point of high interest is represented by the bR vibrational modes. Bacteriorhodopsin exhibits a large number of vibrational degrees of freedom which are coupled with each other. Among these the torsional angle plays the dominant role because it represents the isomerization coordinate (the horizontal axis in Figure 4.3) [101, 108]. The corresponding oscillation frequency is about 160 cm^{-1}. Femtosecond studies showed that this mode is not excited for T < 200 fs. Bacteriorhodopsin variants containing synthetic retinal for which the $C_{13} = C_{14}$ bond is locked exhibit the same chemistry as native bR in the first ~ 200 fs [103]. After 200 fs the initially excited modes

couple with the torsional mode and the isomerization process is initiated. A femtosecond study of the vibrational dynamics in the 900 cm^{-1} – 1800 cm^{-1} window has been reported by Kobayashi [40]. The vibrational regions are: 1,500 - 1,650 cm^{-1} (C = C and C = N stretching modes), 1,150 - 1,250 cm^{-1} (in-plane C = C - H bending coupled with the C - C stretching modes) and 900 - 1,000 cm^{-1} (the hydrogen-out-of plane or HOOP mode). He finds that these modes are modulated in intensity with a frequency close to 160 cm^{-1}, assigned to the torsional mode. The HOOP frequency in particular is strong only when the molecule is aligned in a plane because for orthogonal geometries the "out-of-plane" direction is not well defined. As such, the HOOP mode is a direct witness of the molecular distortions. Studies employing IR beams have directly recorded the absorption bands due to the bR vibrational modes. Due to the change in shape their frequency is slightly shifted [99]. Herbst et al. [102] monitored directly the transient femtosecond IR absorption of these modes.

These are just a few of a large number of works on this subject. Our studies employ 20 fs long excitation pulses which are not capable of exciting the high frequency modes mentioned above. We do see oscillations corresponding to the torsional mode which are analyzed with the final goal of maximizing the 13-cis yield in mind. But, unlike the LD690 study, the vibrational modes are not the main focus of our work. Future experiments involving ~ 10 fs excitation pulses could bring more information on this subject.

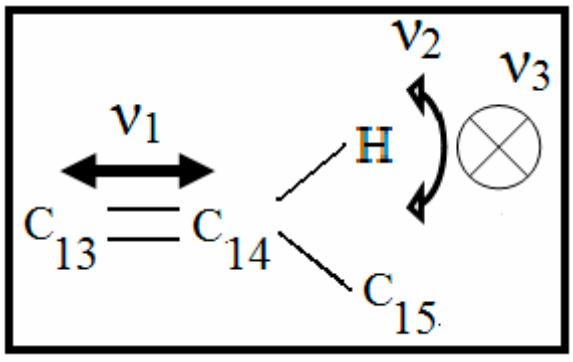

Figure 4.4. The main high frequency modes involved in retinal isomerization. ν_1 = 1150 – 1250 cm^{-1}, ν_2 = 900 – 1000 cm^{-1}, ν_3 = 1500 – 1550 cm^{-1}. The third mode is the hydrogen-out-of-plane vibration, which can serve as a "marker" of the planarity of the molecule.

4.1.2 Coherent Control of Complex Molecules

One of the goals of coherent control is to manipulate (i.e. to maximize and/or minimize) the outcome of complex bio-chemical reactions [8-11, 13-15, 30, 33]. This is challenging because bio-molecules are very large, making theoretical modeling difficult. In addition it is not obvious that quantum mechanics should play a role at the physical scale where many of these bio-molecules operate [114]. Despite these difficulties a number of large molecules have been controlled. Among these we can enumerate the light-harvesting antenna complex LH2 [115] and the green fluorescent protein [116]. Control has been reported even for live cells [38]. Bacteriorhodopsin is certainly on the list of the most interesting candidates for a coherent control experiment [9, 19, 117, 118]. The target is the maximization of the 13-cis yield. A first successful control study has been reported by Prokhorenko et al. [33]. The excitation pulses were very weak (~ 20 nJ energy or 2.7×10^{14} photons/cm^2 fluence) and centered at 570 nm, where the peak of the absorption spectrum is situated. In this regime only one in 10 molecules absorbs a photon, which is close to the intensity regime expected in a natural environment. As a consequence this control experiment deals with natural, biologically relevant excitation conditions. The genetic algorithm found that a complex, amplitude and phase-shaped pulse increases the isomerization yield (that is the 13-cis population) by about 20% compared to a transform-limit pulse. A similar 20% minimization control experiment has been performed. The two GA solutions present very sharp spectral features. The optimal solution is blue-shifted spectrally while the anti-optimal solution is red-shifted spectrally. FROG characterization showed that the control pulses exhibit a regular time-domain pattern, with multiple peaks separated by about 200 fs, which is close to the period of the torsional mode vibrations. The interpretation was that the GA finds this mode and drives it, controlling in this way the isomerization process. Transient scans showed, indeed, oscillatory features with ~ 200 fs period. However these features exist only when the pump and probe overlap temporally, and should be present in any correlation measurement, regardless of medium (the coherent spike). Transient scan measurements reported in other works show vibrations lasting for longer times (1 – 2 ps) than those

reported in [33]. This work opened the door for bR control and served as an inspiration source for the study presented below.

Another work reporting control over the final isomerization yield is that of Gerber et al. [39] They have used very energetic (~ 400 nJ) excitation pulses at 400 nm to excite the all-trans population to a higher excited state. Given the lack of knowledge regarding higher potential energy surfaces in bR we will denote them generically as S_n. The excited population relaxes quickly to the first excited state, which is represented in Figure 4.3. Then a 800 nm dump pulse is used, at various delays with respect to the pump pulses. This pulse "steals away" population which normally would have followed a path leading to the conical intersection and then, possibly, to the 13-cis state. A GA search is performed to find the shape of the dump pulse which can results in a minimum isomerization yield and a TL pulse is found. This leads to the conclusion that the I_{460} wave packet is focused and moves fast over the barrier and this is why a TL pulse is optimal for dumping.

These two works motivated us to perform a control experiment where we would explore a larger range of intensity regimes. We tune the pulse energy between zero and the value at which self-phase modulation effects become strong, i.e. virtually all the physically reasonable regime. Our focus is to find the excitation pulses which would maximize the isomerization yield.

4.2 Experimental Setup

This experiment has been performed at Stanford University, in a new ultrafast lab. The experimental setup resembles that used for the LD690 experiment at University of Michigan. Some extra complexity is added by the special nature of the bR molecule. The bR samples have been prepared for us by Professor Janos Lanyi at University of California at Irvine. Once brought to the proper form they have been shipped to us, stored at 4^0 C and then used without further processing. Temperatures lower than 4^0 C produce freezing of the sample and decrease its bio-functionality. Before the experiment the

sample is illuminated with a 60 W visible light bulb for one hour such that almost all molecules are in the light-adapted, all-trans, form. During the experiment the sample is flowed through a fused silica flow cell (Starna Cells) of 1 mm path length. The whole flow cell area is maintained under strong ambient illumination during the experiment. The flow speed has been adjusted such that the sample is refreshed between consecutive laser shots. The choice of the cell path length has been dictated by the need for large optical signals. We have also used occasionally 0.5 mm cells with similar experimental results. Fortunately bacteriorhodopsin is one of the most robust proteins available in nature, and this increases the experimental lifetime significantly. Typically protein samples have to be discarded after a few hours of use but bacteriorhodopsin can be used for days without a significant decrease in the quality of the optical signals. This provides a tremendous advantage. However there are still a couple of issues. First of all it is necessary to minimize the effect of heating, which is due to contact with the ambient (22^0 C - room temperature) and the friction in the flow system. The bR reservoir (3 ml size) is maintained in ice, which decreases the running temperature from 25^0C to about 19^0 C. Second of all the bR is present in the solvent (a pH 7 phosphate salty buffer) as a suspension of cell membranes. Sometimes these pieces coagulate making optical experiments difficult. Sonication, as freezing, can destroy the molecules. Even in the non-aggregated form, bR in solution acts as a strong scattering medium, with two consequences: the probe signals become noisy and the pump photons can be scattered in the probe path. To minimize these effects special measures had to be taken. The optical path length after the flow cell has been intentionally increased to allow better spatial separation of the probe beam and the pump scatter. Irises and slits have been inserted in the probe path for further selectivity. Figure 5 presents the pump-probe experimental setup.

The probe is created by focusing ~ 0.5 μJ of 800 nm light in a 1 mm piece of sapphire. Before the sapphire plate the 800 nm beam is passed through a delay setup consisting in a computerized translation stage, which changes the delay of the probe with respect to the pump. A BG38 filter cuts most of the intense 800 nm component of the WL spectrum, which extends from 460 nm to 870 nm. The total WL probe energy is about 20 nJ across the full spectrum. A fraction of it (~ 30 %) is split off and used as a reference.

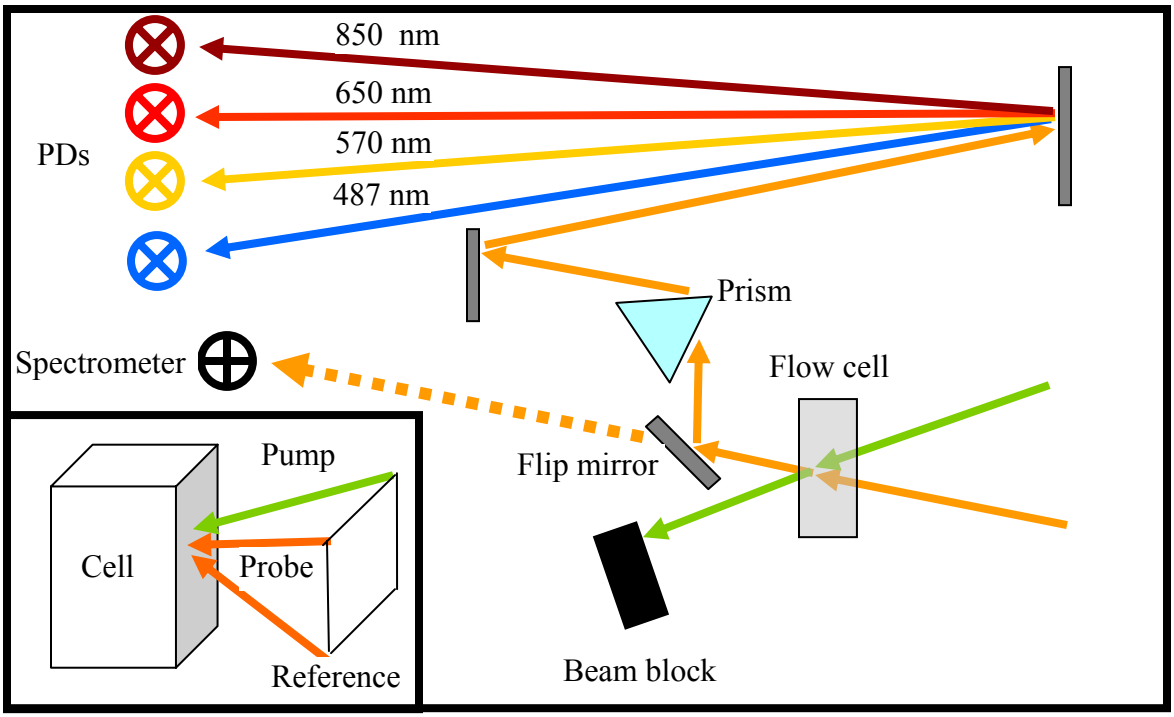

Figure 4.5. The pump - probe setup for the bR experiment, top view. The inset represents a side view, showing the three laser beams. PD = photodiode.

The reference beam is aligned such that it travels perfectly parallel with the probe beam, in the same vertical plane. The same focusing element is used for focusing them in the cell and the same recollimating lens is used after the cell, maintaining the relative alignment. The reference beam arrives at the cell 3 ns before the probe, such that it does not affect the pump-probe measurements. The probe and reference beams are sent in the same photodiode. The 3 ns separation assures the separation of their photo-electric signals. The probe and reference beam are focused with a f = 250 mm mirror in the center of the cell volume. The pump travels parallel with the probe in the horizontal plane. The overlap of the three beams is obtained with the following procedure: the cell is mounted on a triple translation stage and two crossed blades are set a few mm ahead of its front face, on the same mount. The blades are inserted in the beam path and the diffraction pattern of the three beams is checked. If the beams are intersecting at the common focus point then they will exhibit the same pattern. At focus a horizontally inserted blade will cause the beam to be clipped in the vertical direction uniformly from both sides. After the overlap has been optimized in this way a LD690 flow cell is inserted in the mount and the

stage is translated towards the focus point until a maximal bleach signal is observed. LD690 has a quite high absorption coefficient at 570 nm, causing bleach signals of ~ 200 mOD. A new overlap optimization is done with the LD690 cell in. This fine tuning accounts for cell-induced changes in the optical path. LD690 is also used for preliminary pump-probe transient measurements, in order to verify that the ultrafast setup is performing optimally. Next the LD690 and bR flow cells are swapped. The flow tubes and the reservoir are changed too, to avoid any contamination of the bR sample. No additional beam path adjustments take place after this point. After the cell the pump beam is blocked. The probe and reference beams are steered towards a flip mirror. When the mirror is flipped down the beams go to an Ocean Optics spectrometer, which allows simultaneous measurements across the full probe spectrum. Unfortunately the slow response and noise level of the spectrometer does not allow its use for the most challenging ultrafast measurements and an in – house - built monochromator is employed. When the flip mirror is up the beams are directed towards a SF10 dispersing prism. After the prism the dispersing beams are free-propagating for about 2 meters to allow enough separation between the spectral components. Then a system of slits and focusing optics send the light in a setup containing an array of amplified photodiodes (see Figure 4.5). Each photodiode is set for monitoring one of four wavelength regions: 487 nm (I_{460} absorption), 570 nm (all-trans ground state bleach), 650 nm (J_{625} and K_{590} absorption) and 850 nm (I_{460} stimulated emission). Great care is taken to minimize the pump scatter. Despite using circular masks which pass just the probe and reference beams and despite the 2 meters long monochromator pathway the pump scatter is still present at all wavelengths except 850 nm. It represents between 5% and 30% of the observed signal. The worse situation is for measurements at 570 nm. The presence of the pump scatter has a positive effect, too. At high pump intensities self-phase modulation starts to dominate and the amplified photodiode system easily picks up this point, because the pump “scatter” rises non-linearly. This intensity level defines the upper limit for our experiments. Figure 2 presents the all-trans absorption spectrum and the pump and probe spectra.

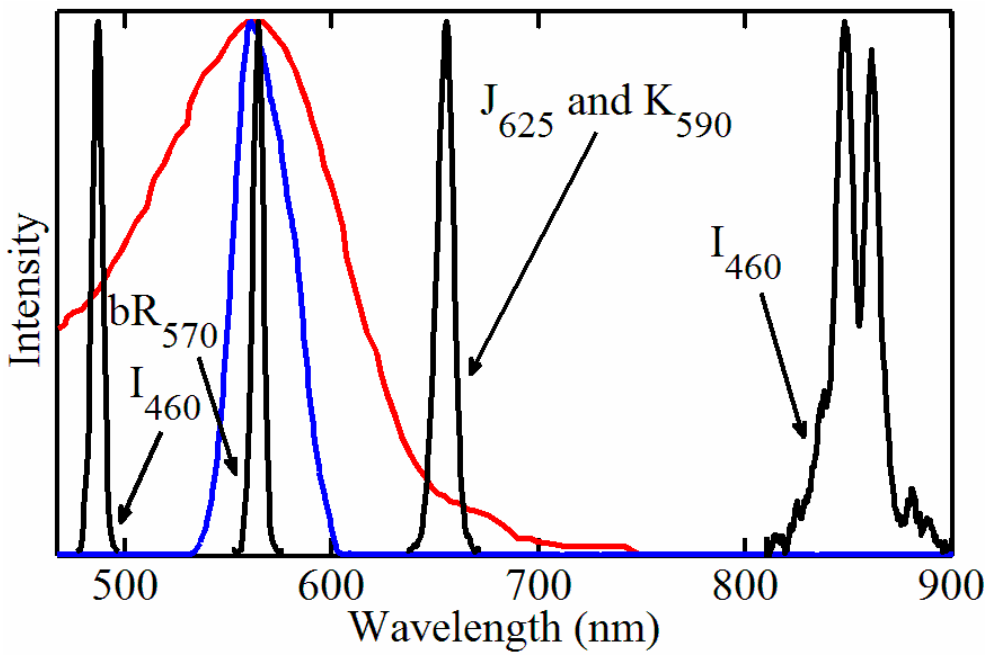

Figure 4.6. Black lines: the probe absorption spectra at 487 nm, 570 nm, 650 nm and 850 nm. Blue line: typical pump spectrum. Red line: the all-trans absorption spectrum.

A couple of types of measurements are performed with this setup. First of all GA experiments are performed while monitoring the signal at 650 nm, where the isomerization yield can be measured easily. For selected pulse shapes (TL, chirped, narrow band etc) transient scans are taken to monitor the femtosecond dynamics of the bR intermediates. Another type of measurements involves setting the probe at fixed time delays and scanning the excitation parameters (chirp, energy, bandwidth) while monitoring any of the four wavelength regions. All these measurements are performed with the goal of finding the optimal control pulse. After the pulse is found we compare the molecular dynamics triggered by this and by sub-optimal pulses in order to understand what the key differences are. The intensity, chirp and bandwidth scans are mimicking the GA search along selected search paths and complement the control experiment.

One very important issue is the intensity regime. We have carefully measured the pump and probe size in air and we found values of ~ 20 μm and 30 μm FWHM respectively. These numbers have been obtained in two ways. The first method involves inserting a blade in the beam, by means of a computerized stage, and measuring the

change in beam intensity on a photodiode. A Gaussian fit is performed on the obtained profile and the FWHM value is calculated. The second method involved an imaging system and a CCD camera to visualize the magnified focus spot. Both methods found similar size values. The pump energy is varied between 0 nJ and more than 200 nJ, but for TL pulses with 200 nJ or more self-phase modulation sets in. All measurements are performed at values at least 25% below this value. For the above quoted pump focus size we calculated a fluence of 1.5×10^{17} photons/cm^2 and an intensity of 2.5 x 10^{12} W/cm^2. The ratio between the number of molecules and the number of photons in the overlap volume is ~ 1:10. These numbers need a series of amendments however. First of all the focus size in bR could be much higher. There are reports of a strong de-focusing effect in bR films [121]. Second the overlap region is roughly in the middle section of the cell and about 50% of the photons are absorbed by that time. This figure is calculated in the following way: for a length of 1 mm / 3 = 0.33 mm and an OD of one we get $\frac{\Delta I}{I} = 10^{-1\,OD \times 0.33\,mm/1\,mm} \approx 0.5$. Third bR exhibits a strong membrane scattering effect which should further decrease the excitation intensity. All these factors could reduce the real intensity by one order of magnitude. With these amendments we still reach a regime about two orders of magnitude more intense than that reported in [33], far from the conditions encountered in nature. Our low intensity (20 nJ) experiments exhibit conditions closer to those in nature. The probe energy is about 20 nJ before reference splitting. When accounting for losses on the other optics we find a value of about 10 nJ for the energy of the probe reaching the sample. The 10 nJ are spread out over a bandwidth of more than 400 nm. Only about 3 nJ correspond to the probe spectrum overlapping with the all-trans absorption. This means that the probe energy is about 50 times smaller than the pump energy and it does not distort the population dynamics.

4.3. Genetic Algorithm Results

The genetic algorithms have been performed for a fitness function defined as the intensity of the probe absorption at 650 nm (see Figure 4.6). At this wavelength both the J_{625} (at $T < 5$ ps) and K_{590} ($T > 5$ ps) populations can be monitored. In most cases the delay was set at 40 ps, where the $J_{625} \rightarrow K_{590}$ transition is complete. The decision to set the monochromator at 650 nm was taken after inspection of transient scans taken with the spectrometer (Figure 4.7). It is easy to see that the maximum signal is at 650 nm – 660 nm.

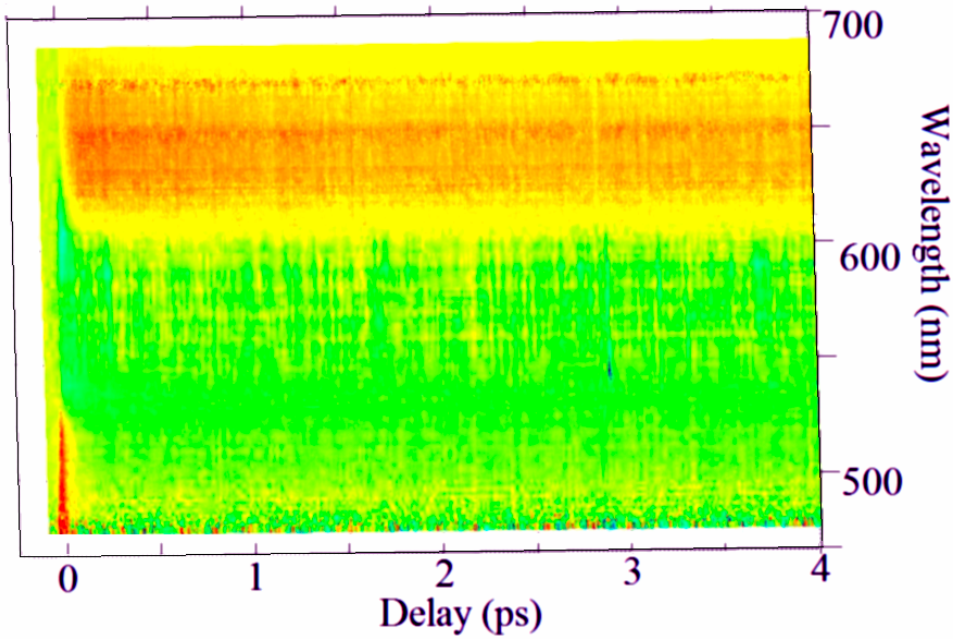

Figure 4.7. A typical pump-probe transient spectrum where the full probe spectrum is monitored simultaneously. The red area at early times around 500 nm represents the short lived I_{460} absorption. The green area represents the ground state bleach. The larger yellow-red area represents the J_{625} and K_{590} absorption. The feedback area for the GA runs has been chosen at 650 nm, where the transient absorption signal is strongest.

As explained in Section 2.4 the genetic algorithm involves finding the optimal pulse from a search space involving billions of possible pulses. An important choice to be made is the search basis from which, through linear combinations, the pulses are built.

Depending on the problem at hand the proper choice of basis set can speed up the search significantly and shed light on the inner control mechanism. In the case of bR control we did not have any preconceptions about the optimal solution and an "N π" basis set has been chosen. This basis set specifies the voltage (phase) jump between adjacent pixels and does not assume any functional relationship between them. The only condition is that the phase difference should not be bigger than a certain number, dictated by the shaping capabilities of the AOM device. We started with GAs performed at intensity levels about 25% below the self-phase modulation threshold, at 150 nJ pulse energy. The search always retrieved transform-limit (TL) pulses. It is worth noting that before each experiment the pump pulses are compressed by monitoring the SHG signal in a BBO crystal. It happened a few times that the bR GA run retrieved pulses slightly shorter than those found with the "traditional" frequency-doubling method, suggesting that the bR isomerization is more sensitive to duration than the SHG process.

To verify that the TL solution is really optimal, we diversified the search experiments. The first thing to do is to try other basis sets. For example the type of solutions found in [33] (a train of pulses) can be reproduced by a Fourier basis. On the other hand a TL solution leads naturally to a polynomial basis set, where chirp (linear, quadratic and so on) can be used to parameterize the pulses. Another approach was to force the GA to start the search further away from a TL phase setting, in the hope to find other local minima. All these experiments consistently retrieved a single solution: a TL pulse. In terms of speed the GAs using a polynomial basis proved to be fastest, converging in 10 – 15 generations. GAs using the "Nπ" basis set performed very well, too. Fourier-based GAs use sinusoidal phase functions overlapped on the TL phase profile. Their behavior consisted in turning off the sinusoidal components in order to reach the TL shape. Figure 4.8 presents a sample GA run.

The improvement between the first random generation and the fitness plateau is about 50%. Normally the GA improvement is expressed relative to a benchmark, the most natural one being the performance of a TL pulse. But here the TL pulse is producing the best results (see the red line in Figure 4.8) and the first random generation cannot be used as a reference point. We have also run a few minimization GAs which showed a 25% reduction in the 13-cis yield compared to the initial generation. This result suggests

that a full 75% control range is achievable. However the fact that the highest intensity pulse maximizes the yield makes minimization experiments less insightful. It is expected that long pulses will automatically perform poorly. In order to understand these results the experiment has been expanded in a couple of directions. As it turns out, the simple the GA solution triggers very complex molecular dynamics.

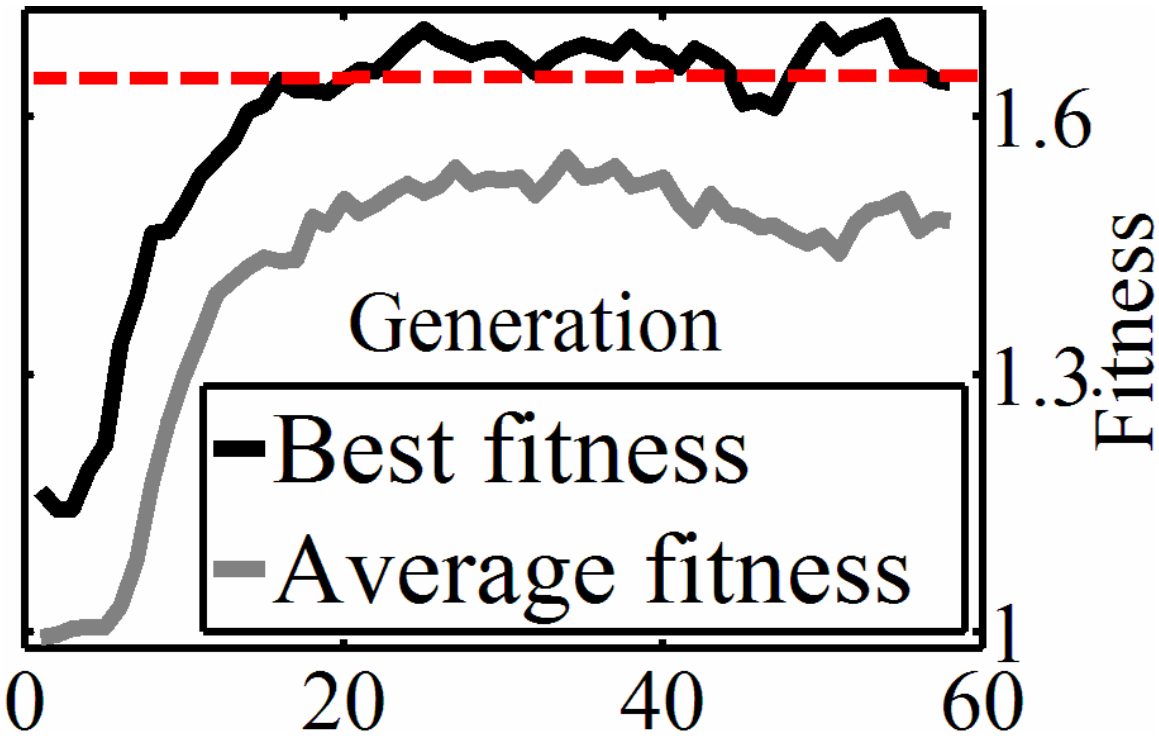

Figure 4.8. A GA run performed at 150 nJ pump energy with a "Nπ" basis set. The black curve represents the fitness of the best individual of each generation and the grey curve represents the mean fitness of each generation. Some short term and longer-term laser fluctuations can be observed but the GA converges consistently. The red line shows the fitness of a TL pulse.

At low intensity the GA is not successful. We have performed a number of searches, at a few low excitation energies and for all three bases mentioned above. While a threshold is not easy to define, it appears that the transition from non-controllability to phase control happens at ~ 50 nJ pulse energies. Our findings contrast with those reported by Miller et al. in [33]. It might be that amplitude shaping is the key feature allowing

control at low intensity. Miller et al. use actinic energy normalization, which takes into account the overlap between the pump spectrum and the all-trans absorption spectrum. This procedure might help the GA to find the complex phase-amplitude solutions reported in that work. Most likely future experiments will settle this issue.

4.4. Energy and Bandwidth Scans

Given that the highest intensity pulse produces the largest isomerization yield, it is natural to study the molecular response while varying the intensity knob. Intensity can be tuned, among other ways, by changing the energy or the bandwidth of the excitation pulse. We present first the bandwidth measurement. Our initial approach was to cut the pulse bandwidth, monitor the decrease in energy and correct the isomerization yield value post-experimentally. This method makes a few assumptions about the experimental conditions and was proven to give wrong results. The best approach is to tune the bandwidth and at the same time to vary the AOM amplitude in order to maintain the pulse energy constant.

Figure 4.9 shows the absorption signal at 650 nm and 40 ps pump-probe delay versus the pulse bandwidth. In addition to the amplitude adjustment mentioned above we have to take into account a second issue. Different pump spectra (see figure 4.10) have different overlap factors with the bR all-trans absorption spectrum and the signal level needs to be adjusted correspondingly. The dominant trend is that the larger the bandwidth the higher the isomerization yield. We have to remark that this scan cannot separate the pure bandwidth effect from the duration effect because the pulses employed here have different durations. A possible solution would be to compare a narrow bandwidth TL pulse with a chirped broad-band pulse of the same duration. However this approach has its own drawbacks. One outlier is the data point collected for the narrowest bandwidth, of only 6 nm FWHM. In this case the AOM significantly distorts the spatial profile of the pulse, due to over-shaping, such that the pump-probe overlap is affected. This means that we do have an experimental limit for how narrow the excitation pulses can be.

The energy scans have been performed for compressed pulses, by changing the AOM amplitude. We monitor all the relevant intermediates (all-trans, I_{460}, J_{625} and K_{590}).

In some cases, in order to better understand the impact of excitation intensity on the dynamics of a certain conformation, we took intensity scans at a couple of delays. The main results are summarized in Figure 4.11

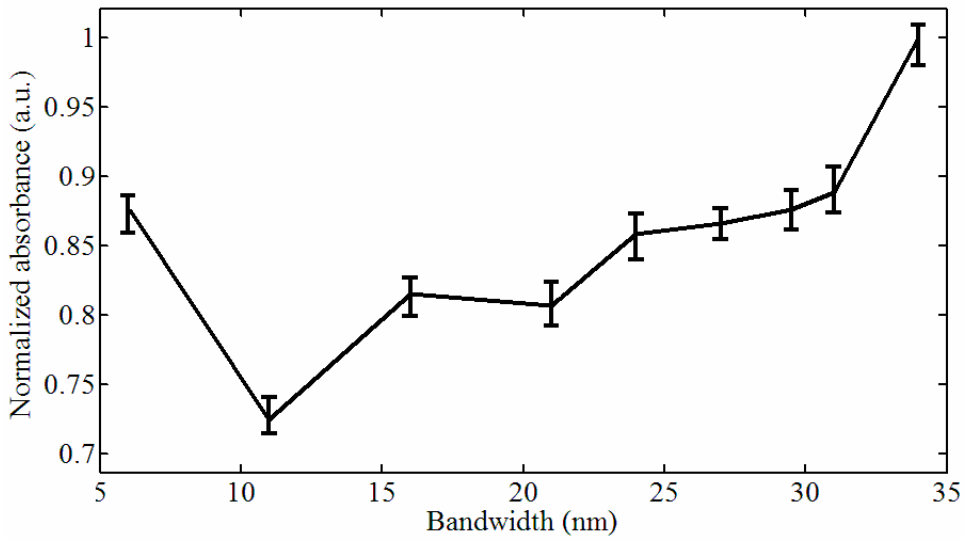

Figure 4.9. The isomerization yield versus the pump FWHM bandwidth. The error bars are 95% confidence intervals. They are proportional to the standard deviation of the mean for each data point. Each data point represents the average of ~ 1000 independent readings.

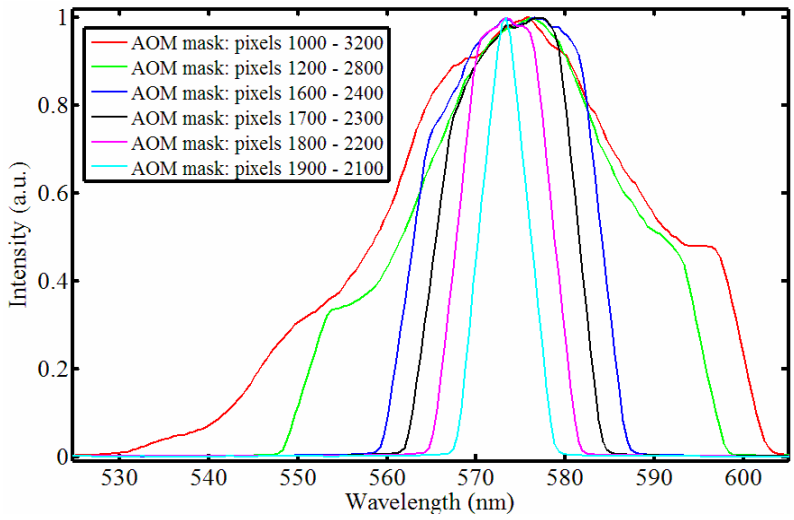

Figure 4.10. The pump spectra used in the bandwidth scan experiment. Always a TL phase shape is applied such that for all spectra the shortest possible pulse is used.

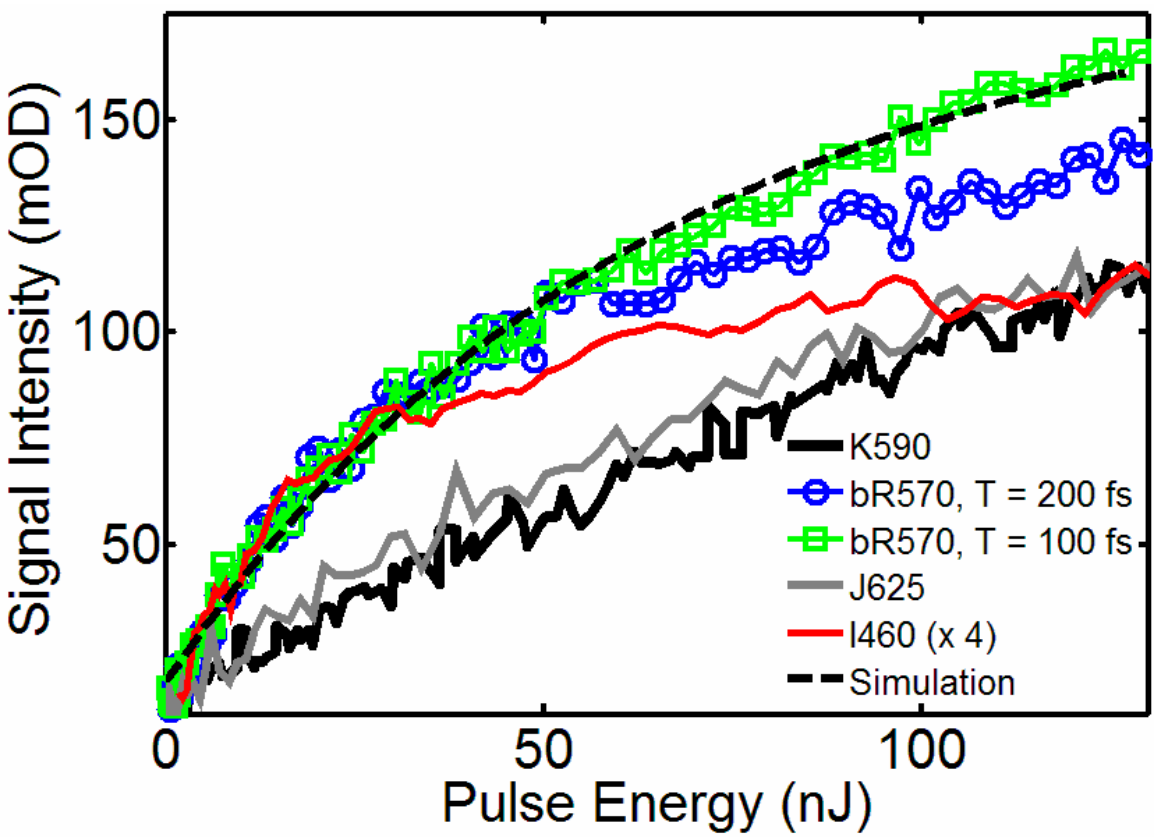

Figure 4.11. Intensity scans monitoring the signal strength of the isomerization intermediates: the all-trans bleach at 100 fs and 200 fs after excitation (squares and circles), the I_{460} stimulated emission at 850 nm (red), the J_{625} absorption at 650 nm ($T - T_0 \approx 2$ ps) and the K_{590} absorption signal at 650 nm ($T - T_0 \approx 40$ps).

As explained above, the ground state is in an all-trans conformation and the initial excitation places population vertically up in the first excited state, called H. The green squares and blue circles describe the ground state bleach at 100 fs and 200 fs delays. The bleach signal is proportional to the total amount of all-trans population excited up and available for the isomerization reaction. $T - T_0 = 100$ fs corresponds roughly to the time when the pump pulse is not temporally overlapped with the probe anymore. It exhibits a sub-linear (saturating) dependence on intensity. The blue curve represents the same signal, but at a delay of 200 fs. The curves split at pump energies above 60 nJ, which suggests that a fraction of the excited population returns to the ground state in the 100 fs time interval between the two measurements. An alternative explanation could be that the

excited states accessed by the photo-excitation process absorb light at 570 nm. In this scenario the recovery of the 570 nm absorption is not due to the return of the population to all-trans but to the increased population in excited intermediate states. Transient scans measurements (see Figure 4.13) have shown that in the 100 fs – 200 fs window we do have a bleach decay of 0 – 5% depending on the excitation conditions. The decay happens after the pump is gone so it must be due to stand-alone population dynamics. It is interesting that the bleach recovery exhibits the sharp 60 nJ threshold. This value coincides roughly with the point where the GA algorithm starts to be successful. The 200 fs delay also represents the time when the I_{460} signal at 487 nm reaches its peak. As explained above, the three-state model argues that it takes about 200 fs for the H population to reach the I_{460} conformation. This could mean that the initial (< 200 fs) bleach recovery is due to the H → all-trans transition. As mentioned above, spectral congestion does not allow a more categorical conclusion.

What is striking is the difference between the I_{460} (red) and the all-trans curves. If almost all of the H population goes to I_{460} then all three plots should follow the same trend. However the I_{460} signal saturates more strongly. The discrepancy suggests that the missing part is excited to another state (S_n), and never reaches the I_{460} conformation. Support for this view comes from a number of studies [39, 44, 105]. Gerber et al. [39] excite population to a higher excited state with 400 nm pump pulses and then follow the wave packet evolution after $S_n \rightarrow I_{460}$ relaxation. El-Sayed et al. [105] studied the all-trans → H → S_n → I_{460} excitation with a two-pump-single-dump scheme. These two studies assume that all of the population excited to S_n relaxes back to the I_{460} state. Our results suggest that a large fraction avoids the I_{460} conformation completely. However we do have data which shows that a part of the S_n population does relax to I_{460} (see Section 4.5).

Despite the sub-linear behavior of the "input" (all-trans) population, the "output" represented by the K_{590} signal (black continuous curve) is linear over a much larger range of pump intensities. This can happen only if, for a given total excited population, the branching ratio between the all-trans and 13-cis pathways is altered at high intensity. The next sections present a model explaining why this is the case.

In order to get a better understanding of the physical processes involved we performed a simple rate equation model, including the all-trans, H, and S_n conformers. The corresponding equations are shown below:

$$\frac{\partial N_{bR}}{\partial t} = -\sigma \times P \times N_{bR} + \sigma \times P \times N_H \tag{4.1}$$

$$\frac{\partial N_H}{\partial t} = -\sigma \times P \times N_H + \sigma \times P \times N_{bR} - f \times \sigma \times P \times N_H + f \times \sigma \times P \times N_{S_n} \tag{4.2}$$

$$\frac{\partial N_{S_n}}{\partial t} = -f \times \sigma \times P \times N_{S_n} + f \times \sigma \times P \times N_H \tag{4.3}$$

The model requires one photon coupling between the H and the S_n states. However simulations involving simultaneous one and two-photon transitions from H to "S_n" states produced similar results. The parameters used above are: σ = the absorption cross-section; P = the photon spectral density; f = a parameter scaling the H – S_n coupling relative to the strength of the bR (i.e. all-trans) ↔ H coupling. The extinction coefficient is 63, 000 mol/(liter x cm^{-1}), f is varied between 1 and 10^{-2} and time is varied between 1 and 50 fs, of the order of the pump duration. The dashed black curve in Figure 4.11 shows that this simple rate model explains the general features of the ground state bleach, but fails to account for the almost linear region of the scan, between 60 nJ and 100 nJ. Taking into account that the bleach is measured 100 fs after the peak of the coherent spike molecular dynamics or more complex excitation schemes could account for the discrepancy. The value of the model presented above is in pointing out the limitations of a simple picture.

Next we performed chirp scans, in which linear chirp is imparted onto the TL phase profile while monitoring the J_{625} and K_{590} states. Both low and high excitation energies are used. Figure 4.12 shows the linear chirp scans at high intensity (upper panel) and low intensity (lower panel). Consistent with the GA experiments, phase makes a difference only at high intensity. For low intensity no trend is observed within the limit given by the 5% RMS noise of the signal. The TL pulse is about 20 fs long while the longest pulses (± 1 × 10^5 fs^2 quadratic phase) are about 150 fs – 200 fs long. A small peak-shift towards negative chirp is noticeable. However FROG characterization of those

chirped pulses show that their duration is within 5% of that of the TL pulse, which is at the limit of our temporal resolution. An earlier study by Shank et al. [37] showed that chirp has a strong impact on the vibrational coherences in bR but chirped pulses longer than ~ 20 fs wash out the oscillations. We look here at population signals, not vibrations but we can speculate that our TL pulses are almost too long for observing fine chirp effects. Future experiments with much shorter pulses could verify the fact that slightly negative pulses enhance the isomerization yield. Another observation is that positive and negative pulses give different yields in the tails of the scan. Given the complexity of the reaction and the small effect (< 5%) it is hard to pinpoint the mechanism through which the chirp sign produces this difference. The small asymmetry of the excitation spectrum could also account for it.

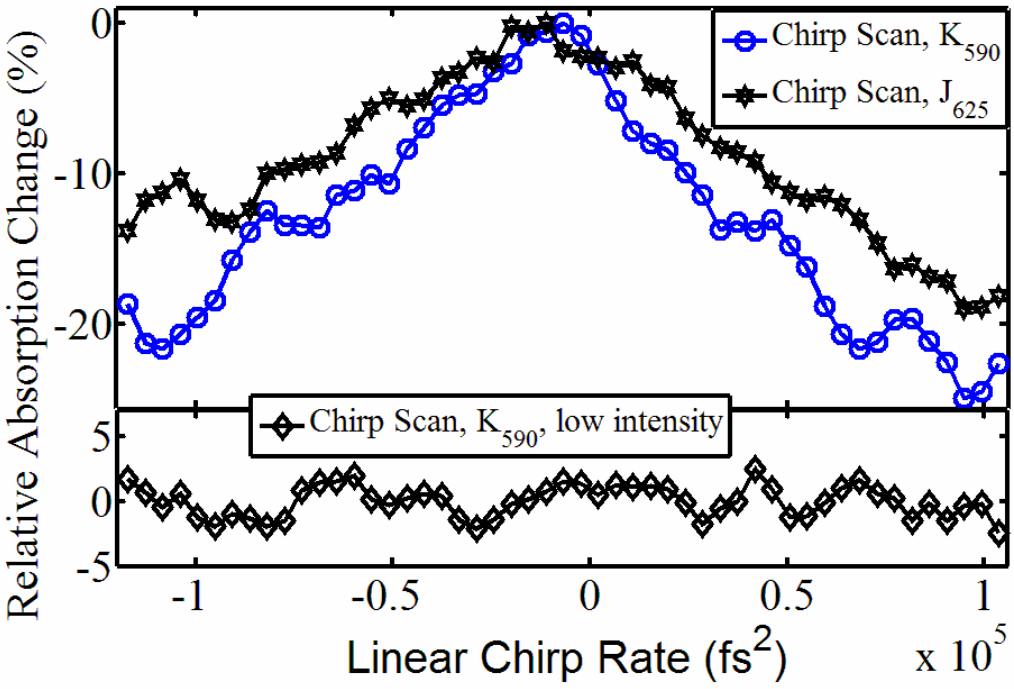

Figure 4.12. Upper panel: chirp scans monitoring the K_{590} (blue curve) and the J_{625} (black curve) conformations. The excitation energy is ~ 150 nJ. Lower panel: the same measurement for K_{590} performed at ~ 20 nJ excitation energy.

4.5. Transient Scans

The previous sections introduced the genetic search algorithm and the auxiliary scans and strengthened the conclusion that a high intensity pulse is optimal for maximization of the isomerization yield. The important question at this point is why this is the case. Transient scans are a very useful tool to unveil the molecular mechanisms. By varying the excitation pulse characteristics one can compare the molecular dynamics under optimal and sub-optimal excitation conditions. The differences will tell what features are needed for control. As above, all the isomerization intermediates are monitored. We start by presenting the dynamics of the all-trans ground state.

4.5.1 Transient Scans at 570 nm

In the transient scans presented in Figure 4.13 we can identify three components. The first component starts at T_0 (marked by the coherent spike in the black curve) and ends 200 fs later, at the point marked by the vertical arrow. In this time interval the bleach recovery depends strongly on the excitation pulse characteristics. For the high intensity excitation (black and red curves) the recovery is about 5 – 10%. For the low intensity pulse (blue curve) the recovery starts earlier than for the other cases. Figure 4.11 showed that above 60 nJ excitation energy the bleach signal at $T - T_0 = 200$ fs saturates. Presumably the bleach recovery in the first 200 fs is dominated by the H to all-trans transition. The above observations imply that pulse phase and energy can control the recovery rate. It is not clear whether the highest intensity pulse is the optimal pulse for maximizing the bleach recovery, as the intensity scans would suggest. A systematic search would be needed for clarifying this point. The difficulty is that when the feedback signal is time dependent pulse shaping can move the pump – probe timing, introducing false trends. This is the reason why chirp scans and GAs at early delays are inconvenient.

The arrow marks the onset of a sharp fall in the bleach signal (the second component) followed, after ~ 2ps, by a third, much slower component. The results of a bi-exponential fit are shown in Table 4.1. The fits have an R^2 of ~ 0.99 for the high fluence curves. For low intensity the onset of the decay happens earlier. The large error

bars for transient scans taken at low excitation intensity are due to poor signal-to-noise ratio. A model employing three or four exponentials gives poorer results.

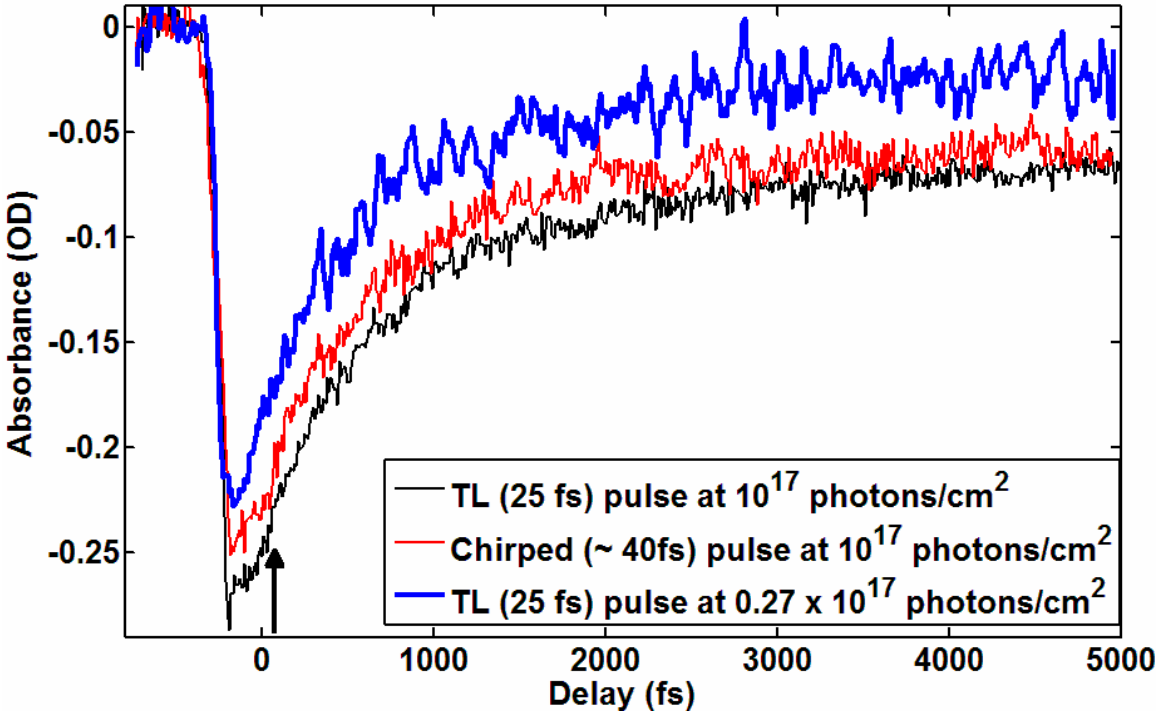

Figure 4.13. Transient scans for three excitation conditions. The chirp for the red curve is negative. The fluence of 10^{17} photons/cm^2 corresponds to ~ 120 nJ. The arrow is a visual aid marking the separation of the first and second time component.

We have performed transient scans up to 100 ps. By 30 ps the signal flattens out and no further changes are observed. The long scans confirm the time constants extracted from the shorter scans. The main trend is that both T_1 and T_2 are much shorter for low excitation intensity, regardless of the phase profile. To understand why this is the case we need to connect these measurements with those monitoring the excited states. The H state is spectroscopically invisible so the next monitored conformation is I_{460}.

Excitation conditions	T_1 (fs)	T_2 (ps)
TL, 120 nJ	582 ±17	5.4 ± 0.4
TL, 20 nJ	312 ± 203	1.1 ± 0.2
Neg. chirp (40 fs), 120 nJ	708 ± 35	9.2 ± 1.5
Neg. chirp (40 fs), 20 nJ	284 ± 121	1 ± 0.3
Pos. chirp (50 fs), 120 nJ	537 ± 102	2.5 ± 1.3
Pos. chirp (50 fs), 20 nJ	478 ± 325	1.37 ± 1.3

Table 4.1. Decay times of the all-trans bleach for various phase profiles and two pulse energies. T_1 and T_2 are the time constants of the bi-exponential fit for each transient scan.

4.5.2 Transient Scans at 487 nm and 850 nm

Two wavelengths are used for the purpose of tracking the I_{460} population: 487 nm, which monitors directly the absorption and 850 nm, which monitors the stimulated emission from this state. Figures 4.14 and 4.15 present some of these plots. Figure 4.14 shows three transient scans taken at 850 nm. The coherent spikes are a few hundred femtoseconds before the signal peak. This contrasts with the plots of Figure 4.15, where the absorption peak is overlapping with the coherent spikes. It has been argued that the I_{460} population needs to undergo some form of relaxation before the stimulated emission/fluorescence signal is apparent [9, 43, 106]. Another hypothesis is that some absorbing band present at early times (< 300 fs) counter-balances the fluorescence signal [43]. This effect is not seen by the absorption signal and this is why it emerges much faster, right after the coherent spike. The early time features in Figure 4.15 have a complex structure characterized by a strong peak, a dip and a second peak. The coherent spike explains some of these features. However some transient scans still exhibit peak - dip features even after the spike extraction.

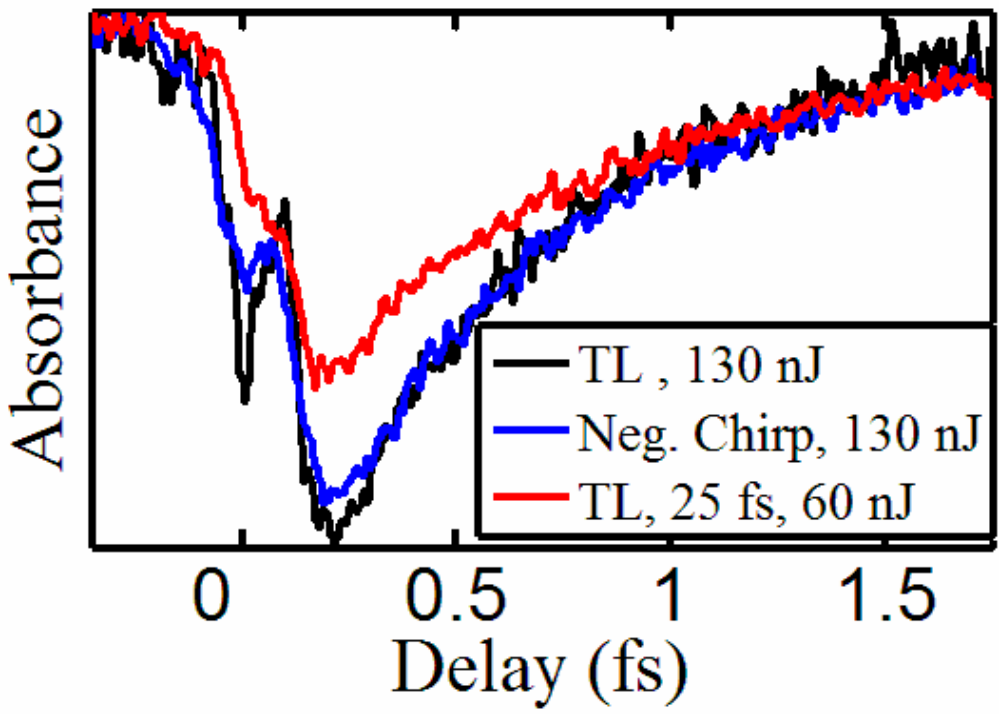

Figure 4.14. Transient scans taken at 850 nm. The negative chirped pulse is identical to the pulse from Figure 4.13.

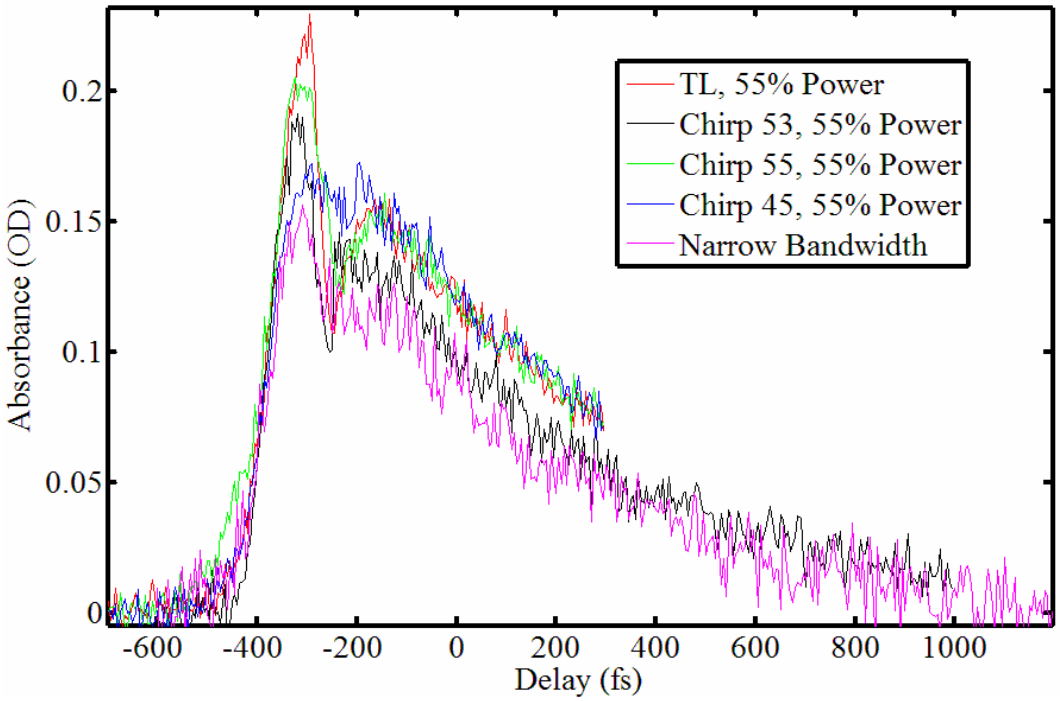

Figure 4.15. Transient scans measuring the dynamics of the I_{460} absorption, at 487 nm. Some scans have a shorter time span.

An example of successful extraction of the coherent spike is presented in Figure 4.16. The red line represents a pump-probe trace taken in the neat buffer (no bR), with the same flow cell in which the experiment is performed. After spike extraction the scan looks much smoother but a small dip can still be observed from – 200 fs to – 100 fs. Certainly the scan does not follow a mono-exponential fit as in the case of the 850 nm scans. For other excitation parameters the spike extraction is even less satisfactory. This mismatch could suggest that the population dynamics is more complex than a simple H $\rightarrow$ I_{460} transfer would imply. A possible explanation is that a part of the population excited to the S_n state returns to the I_{460} state in about 200 fs after excitation, resulting in a non-exponential decay of the absorption signal. El-Sayed et al. [105] have studied this path and found that indeed there is a higher excited state populating the I_{460} conformation. As before, other conformers could contribute to the signal measured at 487 nm (especially the all-trans state) complicating the analysis. The 850 nm scans do not see the $S_n \rightarrow I_{460}$ contribution because their signal is delayed a few hundreds of femtoseconds and the ultrafast $S_n \rightarrow I_{460}$ step ends earlier.

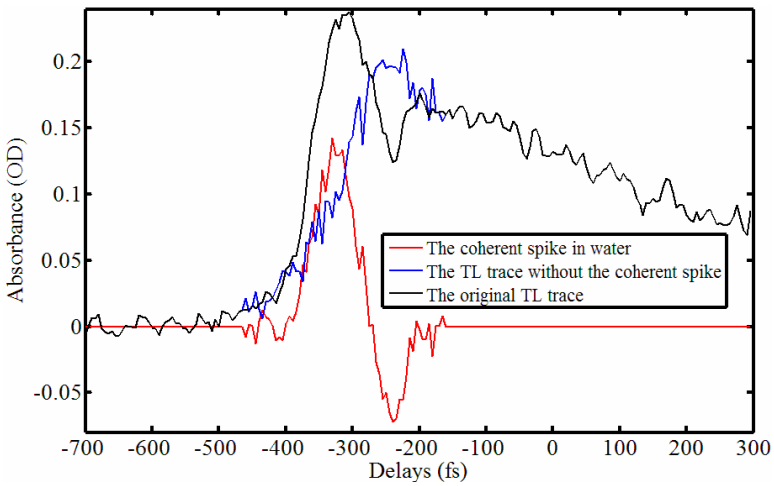

Figure 4.16. The black curve shows a transient scan taken at 487 nm, with a TL, high energy excitation pulse. The red curve shows the coherent spike measured in the bR solvent (phosphate buffer). The blue curve shows the transient signal after the coherent spike is extracted. Small time and amplitude adjustments were needed for finding the optimal way to extract the spike.

At this point in our analysis we need to quantify the extent of the bleach recovery for various excitation conditions. To do this we measure the relative change of the signal between $T - T_0 = 200$ fs and $T - T_0 = 2$ ps. We chose this time interval because it corresponds to the lifetime of the I_{460} state. Previous studies [101, 106] have shown that in this time interval the all-trans state is repopulated through non-radiative decay from the I_{460} state. Since this represents a direct loss for the 13-cis yield, we are very interested in quantifying it. Table 4.2 summarizes these calculations.

Excitation Pulse	T (fs), I_{460}	ΔA/A (%), all-trans	ΔA/A (%), I_{460}
TL, 10^{17} photons/cm^2	578 ± 14	61 ± 2.9	90 ± 1.4
TL, 0.6 x 10^{17} photons/cm^2	750 ± 58	66 ± 2.5	80 ± 1.7
NC, 10^{17} photons/cm^2	555 ± 25	64 ± 2	84 ± 2.3
PC1, 10^{17} photons/cm^2	727 ± 49	66 ± 3	84 ± 2.1
PC2, 10^{17} photons/cm^2	723 ± 52	63 ± 2.5	77 ± 2.5

Table 4.2. Column 2: decay times for the stimulated emission of the I_{460} conformation (single exponential fit). Columns 3 and 4: relative change of the signal for the all-trans bleach and I_{460} stimulated emission, in the interval $T = 200$ fs $\rightarrow$ $T = 2$ ps. The 10^{17} photons/cm^2 fluence corresponds to pulse energy of 120 nJ.

A pattern takes shape from the data shown in Table 2: the higher the intensity of the excitation pulse the stronger the decay of the I_{460} population but the weaker the recovery of the all-trans population. This means that the replenishing of the ground state by non-radiative transition from the I_{460} state becomes weaker at high intensity. Alternatively, this means that more of the I_{460} population branches towards the conical intersection and not towards the all-trans state. What is the reason for smaller "losses" to the all-trans state? The answer can be seen in Column 2 of Table 2. The higher the intensity the faster the decay of the I_{460} population is. We expect that if the population spends less time in the region where non-radiative decay is possible, its losses will be smaller. This is consistent with a model involving the contribution of higher excited

states. The population following the $S_n \rightarrow I_{460}$ route will be vibrationally hot when reaching the I_{460} conformer and will see a smaller barrier on its way towards the conical intersection. As a result it will walk away faster. This model is consistent with previously published studies [39, 108]. Alternatively, stimulated Raman scattering between H and S_n could create a vibrationally hot wave packet in H which then will slide down towards I_{460}, resulting in faster dynamics.

It should be mentioned that spectral congestion could alter the interpretation of the results presented above. The rise of other conformers absorbing at 570 nm would contribute to the apparent decay of the all-trans bleach. Alternatively at high intensity the population returning to all-trans could be "hot" and it will take a longer time to reach the region probed by the 570 nm probe wavelength, resulting in apparently smaller recovery.

4.5.3 Transient Scans at 650 nm

The next transient measurements deal with the $J_{625} \rightarrow K_{590}$ segment of isomerization. Figure 4.17 shows these results.

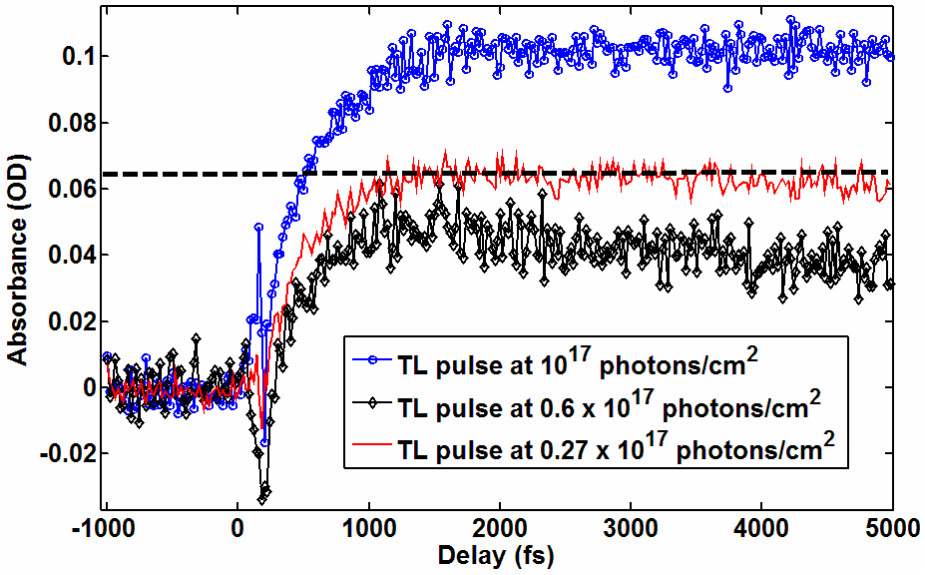

Figure 4.17. Transient scans at 650 nm, monitoring the J_{625} and K_{590} conformations. The traces are normalized by the strength of the I_{460} stimulated emission for the corresponding pump fluences. Despite this, the highest intensity scan still has much higher signal, showing that the I_{460} state does not account for the entire yield.

We can identify three segments in figure 4.17. The first one (T = 0 fs to T ≈ 300 fs) contains the coherent spike and a strong negative feature which has been assigned in literature to a very fast excited state absorption component [42]. The second segment (T = 300 fs to T = 2 ps) corresponds to the rise of the J_{625} signal. For the plots presented in Figure 4.17 the rise times are 400 ± 34 fs, 353 ± 13 fs and 290 ± 44 fs for the energies 40, 80 and 130 nJ, respectively After T = 2 ps the population should relax towards the all-trans or K_{590} conformations. Both of them have lower absorption coefficients at 650 nm compared to J_{625}, with K_{590} stronger than the all-trans signal [122]. This means that the 650 nm absorption is expected to decrease after the J → K or J → all-trans transitions. The smaller the decrease the larger the K_{590} yield will be. In figure 4.17 we see that the higher the intensity the slower the signal decays. This could mean either that the population spends more time in the J_{625} configuration or that the branching is stronger towards the more absorbent isomer, K_{590}. Long scans show that at high intensity the signal does go down, but at later times. This suggests that the first hypothesis is true: at high intensity the population spends more time in the J_{625} conformation.

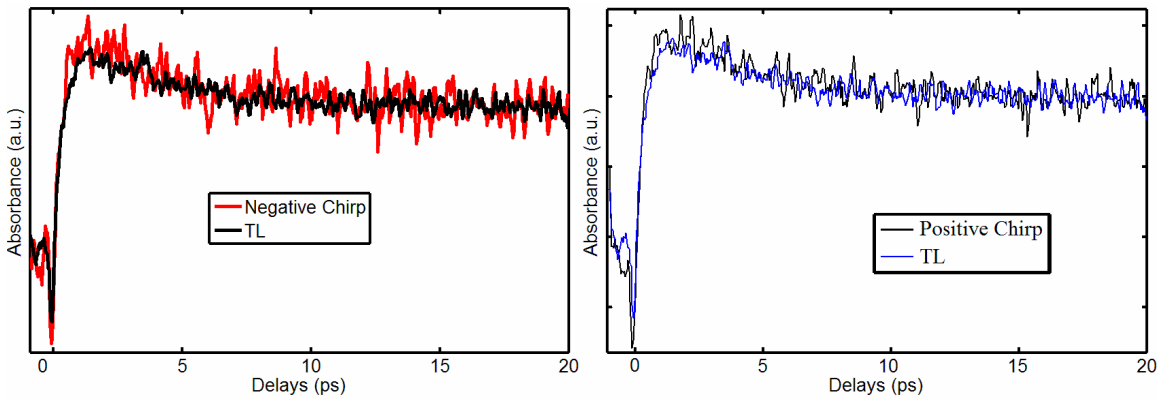

Figure 4.18. Transient scans for the TL, negative chirp and a positive chirp pulse, at intermediate excitation energy. The TL scan has been shifted down to match the tails of the other two plots.

Figure 4.18 shows a comparison between transient scans taken at intermediate pump fluences with a TL and chirped pulses. The tails have been matched to emphasize the faster decay of the signal for chirped pulse excitation. We see that for both positively

and negatively chirped pulses the trace starts higher but ends at the same level as the TL trace after about 10 ps. This means that both pulse energy and chirp have an impact on the dynamics of the J_{625} and K_{590} states. The signal-to-noise ratio is quite poor but the behavior observed in Figure 4.18 has been seen for other similar chirped pulse versus TL pulse measurements.

At this point the focus is to establish if J_{625} is an excited state conformer or is a vibrationally hot version of K_{590}. It has been shown that for high excitation intensity the I_{460} population moves faster towards the conical intersection (see Figure 4.14). The reason is that at high intensity the I_{460} population is vibrationally hot and can easily bypass the small barrier at the right (Figure 4.3). At the same time the difference between the all-trans and I_{460} energy scans (Figure 4.11) shows that some of the excited population never passes trough I_{460}. This population is expected to reach the conical intersection region through another pathway. The conical intersection region can be thought of as a "narrow slit". From the above arguments it results that at high excitation intensity it is likely that the population reaching the conical intersection is vibrationally hot and possibly dispersed along a number of normal coordinates. The transfer towards the ground electronic state will be slowed down in this situation, consistent with the slow decay of the J_{625} spectral signature. If the J_{625} conformation is in the ground state then for high energy it should rise slower, in contradiction with the data. Another factor supporting this model is the rise times for the J_{625} state. We have shown that the higher the intensity the faster the rise of the J_{625} state is. Following the same argument as above, if J is a ground state conformation the rise should be slower at high intensity.

We cannot exclude the possibility that other $S_1 \rightarrow S_0$ conical intersections are accessed by the excited state population. Their spectral signatures could be either beyond the extent of our probe spectrum or could contribute to the 650 nm probe signal, altering the above interpretation. Another possibility is that J_{625} is a vibrationally hot ground state conformer. This would be consistent with the fact that at high excitation intensity its decay is slower. But in this scenario it is not clear why its rise time would be faster. Future experiments could clarify this issue.

The slower transfer rate could help the branching of the population towards the K_{590} conformation. This statement is supported by the data in Figure 4.18. After ~ 20 ps

there are no more changes in the population dynamics. By comparing the peak and the tail of the transient scans we see that under chirped excitation the relative decrease of the signal is higher than for the TL excitation. This change describes how much of the J_{625} population actually reaches the K_{590} state. The connection between the speed of the transition at the conical intersection and the branching ratio could be explained by the following argument [42, 93]: when the conical intersection is approached from the all-trans direction a fast transition to the ground state would likely leave the population in the all-trans geometry. A slow transition would allow the nuclei to rearrange and adapt the 13-cis geometry. This tentative model needs to be experimentally checked. For example probing of the stimulated emission at wavelengths beyond 900 nm could possibly monitor the population dynamics for small $S_0 - S_1$ energy separations, i.e. closer to the conical intersection. The study of bR mutants with various distances between S_0 and S_1 could also bring more information about the role played by the conical intersection region [93].

4.6. Discussion and Conclusions

In summary the model emerging from the above experiments is presented in Figure 4.3. This model is supported by experimental and theoretical studies published in the last years. However some of its elements, like the position of the J_{625} conformer and the controllability of the branching ratio at the conical intersection need further confirmation. Starting from the all-trans ground state the wave packet is excited vertically to the H state. From here it can be excited further to the S_n state or can move towards the I_{460} configuration. Some of the S_n population relaxes to the I_{460} state but most of it avoids it and relaxes towards the conical intersection. S_n is used here to designate all higher excited states which could play a role in the isomerization process. Most likely a couple of "S_n" states are present and they could be coupled with one another by conical intersections. The I_{460} population has two pathways: one leads vertically down to the all-trans state, as shown by the stimulated emission measurements and the other towards the

$S_1 - S_0$ conical intersection. Our data suggests that the vertical transition accounts for a significant recovery of the ground state bleach. For a constant branching ratio from the conical intersection to the ground state, avoiding the I_{460} → all-trans transition contributes to the increase in the isomerization yield.

Our experimental data does not clarify if the I_{460} and S_n pathways lead to the same area of the conical intersection. Population drawn from both pathways contributes to the 650 nm signal making the individual contributions hard to separate. The J_{625} conformation appears to be part of the conical intersection, as discussed above.

The model detailed above explains why control of the isomerization yield is possible. We identify three "nodes" along the isomerization pathway where the phase profile and the energy of the excitation pulse could influence the branching ratio. The first is the H state from which the population can go in three directions: back to the all-trans ground state, to I_{460} or to S_n. At high intensity the S_n channel becomes significant. The I_{460} node is also controllable, that is for higher intensity the vertical losses to all-trans are minimized. Finally the J_{625} node appears to be controllable, because at high intensity more population branches towards the K_{590} conformation. All these three "nodes" could contribute to the final improved yield, and it's hard to disentangle completely their contributions. But the main conclusion is that higher intensity drives the isomerization reaction on a path favoring the 13-cis/K_{590} conformation.

Chapter V

Conclusions

The two experiments presented in this thesis deal with control of matter at a molecular level by means of femtosecond shaped laser pulses. Three actual aspects of coherent control are emphasized. The first is the use of shaped pulses as a tool to understand the intimate evolution of photo-chemical reactions. This aspect is most visible in the case of retinal isomerization in bR. The fact that transform-limit pulses are maximizing the isomerization yield pointed to the existence of other pathways not anticipated before the experiment. Further measurements used different pulse settings (different chirp and energy) to understand how the molecular dynamics depends on these control knobs. It is shown that the higher the intensity of the pulses the faster the dynamics of the I_{460} population and the slower the decay of the J_{625} population. These two conformers correspond to two important intermediate points along the isomerization pathway and their control shows that the initial excitation conditions can have significant impact picoseconds after the primary step.

The second feature is selective spectroscopy, emphasized in the experiment dealing with control of vibrational coherences in LD690. The simultaneous use of two control knobs (spectrum and chirp) enabled the almost exclusive stimulation of excited state wave packets. Retrieval of excited state characteristics like the frequency of oscillation and the dephasing time became straightforward. The small 570 cm^{-1} shoulder present in the Raman spectrum unambiguously proved to be the red-shifted frequency of the excited state mode. The dephasing time is usually extracted by fitting a sum of damped harmonic functions to the transient oscillatory signal. If the ground state

contribution is dominant retrieving the excited state time constant can be challenging. Shaped pulse excitation enables easy retrieval of the excited state dephasing time.

The third feature is complexity. LD690 is a fairly large sized molecule, but the dynamics monitored here relates to a single unambiguous feature: the oscillations of the ring breathing mode. The case of retinal isomerization in bR is radically different. Retinal is strongly coupled to the protein structure and has very complex dynamics, involving many transient conformations and a number of vibrational modes spanning the 150 cm^{-1} to 1800 cm^{-1} frequency range. Control of molecules of this scale met some success so far. An experiment performed by Motzkus et al. [30] showed that it's possible to minimize energy transfer in light harvesting complexes, but maximization attempts were not successful. Gerber et al. [39] reported a similar result for retinal isomerization in bacteriorhodopsin. The experiment reported here and the one performed by Miller et al. [33] show isomerization control in different excitation regimes, but the optimal pulse shapes are not similar and the discrepancies will require further investigation. Furthermore it is not clear that quantum coherence plays an important role, as claimed in [33]. In Chapter IV it is shown that the learning control experiment produces a 50% improvement in the isomerization yield between the TL pulse and long, low-intensity pulses. The emerging model does not require a coherent wave packet propagating along the full isomerization reaction path. Kobayashi et al. and Bardeen et al. [37, 40] showed that coherences can be maintained for about 1 ps. The full reaction proceeds in more than 5 ps. Future control experiments with ~ 5 fs pulses can follow directly the impact of coherent effects on the isomerization yield. So the question if quantum coherence plays a role in large scale chemistry remains open.

The experiments reported here open the door for more explorations. Vibrational bond excitation can potentially result in bond breaking and selective dissociation. While LD690 is a remarkably stable molecule, other molecules could prove good candidates for this type of experiment [121]. In another direction, the knowledge about the potential energy surfaces in LD690 naturally suggested chirp and spectral tuning as control knobs. However recent experiments suggest that linear chirp could be just one of the relevant phase knobs [122]. It would be instructive to perform a genetic algorithm experiment where the feedback is represented by the strength of the oscillatory signal. The main

difficulty is that for each candidate pulse shape a low-noise transient scan followed by FFT analysis has to be performed increasing significantly the running time. This would require the ability to perform rapid transient absorption scans with high signal-to-noise ratios.

The bacteriorhodopsin experiment presents even more exciting possibilities due to the inner complexity of the protein system. The use of much shorter pump pulses would enable the study of the participating high frequency vibrational modes. Expansion of the probe spectrum in the UV (~ 260 nm) and the near – IR (~ 950 nm) would enable better detection of the intermediate species. The impact of retinal – protein (tryptophan) coupling has been previously studied by means of UV absorption [109], but not in the context of shaped, short pulse excitation. Expansion of the probe spectrum in the near infrared region would allow better measurement of the I_{460} stimulated emission spectrum. Amplitude shaping could be used in conjunction with phase shaping to expand the range of possible excitation pulses. In the low intensity experiment amplitude shaping played a central role [32]. Its impact might have been two-fold. On one side sharp spectral features were present in the optimal excitation spectrum, with a periodicity related to the torsion frequency. On another hand the optimal and anti-optimal pulses had blue-tuned and red-tuned weight centers. This suggests that spectral tuning (in the way implemented in the LD690 experiment) could provide another control knob. Excitation with blue pulses (at 400 nm) could directly access S_n states and the ensuing dynamics could be compared to the measurements detailed in this work. A drastic reduction in the noise could make possible a successful experiment in low intensity, low-signal level conditions. Finally control studies of retinal in other environment could bring insights regarding the very important role played by the protein environment in assisting the isomerization reaction.

Bacteriorhodopsin is intensively studied for bio-photonic applications like holographic memories or optically-integrated circuits [41, 98, 123]. In this context increased isomerization efficiency is very important. The energy scans shown in Figure 4.11 can be seen as a optical linearization device: a non-linear input signal (the bleach of the ground all-trans state) results in a linear output signal (the 13-cis isomer absorption). Trough analogy with electrical devices (diodes for example) this feature could play an important role in future optical devices.

Bibliography

[1] Zewail, A. H. *J. Phys. Chem. A*, **104**, 5660 (2000).
[2] Cerullo, G. and Silvestri, S. D. *Rev. Scie. Instr.*, **74**, 18 (2003).
[3] Carley, R. E., Heesel, E. and Fielding, H. H. *Chem. Soc. Rev.*, **34**, 949 (2005).
[4] Brabec, T. and Krausz, F. *Rev. Mod. Phys.*, **72**, 545 (2000).
[5] Kobayashi, T. and Baltuska, A. *Meas. Sci. Technol.*, **13**, 1671 (2002).
[6] Bucksbaum, P. H. *Science*, **317**, 766 (2007).
[7] Vos, M. H. and Martin, J. L. *Biochim. Biophys. Acta-Bioenerg.*, **1411**, (1999).
[8] Dantus, M. and Lozovoy, V. V. *Chem. Rev.*, **104**, 1813 (2004).
[9] Nuernberger, P., Vogt, G., Brixner, T. and Gerber, G. *Phys. Chem. Chem. Phys.*, **9**, (2007).
[10] Judson, R. S. and Rabitz, H. *Phys. Rev. Lett.*, **68**, (1992).
[11] Kohler, B., Yakovlev, V. V., Che, J. W., Krause, J. L., Messina, M., Wilson, K. R., Schwentner, N., Whitnell, R. M. and Yan, Y. J. *Phys. Rev. Lett.*, **74**, (1995).
[12] Weinacht, T. C., Ahn, J. and Bucksbaum, P. H. *Nature*, **397**, (1999).
[13] Rice, S. R. and Zhao, M. *Optical Control of Molecular Dynamics*, Wiley-Interscience, New York (2000).
[14] Rabitz, H., de Vivie-Riedle, R., Motzkus, M. and Kompa, K. *Science*, **288**, 824 (2000).
[15] Brixner, T. and Gerber, G. *ChemPhysChem*, **4**, 418 (2003).
[16] Brumer, P. W. and Shapiro, M. *Principles of the Quantum Control of Molecular Processes.*, Wiley - Interscience, Hoboken, NJ (2003).
[17] Shapiro, M., and Brumer, P. *Rep. Prog. Phys.*, **66**, 859 (2003).
[18] Wohlleben, W., Buckup, T., Herek, J. L. and Motzkus, M. *ChemPhysChem*, **6**, 850 (2005).
[19] Abe, M., Ohtsuki, Y., Fujimura, Y. and Domcke, W. *J. Chem. Phys.*, **123**, (2005).
[20] Assion, A., Baumert, T., Bergt, M., Brixner, T., Kiefer, B., Seyfried, V., Strehle, M. and Gerber, G. *Science*, **282**, 919 (1998).
[21] Baltuska, A. and Kobayashi, T. *Appl. Phys. B*, **75**, 427 (2002).
[22] BARDEEN, C. J., WANG, Q. and Shank, C. V. *Phys. Rev. Lett.*, **75**, 3410 (1995).
[23] Bardeen, C. J., Yakovlev, V. V., Squier, J. A. and Wilson, K. R. *J. Am. Chem. Soc.*, **120**, 13023 (1998).
[24] Bardeen, C. J., Yakovlev, V. V., Wilson, K. R., Carpenter, S. D., Weber, P. M. and Warren, W. S. *Chem. Phys. Lett.*, **280**, 151 (1997).
[25] Brixner, T., Damrauer, N. H., Niklaus, P. and Gerber, G. *Nature*, **414**, (2001).
[26] Cao, J. S. and Wilson, K. R. *J. Chem. Phys.*, **107**, (1997).
[27] Fibich, G., Eisenmann, S., Ilan, B. and Zigler, A. *Opt. Lett.*, **29**, 1772 (2004).
[28] Florean, A. C., Carroll, E. C., Spears, K. G., Sension, R. J. and Bucksbaum, P. H. *J. Phys. Chem. B*, **110**, 20023 (2006).
[29] Geppert, D., Hofmann, A. and de Vivie-Riedle, R. *J. Chem. Phys.*, **119**, (2003).
[30] Herek, J. L., Wohlleben, W., Cogdell, R. J., Zeidler, D. and Motzkus, M. *Nature*, **417**, 533 (2002).

[31] Lee, S. H., Jung, K. H., Sung, J. H., Hong, K. H. and Nam, C. H. *J. Chem. Phys.*, **117**, 9858 (2002).
[32] Prokhorenko, V. I., Nagy, A. M. and Miller, R. J. D. *J. Chem. Phys.*, **122**, 184502-1 (2005).
[33] Prokhorenko, V. I., Nagy, A. M., Waschuk, S. A., Brown, L. S., Birge, R. R. and Miller, R. J. D. *Science*, **313**, 1257 (2006).
[34] Gaubatz, U., Rudecki, P., Schiemann, S. and Bergmann, K. *J. Chem. Phys.*, **92**, (1990).
[35] Pearson, B. J., White, J. L., Weinacht, T. C. and Bucksbaum, P. H. *Phys. Rev. A*, **63**, 063412-1 (2001).
[36] White, J. L., Pearson, B. J. and Bucksbaum, P. H. *J. Phys. B*, **37**, L399 (2004).
[37] Bardeen, C. J., Wang, Q. and Shank, C. V. *J. Phys. Chem. A*, **102**, 2759 (1998).
[38] Ogilvie, J. P., Débarre, D., Solinas, X., Martin, J.-L., Beaurepaire, E. and Joffre, M. (2006).
[39] Vogt, G., Nuernberger, P., Brixner, T. and Gerber, G. *Chem. Phys. Lett.*, **433**, (2006).
[40] Kobayashi, T., Saito, T. and Ohtani, H. *Nature*, **414**, (2001).
[41] Haupts, U., Tittor, J. and Oesterhelt, D. *Annu. Rev. Biophys. Biomolec. Struct.*, **28**, (1999).
[42] Abramczyk, H. *J. Chem. Phys.*, **120**, (2004).
[43] Haran, G., Wynne, K., Xie, A. H., He, Q., Chance, M. and Hochstrasser, R. M. *Chem. Phys. Lett.*, **261**, (1996).
[44] Backus, S., Peatross, J., Huang, C. P., Murnane, M. M. and Kapteyn, H. C. *Opt. Lett.*, **20**, 2000 (1995).
[45] Salin, F., Squier, J., Mourou, G. and Vaillancourt, G. *Opt. Lett.*, **16**, 1964 (1991).
[46] Riedle, E., Beutter, M., Lochbrunner, S., Piel, J., Schenkl, S., Spörlein, S. and Zinth, W. *Appl. Phys. B*, **71**, 457 (2000).
[47] Trapani, P. D., Andreoni, A., Banfi, G. P., Solcia, C., Danielius, R., Piskarskas, A., Foggi, P., Monguzzi, M. and C.Sozzi *Phys. Rev. A*, **51**, 3164 (1995).
[48] Boyd, R. W. *Nonlinear Optics*, Academic Press, San Diego, CA (2002).
[49] Alfano, R. R. and Shapiro, S. L. *Phys. Rev. Lett.*, **24**, 584 (1970).
[50] Zheltikov, A. M. *Phys.-Usp.*, **49**, 605 (2006).
[51] Brodeur, A. and Chin, S. L. *J. Opt. Soc. Am. B*, **16**, 637 (1999).
[52] Kovalenko, S. A., Dobryakov, A. L., Ruthmann, J. and Ernsting, N. P. *Phys. Rev. A*, **59**, 2369 (1999).
[53] Knox, W. H., Pearson, N. M., Li, K. D. and Hirlimann, C. A. *Opt. Lett.*, **13**, 574 (1988).
[54] Bor, Z. *Opt. Lett.*, **14**, 119 (1989).
[55] Ciddor, P. E. *Appl. Opt.*, **35**, 1566 (1996).
[56] Armstrong, J. A., Bloembergen, N., Ducuing, J. and Pershan, P. S. *Phys. Rev.*, **127**, 1918 (1962).
[57] Wang, H. and Weiner, A. M. *IEEE J. Quant. Electron.*, **39**, 1600 (2003).
[58] Florean, A. C., Carroll, E., Pearson, B., Sension, R. and Bucksbaum, P. H., DAMOP, 2005.
[59] Xu, L., Nakagawa, N., Morita, R., Shigekawa, H. and Yamashita, M. *IEEE J. Quant. Electron.*, **36**, 893 (2000).

[60] Xu, L., Li, L., Nakagawa, N., Morita, R. and Yamashita, M. *IEEE Photon. Techn. Lett.*, **12**, 1540 (2000).
[61] Weiner, A. M. *Rev. Scie. Instr.*, **71**, 1929 (2000).
[62] Brixner, T., Krampert, G., Pfeifer, T., Selle, R., Gerber, G., Wollenhaupt, M., Graefe, O., Horn, C., Liese, D., Baumert, T. *Phys. Rev. Lett.*, **92**, 208301-1 (2004).
[63] Brixner, T. and Gerber, G. *Opt. Lett.*, **26**, 557 (2001).
[64] Fork, R. L., Martinez, E. and Gordon, J. P. *Opt. Lett.*, **9**, 150 (1984).
[65] Sherriff, R. E. *J. Opt. Soc. Am. B*, **15**, 1224 (1998).
[66] Trebino, R., Long, K. W. D., Fittinghoff, D. N., Sweetser, J. N., Krumbugel, M. A., Richman, B. A. and Kane, D. J. *Rev. Scie. Instr.*, **68**, 3277 (1997).
[67] Hornung, T., Motzkus, M. and de Vivie-Riedle, R. *Phys. Rev. A*, **65**, (2002).
[68] Misawa, K. and Kobayashi, T. *J. Chem. Phys.*, **113**, 7546 (2000).
[69] Carroll, E. C., Pearson, B. J., Florean, A. C., Bucksbaum, P. H. and Sension, R. J. *J. Chem. Phys.*, **124**, 114506-1 (2006).
[70] Fainberg, B. D. and Gorbunov, V. A. *J. Chem. Phys.*, **117**, 7222 (2002).
[71] Yabushita, A., Fuji, T. and Kobayashi, T. *Chem. Phys. Lett.*, **398**, 495 (2004).
[72] Etchepare, J., Grillon, G. and Arabat, J. *Appl. Phys. B*, **49**, 425 (1989).
[73] Etchepare, J., Grillon, G., Hamoniaux, G., Antonetti, A. and Orszag, A. *Rev. Phys. Appl.*, **22**, 1749 (1987).
[74] Cerullo, G., Bardeen, C. J., Wang, Q. and Shank, C. V. *Chem. Phys. Lett.*, **262**, 362 (1996).
[75] Bardeen, C. J. and Shank, C. V. *Chem. Phys. Lett.*, **203**, 535 (1993).
[76] Bardeen, C. J., Rosenthal, S. J. and Shank, C. V. *J. Phys. Chem. A*, **103**, 10506 (1999).
[77] Nahmias, O., Bismuth, O., Shoshana, O. and Ruhman, S. *J. Phys. Chem. A*, **109**, 8246 (2005).
[78] Malkmus, S., Durr, R., Sobotta, C., Pulvermacher, H., Zinth, W. and Braun, M. *J. Phys. Chem. A*, **109**, (2005).
[79] Van Dao, L., Lincoln, C., Lowe, M. and Hannaford, P. *J. Chem. Phys.*, **120**, (2004).
[80] Yoon, M. C., Jeong, D. H., Cho, S., Kim, D., Rhee, H. and Joo, T. *J. Chem. Phys.*, **118**, (2003).
[81] Banin, U., Bartana, A., Ruhman, S. and Kosloff, R. *J. Chem. Phys.*, **101**, (1994).
[82] Saito, T. and Kobayashi, T. *J. Phys. Chem. A*, **106**, (2002).
[83] Kumar, A. T. N., Rosca, F., Widom, A. and Champion, P. M. *J. Chem. Phys.*, **114**, (2001).
[84] Lanzani, G., Zavelani-Rossi, M., Cerullo, G., Comoretto, D. and Dellepiane, G. *Phys. Rev. B*, **69**, (2004).
[85] Hornung, T., Skenderovic, H. and Motzkus, M. *Chem. Phys. Lett.*, **402**, (2005).
[86] Chesnoy, J. and Mokhtari, A. *Phys. Rev. A*, **38**, (1988).
[87] Cerullo, G., Luer, L., Manzoni, C., De Silvestri, S., Shoshana, O. and Ruhman, S. *J. Phys. Chem. A*, **107**, (2003).
[88] Carson, E. A., Diffey, W. M., Shelly, K. R., Lampa-Pastirk, S., Dillman, K. L., Schleicher, J. M. and Beck, W. F. *J. Phys. Chem. A*, **108**, (2004).
[89] Joo, T. H. and Albrecht, A. C. *Chem. Phys.*, **173**, (1993).
[90] Pollard, W. T., Dexheimer, S. L., Wang, Q., Peteanu, L. A., Shank, C. V. and Mathies, R. A. *J. Phys. Chem.*, **96**, (1992).

[91] Hong, Q., Pexton, I. A. D., Porter, G. and Klug, D. R. *J. Phys. Chem.*, **97**, (1993).
[92] Pollard, W. T., Lee, S. Y. and Mathies, R. A. *J. Chem. Phys.*, **92**, (1990).
[93] Gai, F., Hasson, K. C., McDonald, J. C. and Anfinrud, P. A. *Science*, **279**, (1998).
[94] Kuhlbrandt, W. *Nature*, **406**, (2000).
[95] Lanyi, J. K. *Biochim. Biophys. Acta-Bioenerg.*, **1757**, (2006).
[96] Lanyi, J. K. *J. Mol. Microbiol. Biotechnol.*, **12**, (2007).
[97] Schenkl, S., van Mourik, F., van der Zwan, G., Haacke, S. and Chergui, M. *Science*, **309**, (2005).
[98] Xu, J., Stickrath, A. B., Bhattacharya, P., Nees, J., Varo, G., Hillebrecht, J. R., Ren, L. and Birge, R. R. *Biophys. J.*, **85**, (2003).
[99] Atkinson, G. H., Ujj, L. and Zhou, Y. D. *J. Phys. Chem. A*, **104**, (2000).
[100] Balashov, S. P., Imasheva, E. S., Govindjee, R. and Ebrey, T. G. *Photochem. Photobiol.*, **54**, (1991).
[101] Dexheimer, S. L., Wang, Q., Peteanu, L. A., Pollard, W. T., Mathies, R. A. and Shank, C. V. *Chem. Phys. Lett.*, **188**, (1992).
[102] Herbst, J., Heyne, K. and Diller, R. *Science*, **297**, (2002).
[103] Hou, B. X., Friedman, N., Ottolenghi, M., Sheves, M. and Ruhman, S. *Chem. Phys. Lett.*, **381**, (2003).
[104] Kennis, J. T. M., Larsen, D. S., Ohta, K., Facciotti, M. T., Glaeser, R. M. and Fleming, G. R. *J. Phys. Chem. B*, **106**, (2002).
[105] Logunov, S. L., Volkov, V. V., Braun, M. and El-Sayed, M. A. *Proc. Natl. Acad. Sci. U. S. A.*, **98**, (2001).
[106] Mathies, R. A., Cruz, C. H. B., Pollard, W. T. and Shank, C. V. *Science*, **240**, (1988).
[107] Myers, A. B., Harris, R. A. and Mathies, R. A. *J. Chem. Phys.*, **79**, (1983).
[108] Ruhman, S., Hou, B. X., Friedman, N., Ottolenghi, M. and Sheves, M. *J. Am. Chem. Soc.*, **124**, (2002).
[109] Schenkl, S., van Mourik, F., Friedman, N., Sheves, M., Schlesinger, R., Haacke, S. and Chergui, M. *Proc. Natl. Acad. Sci. U. S. A.*, **103**, (2006).
[110] Terentis, A. C., Ujj, L., Abramczyk, H. and Atkinson, G. H. *Chem. Phys.*, **313**, (2005).
[111] Terpugov, E. L. and Degtyareva, O. V. *J. Mol. Struct.*, **565**, (2001).
[112] Wang, J. P. and El-Sayed, M. A. *Biophys. J.*, **83**, (2002).
[113] Ye, T., Gershgoren, E., Friedman, N., Ottolenghi, M., Sheves, M. and Ruhman, S. *Chem. Phys. Lett.*, **314**, (1999).
[114] Hoki, K. and Brumer, P. *Phys. Rev. Lett.*, **95**, (2005).
[115] Herek, J. L., Wohlleben, W., Cogdell, R. J., Zeidler, D. and Motzkus, M. *Nature*, **417**, 533 (2002).
[116] Bardeen, C. J., Yakovlev, V. V., Squier, J. A. and Wilson, K. R. *J. Am. Chem. Soc.*, **120**, 13023 (1998).
[117] Flores, S. C. and Batista, V. S. *J. Phys. Chem. B*, **108**, (2004).
[118] Ohtsuki, Y., Ohara, K., Abe, M., Nakagami, K. and Fujimura, Y. *Chem. Phys. Lett.*, **369**, (2003).
[119] Werner, O., Fischer, B. and Lewis, A. *Opt. Lett.*, **17**, (1992).
[120] Polland, H. J., Franz, M. A., Zinth, W., Kaiser, W., Kolling, E. and Oesterhelt, D. *Biophys. J.*, **49**, (1986).

[121] Carroll, E. C., Pearson, B. J., Florean, A. C., Bucksbaum, P. H. and Sension, R. J. *J. Chem. Phys.*, **124**, (2006).
[122] Nahmias, O., Bismuth, O., Shoshana, O. and Ruhman, S. *J. Phys. Chem. A*, **109**, (2005).
[123] Huang, Y. H., Fu, J., Hagan, D. J., Wu, S. T., Huang, X. H. and El-Sayed, M. A. *IEEE J. Sel. Top. Quantum Electron.*, **11**, (2005).